Luís António Rodrigues de Figueiredo Ferreira Pereira

AN EMULATION WORKBENCH FOR POSITION SENSITIVE GASEOUS SCINTILLATION DETECTORS

Tese de doutoramento em Engenharia Física – Ramo Instrumentação, orientada pelo Professor Doutor Francisco Fraga e apresentada ao Departamento de Física, da Faculdade de Ciências e Tecnologia da Universidade de Coimbra

Agosto de 2017

· U C ·

UNIVERSIDADE DE COIMBRA

DOCTORAL THESIS

An emulation workbench for position sensitive gaseous scintillation detectors

Author:
Luís PEREIRA

Supervisor:
Francisco FRAGA

Abstract

Position-sensitive gaseous scintillation detectors (PSGSD) with Anger-ty pe optical readout are being developed for use in various research areas such as neutron detection [1], search for dark matter [2] and neutrinoless double beta decay [3]. Using suitable gas mixtures, the avalanches produced in these detectors can emit up to 10^6 photons/MeV in tens of nanoseconds, allowing to achieve high spatial resolution ($\sim$1 mm) and high count rate (>1 MHz) over large detection areas (up to thousands of cm^2).

Design and optimization of PSGSDs frequently require taking into consideration a large number of interconnected factors being, for that reason, typically performed either iteratively or by means of numerical simulations. The first approach can be very demanding in terms of time and resources while numerical simulations do not often provide adequate results due to limitations of the physical model or lack of information on relevant properties of the elements of the detector.

The work presented in this thesis comprises the design, construction, calibration and validation tests of an emulation workbench for design and optimization of PSGSDs which allow to avoid constraints of both approaches. The emulation workbench has modular structure and both light emission properties and geometry of the detector can be independently configured allowing fast iterative optimization processes. Moreover, unlike numerical simulations, this approach does not depend on a model or on the detailed knowledge of the properties of the detector components. With this tool, point-like primary and secondary scintillation can be emulated with precise control of position, intensity and timing characteristics over a wide range of light intensities. The system is easily configurable, allowing quick modifications of the geometry and changes of the materials of elements of the emulated detector, as well as type, number and arrangement of the photodetectors. The two fundamental components of the workbench being presented are a quasi point-like isotropic light source installed on a 3D high resolution positioning system and an Anger-type optical readout consisting of an hexagonal arrangement of seven photomultipliers (PMTs). The light source emitting volume has approximately 1 mm in diameter and isotropy better than 10 % over $> 3.5\pi$. Light emission can be configured from $\sim 10^3$ to $\sim 10^6$ photons per pulse, with variable pulse duration between $\sim$1 ns and $\sim$1 s. The light source and the PMTs were installed in a light-tight box with black inner walls to suppress light scattering. Different elements such as surfaces or

glass windows can be quickly mounted (and unmounted) on holders placed inside the box for that purpose.

The operation of the emulation workbench was successfully validated using a minimal configuration consisting of the light source, the positioning system and the optical readout. Since reflections from the elements of the workbench were practically nonexistent, the signals from the photomultipliers (PMTs) depended, to a very good approximation, only on the position of the source, the amount of emitted photons, the optical readout geometry and the relative gains of the PMTs. Under these conditions numerical simulations are able to provide reliable predictions of the signals collected by the PMTs, if both PMTs and light source are calibrated. These calibrations were performed and measurements and simulations were conducted for matching conditions, providing information on the spatial resolution and the reconstruction bias as function of the source position and the number of emitted photons. A very good agreement was observed between the experimental and the simulated results.

The system was used to investigate several configurations relevant to the project dedicated to development of a position sensitive thermal neutrons detector based on a scintillation proportional counter with Anger-type optical readout [1], in which our group has been participating. In particular, the maximum likelihood algorithm was used to reconstruct events in case studies covering detector geometries with highly suppressed scattered light, with cylindrical walls built from materials with different light scattering properties and with a glass window interfacing the light source and the array of PMTs. Methods of data processing were developed to parameterize light response of the PMTs from the emulated data. The results demonstrate that the emulation workbench can be effectively applied to design and optimize PSGSDs, targeting the highest possible position and energy resolution as well as minimal spatial distortion of the reconstructed events.

The workbench can also be used to provide emulated realistic experimental signals to test PSGSD readout electronics, to study the performance of event reconstruction algorithms or to develop adaptive techniques of the detector response such as those presented in reference [4]. The same concept can be further developed for applications requiring adjustable wavelength and precisely-controlled time emission properties of the light source. It is envisage that this approach may eventually be extended to emulate light emission in liquid and solid scintillators by operating the light source in a volume filled with a liquid with optical properties (e.g. refractive index) matching

those of the scintillator in study.

Resumo

Detectores gasosos de cintilação sensíveis à posição (PSGSD) com leitura óptica tipo Anger, estão em desenvolvimento para serem usados em diversas áreas de investigação tais como a detecção de neutrões [1], a procura de matéria escura [2] e duplo decaimento beta sem neutrinos [3]. Usando misturas gasosas adequadas, as avalanches produzidas nestes detectores podem emitir até 10^6 fotões/MeV em dezenas de nano-segundos, permitindo alcançar elevada resolução espacial ($\sim$1 mm) e altas taxas de contagem (>1 MHz) ao longo de extensas áreas de detecção (até milhares de cm^2).

O desenho e a optimização de PSGSDs requerem frequentemente a consideração de um elevado número de factores interligados, sendo por essa razão tipicamente efectuados de forma iterativa ou com recurso a simulações numéricas. A primeira abordagem pode ser bastante exigente em termos de tempo e recursos enquanto as simulações numéricas muitas vezes não fornecem resultados adequados devido a limitações do modelo ou à falta de informação sobre propriedades relevantes de elementos do detector.

O trabalho apresentado nesta tese compreende o desenho, a construção, a calibração e os testes de validação de uma bancada de emulação para o desenho e optimização de PSGSDs a qual permite evitar constrangimentos das duas abordagens. A bancada de emulação tem uma estrutura modular e tanto as propriedades da emissão de luz como a geometria do detector podem ser configuradas de forma independente, permitindo processos iterativos de optimização rápidos. Mais ainda, contrariamente às simulações numéricas, esta abordagem não depende de um modelo ou do conhecimento detalhado das propriedades dos componentes do detector. Com esta ferramenta, cintilação quase-pontual primária e secundária podem ser emuladas com controlo preciso da posição, intensidade e características temporais numa vasta gama de intensidades de luz. O sistema é facilmente configurável, permitindo modificações rápidas da geometria e mudanças dos materiais de elementos do detector emulado, bem como o tipo, número e arranjo dos fotodetectores. Os dois componentes fundamentais da bancada apresentada são uma fonte de luz quase-pontual instalada num sistema de posicionamento de alta resolução e um sistema de leitura óptica tipo Anger que consiste num arranjo hexagonal de sete fotomultiplicadores (PMTs). A fonte de luz tem aproximadamente 1 mm de diâmetro e isotropia melhor que 10 % em $> 3.5\pi$. A emissão pode ser configurada para emitir entre $\sim 10^3$ e $\sim 10^6$ fotões por pulso, com duração variável entre $\sim$1 ns e $\sim$1 s. A fonte de luz e os PMTs estão instalados numa caixa hermética à luz com paredes interiores

pretas, para suprimir a reflexão de luz. Diferentes elementos, tais como superfícies ou janelas de vidro podem ser rapidamente montados (ou desmontados) em suportes colocados no interior da caixa para esse propósito.

A operação da bancada de emulação foi validada com sucesso com uma configuração minimalista, consistindo apenas na fonte de luz, no sistema de posicionamento e no sistema de leitura óptica. As reflexões a partir dos elementos da bancada foram suprimidas e os sinais dos PMTs dependiam, numa boa aproximação, apenas da posição da fonte, da quantidade de fotões emitidos, da geometria da câmara Anger e dos ganhos relativos dos PMTs. Nestas condições, as simulações numéricas são capazes de fornecer previsões fidedignas dos sinais dos PMTs, se os PMTs e a fonte de luz estiverem calibrados. Estas calibrações foram efectuadas e, tanto as medidas como as simulações, foram posteriormente conduzidas para as mesmas condições, fornecendo informação sobre a resolução e distorção espacial das reconstruções em função da posição da fonte e do número de fotões emitidos. Foi observado um bom acordo entre os resultados experimentais e os simulados.

O sistema foi usado para investigar diversas configurações relevantes para o projecto dedicado ao desenvolvimento de um detector de neutrões térmicos sensível à posição baseado num contador proporcional de cintilação com leitura óptica [1], no qual o nosso grupo participou. Em particular, o algoritmo da máxima verosimilhança foi usado para reconstruir eventos em casos de estudo que cobriam geometrias de detectores com reflexão de luz suprimida, com paredes cilíndricas feitas de materiais com diferentes propriedades de reflexão e com uma janela de vidro como interface entre a fonte de luz e os PMTs. Métodos para processamento de dados foram desenvolvidos para parametrizar as funções resposta dos PMTs a partir dos dados emulados. Os resultados obtidos demonstraram que a bancada de emulação pode ser usada de forma efectiva para desenhar e optimizar PSGSDs, visando a melhor resolução possível em posição e energia, assim como a mínima distorção espacial dos eventos reconstruídos.

A bancada de emulação pode também ser usada para emular sinais realistas para o teste da electrónica de leitura de PSGSDs em condições realistas, para estudar o desempenho de algoritmos de reconstrução de eventos ou para desenvolver técnicas adaptativas da resposta do detector como as apresentadas na referência [4]. O mesmo conceito pode ainda ser desenvolvido, com vista a aplicações que necessitam de comprimento de onda ajustável e controlo preciso das propriedades de emissão da fonte de luz. Esta abordagem poderá possivelmente ser estendida à emulação da luz de cintilação

em líquidos e sólidos, operando a fonte de luz num volume preenchido com um líquido com propriedades ópticas (e.g. índice de refracção) que corresponda ao do cintilador em estudo.

Acknowledgements

The same way a complex machine depends on many critical parts to complete a task, so did the work leading to this dissertation. It relied not only on my effort and perseverance, but also on the contributions of many other people that, over the last years, provided me with guidance, fruitful discussions, knowledge, motivation, inspiration, encouragement, advice and good moods.

I would like to thank my supervisor, Prof. Doutor Francisco Fraga for the encouragement, advice and for accepting to guide me under his supervision.

To Andrei Morozov, who is a colleague and a friend, for his continuous, unresting and unconditional support since the first moment we started working together many years ago.

I owe my deepest gratitude to the LIP-Coimbra directive board for the continuous support.

In general, I want to thank all members of LIP-Coimbra, in particular all the technical staff for being so helpful and from whom I've learnt so much.

To my colleagues, Luís Margato, Susete Fetal, Vladimir Solovov and Francisco Neves I have to say thank you for helping me with your knowledge and experience.

Thanks to all my friends for putting up with me, despite my bad mood and endless monologues about almost everything that exists in the universe and beyond.

I owe my deepest gratitude to Carla Margarida for her continuous support and for accepting the responsibility to submit this thesis on time while I was in Dresden.

I also thank Neide Ribeiro for being so cheerful and helpful.

I am grateful to my mother for her unlimited support and contagious laughter. I am also grateful to my sister Daniela Pereira and my niece Inês Marques for making my life more joyful.

Thanks to Claudia Ascher for sharing with me her wisdom and love.

This work was supported by the fellowship SFRH/BD/82505/2011 granted by the Portuguese Foundation for Science and Technology (FCT) under the program POPH/FSE.

Contents

List of Abbreviations

1D	one **D**imensional
2D	two **D**imensional
3D	three **D**imensional
ACEWrench	**A**cquisition and **C**ontrol of an **E**mulation **W**o**R**k**b**ENCH
ADC	**A**nalogue to **D**igital **C**onverter
ANTS	**A**nger-camera type **N**eutron detector: **T**oolkit for **S**imulation
APD	**A**valanche **P**hoto**D**iode
CCD	**C**harge **C**oupled **D**evice
CE	**C**ollection **E**fficiency
CERN	**C**entre **E**uropeén de **R**echerche **N**ucléaire
COG	**C**enter **O**f **G**ravity
DC	**D**irect **C**urrent
ENC	**E**quivalent **N**oise **C**harge
ENF	**E**xcess **N**oise **F**actor
FOV	**F**ield **O**f **V**iew
FWHM	**F**ull **W**idth at **H**alf **M**aximum
GEM	**G**as **E**electron **M**ultiplier
GPU	**G**raphic **P**rocessing **U**nit
GUI	**G**raphic **U**ser **I**nterface
HNN	**H**ardware **N**eural **N**etwork
HPD	**H**ybrid **P**hoto **D**etector
LAB	**L**inear**A**lkyl**B**enzene
LAC	**L**inear **A**ctuator **C**ontroller
LED	**L**ight **E**mmitting **D**iode
LRF	**L**ight **R**esponse **F**unction
LUX	**L**arge **U**nderground **X**enon
MCP	**M**icro **C**hannel **P**late
MIPS	**M**inimum **I**onizing **P**article **S**
ML	**M**aximum **L**ikelihood
MPPC	**M**ulti **P**ixel **P**hoton **C**outing
MSGC	**M**icro **S**trip **G**as **C**hamber
NEXT	**N**eutrino **E**xperiment with a **X**enon **T**PC

NIR	**N**ear **I**nfra **R**ed
NIST	**N**ational **I**nstitute of **S**tandards and **T**echnology
NN	**N**eural **N**etworks
OF	**O**ptical **F**iber
PD	**P**hoto**D**iode
PET	**P**ositron **E**mission **T**omography
PMMA	**P**oly(**M**ethyl**M**eth**A**crylate)
PMT	**P**hoto**M**ultiplier **T**ube
PSGSD	**P**osition **S**ensitive **G**aseous **S**cintillation **D**etector
PSP	**P**hoto**S**timulable **P**hosphor
PSU	**P**ower**S**upply **U**nit
PTFE	**P**oly**t**etra**f**luoro**e**thylene
QE	**Q**uantum **E**fficiency
RCA	**R**adio **C**rporation of **A**merica
RF	**R**adio **F**requency
RMS	**R**oot **M**ean **S**quare
SDC	**S**cintillation **D**rift **C**hamber
SER	**S**ingle **E**lectron **R**esponse
SiPM	**S**ilicon **P**hoto**M**ultiplier
SNO	**S**udbury **N**eutrino **O**bservatory
SRIM	**S**topping **R**ange of **I**ons in **M**atter
TLD	**T**hermo**L**uminescence **D**osimeter
TPC	**T**ime **P**rojection **C**hamber
UV	**U**ltra **V**iolet
VUV	**V**acuum **U**ltra **V**iolet
WIMP	**W**eakly **I**nteracting **M**assive **P**article

Introduction

Position sensitive gaseous scintillation detectors (PSGSD) with Anger type readout are being developed for use in various research areas such as neutron detection [1], search for dark matter [2] and neutrinoless double beta decay [3]. Using suitable gas mixtures the avalanches produced in these detectors can emit up to 10^6 photons/MeV in tens of nanoseconds, allowing to achieve high spatial resolution ($<1\,\mathrm{mm}$) and high count rate ($>1\,\mathrm{MHz}$) over large detection areas (in the order of thousands of cm^2).

Optical readout offers several advantages over charge readout: since electronics are decoupled from the detection media, they become insensitive to electronic noise or RF pickup signals coming from the detector media and housing; large areas can be covered with a high filling factor leaving nearly no dead spaces; using true pixel readout complex events can be recorded and real multi-hit capability is possible [5]. As disadvantages, optical readout typically adds complexity, size and cost to the detector design, and additionally it requires a suitable optical coupling between the photodetectors and the scintillation volume.

The design of new PSGSDs and optimization of existent ones in terms of resolution and image quality requires consideration of a large number of parameters, including number of emitted photons per event, characteristics of the photodetector array, light-scattering properties of the structural elements and the algorithm used in event reconstruction. Traditionally, optimization methods are based on iterative experimentation with the detector or involve Monte Carlo simulations. The first approach can be very time and resource consuming, while simulations, although a remarkable tool, do not often provide adequate results due to limitations in the model or lack of knowledge of many relevant parameters (e.g. optical properties of the detector components).

The main goal of this work is to study a different approach based on an experimental set-up capable of emulate scintillation events in gaseous scintillation detectors with optical readout, under controllable experimental conditions. This set-up can be a valuable investigative tool, since it is easily

configurable (as a Monte-Carlo simulation), while providing realistic experimental data (as a gaseous scintillation detector). It is, therefore, envisaged that it may facilitate design and optimization of PSGSDs while being capable to assist the development of new event reconstruction techniques. One of the first challenges to overcome during the construction of such a system was to manufacture a stable light source with simultaneously high degree of isotropy, small volume and pulse mode capability. These requirements were met growing a polymer diffuser at the end of an optical fiber coupled to a light emitting diode (LED). With this technique, $1\,\mathrm{mm}$ diameter diffusers were manufactured with isotropy better than $10\,\%$ over more than $> 3.5\pi$ solid angle. The light source was installed on a 3D high resolution positioning system covering $100\times100\times50\,\mathrm{mm}^3$ inside a light tight box with black inner walls to suppress light scattering. A holder on top of the box allows to quickly mount (and remove) cylindrical walls with different diameters and built using materials with different scattering properties. The optical readout consists of a hexagonal arrangement of seven, $38\,\mathrm{mm}$ diameter PMTs (Hamamatsu R1387) mounted on a frame on top of the box. The PMT signals are recorded using a charge sensitive ADC and the set-up is controlled using a custom LabVIEW [1] application developed to perform and automatize the most relevant tasks such as light source positioning, PMT signal monitoring, data acquisition and experimental data pre-processing. The light emission is adjustable in the range between $\sim 10^3$ and $\sim 10^6$ photons per pulse using the signal reading from a calibrated PMT and the duration of the light pulses can be set in the range between $\sim$1 ns and $\sim$1 s.

The whole experimental set-up was called *emulation workbench for position sensitive gaseous scintillation detectors* and will be referred hereafter as *emulation workbench*.

With this setup primary and secondary scintillation can be emulated since it is possible to adjust both position of the light source, as well as the number of emitted photons per pulse over a wide range of light yields. Moreover, this can be done in near real-time. Another strength of this setup is the possibility to easily change the geometry and the light scattering properties of the walls of the detector. The setup can be modified to study different types of photosensors and to characterize the performance with different geometries of the sensor array. It is also possible to add optical elements such as lightguides, lenses or windows. As an additional advantage, the setup can be used to test

[1] LabVIEW is the acronym for Laboratory Virtual Instrument Engineering Workbench which is a system-design platform and development environment for a visual programming language from National Instruments Corporation, Austin, USA.

the acquisition system and to perform a detailed characterization of the light detection properties of individual photosensors.

The preliminary validation runs were made with suppressed scattered light conditions, by recording the camera signals from events occurring at different locations and light intensities. The experimental data was processed using the center of gravity algorithm, due to its simplicity and robustness, and the results compared with those given by simulations made with the simulation and data processing package ANTS2 [6]. Measurements of the practical spatial resolution versus distance between the light source and the PMT plane are presented, as well as a study of the achievable spatial resolution versus the number of emitted photons.

The spatial response of individual PMTs (the so called light response function (LRF)) was experimentally measured with different light scattering conditions. The maximum likelihood algorithm was used to investigate event reconstruction both without and with the presence of highly scattering materials namely PTFE (high diffuse reflectance) and aluminized Mylar (high specular reflectance). The effect of a $10\,\mathrm{mm}$ glass window interfacing the PMTs and the light source was studied for light source positions located in plane at $10\,\mathrm{mm}$ distance from the plane of the PMTs. The optical properties of the PTFE surface and the glass window were estimated by fitting experimental data with data obtained from simulated models. The process consisted in interactively changed the parameters of the simulated model providing the best fit between the experimental and the simulated data. Moreover, the prevision capability of the model parameterization can be tested with data acquired at the emulation workbench under different geometrical conditions. The organization of this thesis comprises seven chapters, an Introduction and Conclusions. In the Introduction the structure, the scientific framework and the purpose of the thesis are presented. Chapter 1 addresses the fundamental concepts of interaction of radiation with matter and the principles of radiation detectors, including some major breakthroughs in radiation detection with emphasis on the development of gaseous scintillation detectors. Chapter 2 describes relevant characteristics of photomultiplier tubes (PMTs). This type of photodetectors was chosen to the 2D position sensitive gas scintillation detector for thermal neutrons developed under the European FP7 NMI3 JRA program (Project 226507) [1] which triggered the main investigation line of the thesis. Moreover PMTs are still widely used in many applications, particularly those involving low light level detection. Chapter 3 addresses techniques used to reconstruct events from photodetector signals, namely

the center of gravity method, statistical algorithms based on maximum likelihood estimation and neural networks. The construction details and the calibration procedures of the emulation workbench are presented in chapter 4 and chapter 5, respectively. The ANTS2 simulation and data processing package, which was intensively used during this work, is briefly presented in chapter 6. Chapter 7 is dedicated to present some relevant cases studied with data acquired with the emulation workbench. In the Conclusions the goals achieved are presented and ways to improve the emulation workbench capabilities, as well as possible target applications, are going to be pointed out.

Chapter 1

Radiation detection

In this chapter an overview of the fundamental concepts regarding gas scintillation detectors is given, including the fundamental physical phenomena, history, structure and some recent developments.

1.1 Interaction of radiation with matter

This section was written mostly following well known classical text books namely Knoll [7] and Leo [8].

1.1.1 Charged Particles

Heavy particles

In matter, the interaction of heavy charged particles, such as an alpha particle ($^4_2\mathrm{He}^{2+}$), is mediated through the coulomb force between their positive charge and the negative charge of the orbital electrons within the absorber atoms. The differential energy loss for a particle within a certain material is given by its linear stopping power S

$$S = -\frac{dE}{dx} \tag{1.1}$$

here E is the energy of the particle and x the path length. The value $-dE/dx$, along a particle track, is called the *specific energy loss*. The classical expression describing the specific energy loss is known as the *Bethe formula* and is as follows

$$-\frac{dE}{dx} = \frac{4\pi e^4 z^2}{m_0 v^2} NB \tag{1.2}$$

where

$$B = Z\left[ln\frac{2m_0v^2}{I} - ln\left(1-\frac{v^2}{c^2}\right) - \frac{v^2}{c^2}\right].$$

In the expression above v and ze are the velocity and charge of the primary particle, N and Z are the number density and atomic number of the

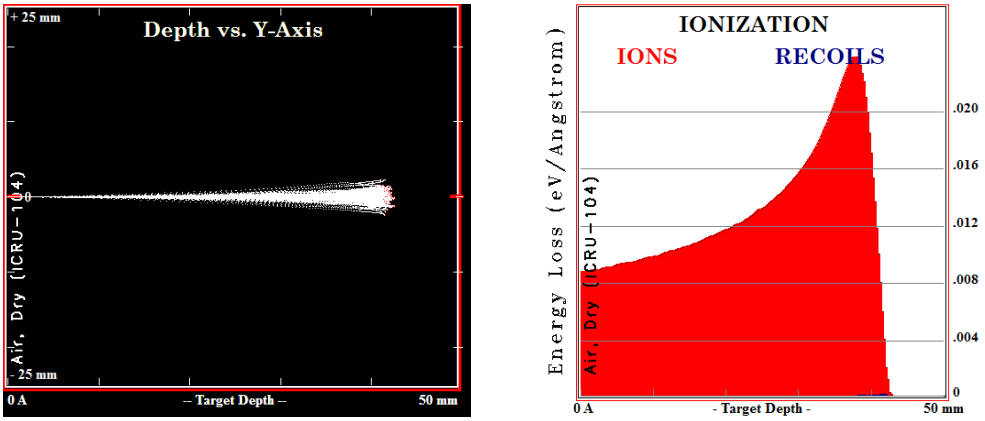

FIGURE 1.1: Simulated data relative to the interaction of $5.5\,\mathrm{MeV}$ alpha particles with air molecules at atmospheric pressure. The simulation was performed using the simulation package SRIM. Left: Particle track. Right: Energy deposition by ionization along the particle track.

absorber atoms, m_0 is the electron rest mass, and e is the electron charge. Parameter I represents the average excitation and ionization potential of the absorber, which is normally treated as an experimentally determined parameter. According to the Bethe formula, the stopping power is proportional to the density and atomic number of the absorber material. It depends also on the characteristics of the incident particles (rest mass, velocity and charge). In the non-relativistic regime the stopping power decreases with the square of the velocity of the incident particle, which means that as it slows down, it loses more and more energy. When the velocity of the particle is approximately $0.96c$, the stopping power exhibits a minimum. At this point such particles are termed MIPS from *Minimum Ionizing ParticleS*. For $v > 0.96c$, the stopping power increases again as $v/c \to 1$ and ln term rises slowly. Highly relativistic particles start to lose energy much more rapidly due to radiation losses and are out of the Bethe range. In figure 1.1, simulated data obtained using the simulation package SRIM[1] is depicted showing the tracks of $5.5\,\mathrm{MeV}$ alpha particles in air at atmospheric pressure. The plot of the specific energy loss of alpha particles, such as the one shown in figure 1.1(right), is known as a *Bragg curve*. The specific energy loss increases roughly with $1/E$ as predicted by the Bethe formula up to the *Bragg peak*. Near the end of the track, electron pickups effects reduce the charge of the particle and the curve falls off. Since the energy transfer between the particle and the absorber is a statistical or stochastic process, a spread always results after a

[1]SRIM (Stopping and Range of Ions in Matter) is a software package developed by James F. Ziegler and available at http://srim.org/.

beam of monoenergetic charged particles has passed through a given thickness of absorber. This effect is commonly referred to as *energy straggling*. The range R of an heavy charged particle (see figure 1.1 (left)) can be determined from the Bragg curve by integrating $(dE/dx)^{-1}$ between the initial energy of the particle E and zero i.e.

$$R = \int_0^E \left(\frac{dE}{dx}\right)^{-1} dE \tag{1.3}$$

For a beam of heavy charged particles the range in an absorber material is commonly defined as the absorber thickness that reduces the alpha particle count to exactly one half of its value in the absence of the absorber. The same stochastic factors that lead to the energy straggling at a given penetration distance also result in slightly different total path lengths for each particle, which is called *range straggling*.

Electrons

In general electrons lose energy at a lower rate and follow much more complex paths than heavy particles. The large deviations in path are possible because their mass is equal to that of the orbital electrons with which it is interacting, and a much larger amount of energy can be lost in a single encounter. In addition, electron-nuclear interactions, which can abruptly change the electron's direction, sometimes occur. The specific energy loss for electrons is as follows

$$-\left(\frac{dE}{dx}\right)_{collisional} = 2\pi N r^2 \tau \rho \frac{Z}{A\beta^2}\left[ln\left(\frac{\tau^2(\tau+2)}{2(Ilm_0c^2)}\right) + F(\tau)\right] \tag{1.4}$$

where the symbols have the same meaning as in equation 1.2 and $\beta \equiv v/c$. Electrons also lose energy along the track with the emission of electromagnetic radiation (bremmstrahlung). The linear specific energy loss through this radiative process is

$$-\left(\frac{dE}{dx}\right)_{radiative} = \frac{NEZ(Z+1)e^4}{137m_0^2c^4}\left(4ln\left(\frac{2E}{m_0c^2}\right) - \frac{4}{3}\right) \tag{1.5}$$

The factors E and Z^2 in the numerator of 1.5 show that radiative losses are most important for high electron energies and for absorber materials of large atomic number. For typical electron energies, the average bremsstrahlung photon energy is quite low and is therefore normally reabsorbed fairly close to its point of origin. In some cases, however, the escape of bremsstrahlung

can influence the response of small detectors. The total linear stopping power for electrons is the sum of the collisional and radiative losses

$$\frac{dE}{dx} = \left(\frac{dE}{dx}\right)_{collisional} + \left(\frac{dE}{dx}\right)_{radiative} \tag{1.6}$$

The ratio of specific energy losses is given approximately by

$$\frac{(dE/dx)_{radiative}}{(dE/dx)_{collisional}} \simeq \frac{EZ}{700} \tag{1.7}$$

where E is in units of MeV. Therefore, for electrons with energy up to a few MeV, radiative losses are significant only in absorber materials with high atomic number [7].

1.1.2 Photons

Among other interaction mechanisms for the interaction of photons with matter, the following three play an important role in the context of radiation detection: photoelectric effect, Compton scattering and pair production.

Photoelectric effect

When a photon interacts with an atom through photoelectric effect, an energetic photoelectron is ejected from one of its bound shells and the photon disappears. The ejected electron, also known as photoelectron, appears with an energy given by

$$E_{e-} = h\nu - E_b \tag{1.8}$$

where E_b represents the binding energy of the photoelectron in its original shell. The photoelectrons are predominantly from the inner atomic shells i.e K, L or M and carry the difference between the energy of the photon and the electron binding energy. Therefore, in order for the photoelectric effect to occur, the energy of the photon must be larger than the binding energy of the emitted electron. The probability of photoelectric effect occurring is described by the *photoabsorption efficience* τ. It depends on the material density ρ and on the atomic number Z. No single analytic expression is valid for the probability of photoelectric absorption over all ranges of energy and atomic number [7], but a rough approximation is given by

$$\tau \propto \frac{Z^n}{E^{3.5}} \tag{1.9}$$

where the exponent n varies between 4 and 5 over the gamma-ray energy region of interest. This severe dependence of the photoelectric absorption probability on the atomic number of the absorber is a primary reason for the preponderance of high-Z materials (such as lead) in gamma-ray shields.

Compton scattering

Compton scattering refers to the inelastic interaction between a photon and an electron in the absorbing material. The incoming photon is deflected through an angle θ with respect to its original direction as it transfers a portion of its energy to the electron (assumed to be initially at rest). Since there are no restrictions to the possible angles of scattering, the energy transferred to the electron can vary from zero to a large fraction of the photon energy. For any given interaction it can be shown that the energy of the outgoing photon $h\nu'$ relates to the energy of the incoming photon $h\nu$ as follows

$$h\nu' = \frac{h\nu}{1 + \frac{h\nu}{m_0c^2}\left(1 - cos(\theta)\right)} \tag{1.10}$$

where m_0c^2 is the rest mass-energy of the electron ($0.511\,\mathrm{MeV}$). For small scattering angles, $\theta \approx 0 \rightarrow h\nu' \approx h\nu$ i.e. little energy is transferred. Even in the extreme case of $\theta = \pi$, some of the energy is always retained by the incoming photon.

The probability of Compton scattering per atom of the absorber depends on the number of electrons available as scattering targets and therefore increases linearly with the atomic number Z. The angular distribution of scattered photons is predicted by the $Klein-Nishina$ formula for the differential scattering cross section $d\sigma/d\Omega$,

$$\frac{d\sigma_C}{d\Omega} = Zr_0^2 \left(\frac{1}{1+\alpha(1-cos\theta)}\right)^2 \left(\frac{1+cos^2\theta}{2}\right) \left(1 + \frac{\alpha^2(1-cos\theta)^2}{(1+cos^2\theta)([1+\alpha(1-cos\theta)])}\right) \tag{1.11}$$

which reveals the strong tendency of forward scattering with increasing photon energy[2].

Pair production

The conversion of a photon in an electron-position pair is energetically possible if the photon energy exceeds twice the rest-mass energy of an electron ($1.02\,\mathrm{MeV}$). In the interaction, which must take place in the Coulomb field of

[2] A detailed discussion of the Compton effect can be found in reference [9].

a nucleus, the photon is converted to an electron-position pair. All the excess energy carried by the photon above the $1.02\,\mathrm{MeV}$ required to create the pair goes into kinetic energy shared by the positron and the electron. The positron has a very short range in matter and will subsequently annihilate, normally producing two photons as secondary products of the interaction. The probability of pair production per nucleus varies approximately with Z^2 and the importance of pair production rises sharply with the photons' energy.

1.1.3 Neutrons

Neutrons lack electric charge and are only weakly absorbed by most materials. The kinetic energy of a neutron E_k, is given by the *De Broglie relationship*

$$\lambda = \frac{h}{mv} \tag{1.12}$$

where λ is the De Broglie wavelength, m and v are respectively the mass and velocity of the neutron and h is the Planck's constant. The neutron kinetic energy of the neutron is then given by

$$E_k = \frac{1}{2}mv^2 = \frac{h^2}{2m\lambda^2}. \tag{1.13}$$

As neutral particles, neutrons can only interact with nuclei either in elastic or inelastic collisions, or else be captured triggering a nuclear reaction. The predominant interaction type (scattering or nuclear) is determined by the energy of the neutron and the nature of the target material. Inelastic scattering occurs at all energies, and allows slowing down of energetic neutrons. The designation *thermal neutrons* is used for neutrons with average energy similar to the surrounding medium at room temperature i.e. 0.025 eV (as given by the Maxwell-Boltzmann distribution of velocities). In general, the neutron absorption cross section reduces with energy for several materials (see figure 1.2). Since thermal neutrons have wavelengths in the order of 1 Å, which is about the size of the typical separation between atoms in a solid material, they are used in neutron diffraction experiments.

A nuclear reaction caused by the absorption of a neutron is immediately followed (usually on the picosecond time scale) by the emission of a gamma photon or a heavy particle. Gamma emission is by far more common; nevertheless, the emission of a heavy particle is the most important process for neutron detection. In fact, the detection of a heavy particle such as an alpha particle or a proton is usually a much more efficient process than that

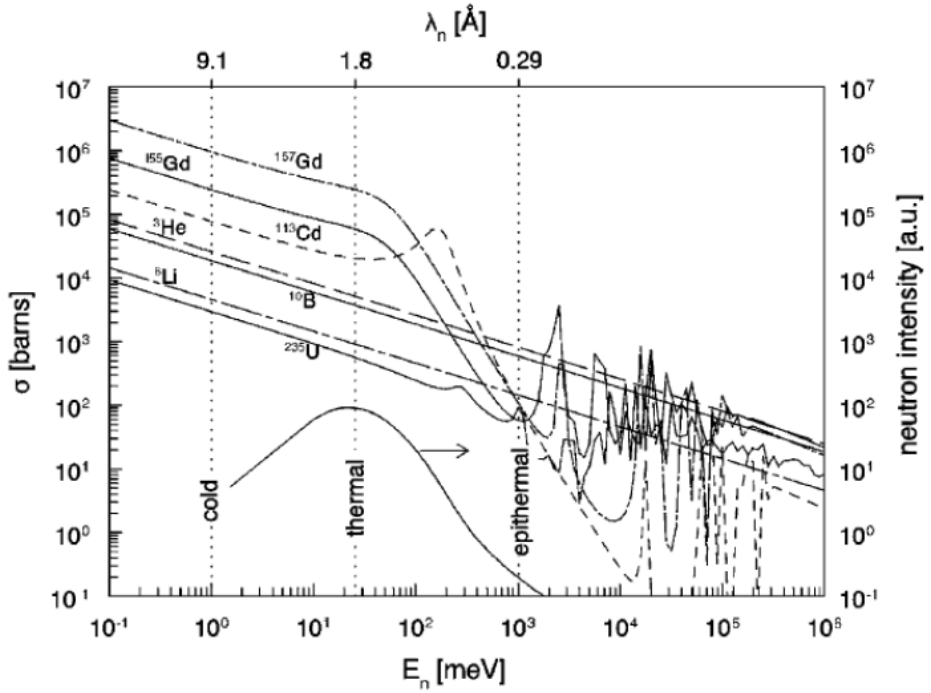

FIGURE 1.2: Cross section for the interaction of neutrons with several relevant nuclei.

of a gamma photon. In table 1.3 the most common reactions used for neutron detection are listed. In all cases the reaction is so energetic that even for a thermal neutron the outgoing projectile has a total energy of the order of $1\,\mathrm{MeV}$. Moreover, for light nuclei, the recoil energy will not be negligible with respect to the energy of the outgoing projectiles.

$^{3}He + n \rightarrow {}^{3}H + p + 0.77MeV$

$^{6}Li + n \rightarrow {}^{3}H + {}^{4}He + 4.79MeV$

$^{10}B + n \rightarrow {}^{7}Li^{*} + {}^{4}He \rightarrow {}^{7}Li + {}^{4}He + 0.48MeV\,\gamma\text{ ray } + 2.3MeV\,(93\%)$
$\rightarrow {}^{7}Li + {}^{4}He + \qquad 2.79MeV\,(7\%)$

$^{157}Gd + n \rightarrow Gd^{*} \rightarrow \gamma$ ray spectrum $\rightarrow$ conversion electron spectrum up to 182 KeV

$^{235}U + n \rightarrow$ fission fragments $+ \sim 80MeV$

$^{239}Pu + n \rightarrow$ fission fragments $+ \sim 80MeV$

FIGURE 1.3: Some important reactions in the context of neutron detection.

1.2 Radiation detectors

Among several other relevant references that will be given throughout this section, the historical perspective starting in the primordials of radiation detection was mostly based on the work of F.N. Flakus "Detecting and measuring ionizing radiation - a short history" [10]. More specifically, many details concerning scintillation counting were obtained from the "The theory and practice of scintillation counting" from John B. Birks [11].

During the whole history of mankind, ionizing radiation has been present in nature, either from extra-terrestrial sources (cosmic rays) or from naturally occurring radioactive materials. However, contrary to what happens with visible radiation, human beings have no specific sense capable of perceiving ionizing radiation and consequently it remained unnoticed until more than 100 years ago. The sequence of extraordinary scientific achievements that led humanity to unveil the nature, measure and control the effects of ionizing radiation can be traced back to the pioneering works of W. C. Röntgen (discovery of X-rays, 1895) and H. Becquerel (discovery of radioactivity, 1896). The discovery of X-rays by Röntgen was in fact due to the presence of an "accidental" radiation detector made of cardboard coated with barium platinocyanide placed close to an Hittorf-Crookes discharge tube. Röntgen, noticed that the cardboard flickered greenish light, correlating to the discharges. Subsequently, Röntgen replaced the fluorescence screen by a photographic plate and the X-ray radiography was born. The discovery of radioactivity in 1896, also happened somewhat accidentally, while Becquerel was experimenting with phosphorescent substances placed in photographic plates. On one occasion, he found dark spots on a plate placed in a drawer under a tray with uranium salts and correctly interpreted that they were cause by some kind of invisible rays which were at first named Becquerel rays and later generically renamed radioactivity by Madame Skłodowska Curie. Among other important facts, Becquerel found that these rays discharged a charged electroscope which contributed to the search for further radiation emitting elements. It was discovered early that X-rays had the ability to make dry air electrically conductive, i.e. to liberate electrical charges in air. The charges could be collected by producing an electric field across that volume in air. These facts led to the development of the first ionization chambers.

The development of radiation detectors based either on its luminescence or ionization effects is interconnected, as often developments in one led to

new perspectives in the other, as will be described hereafter in a short historical note about the development of radiation detectors with a particular focus on scintillation based detectors.

1.3 Historical note

As stated, the discovery of the X-rays by Röntgen is in fact connected to the correct interpretation of the result given by a fluorescent target which accidentally acted as a radiation detector. During this early era, radiation detection using fluorescent targets saw subsequent improvements in the form of fluoroscopes by W.F. Magie, E.P. Thomson and T.A. Edison [12]. Despite the capability of these devices for producing real time moving images, health hazards and poor resolution dictated its loss of importance at least until the development of suitable optical sensors.

In 1903 a sequence of events following the accidental spill of radium bromide over a zinc sulfide screen led William Crookes to invent the first instrument capable of detecting individual rays: the spinthariscope. This instrument, the first radiation counter, was used e.g. by Rutherford as late as the 1930s. However, counting individual scintillations was tedious work and the counting was very stressful for the eyes. It was the invention of the photomultiplier tube in 1940s that finally allowed the weak light flashes from scintillators to be easily detected, making counting by eye (as happens with the spintharoscope) obsolete. In the late 40s, several good solid scintillators were found, among them the thallium-activated sodium iodide crystal (NaI(Tl)) which was discovered in 1948 and became commercially available in 1950, and is still widely used today due to it's characteristics, namely wavelength of maximum emission ($415\,\mathrm{nm}$), decay time ($230\,\mathrm{ns}$) and number of emitted photons per MeV deposited (38000) [7].

Liquid scintillation detectors were reported in 1948, but interest in these detectors did not develop until the 1960s. Some noble gases, when condensed as a cryogenic liquid or solid, are also observed to be quite efficient scintillators with emission typically in the VUV range [7]. Liquid xenon, for example, can be effectively used to detect gamma radiation due to its high atomic number of 54. Additionally, in certain liquid scintillators there is a large difference in the relative slow component induced by different radiations, so that very effective pulse shape discrimination is possible between particles types [7].

As already outlined, using photographic plates to record ionizing radiation dates back to the discovery of X-rays and radioactivity. In later years, special photographic emulsions were developed to be used for special purposes, either to X-ray radiography or, as in the case of nuclear emulsion, to observe individual nuclear tracks. Photographic film was used until as recently as the 1990s as a 2D radiation detector (e.g. diffractrometry). Image plate, a photostimulable phosphor (PSP) plate developed in the early 1980s, allowed the signature of X-ray to be stored as a photographic plate. The radiation footprint was typically read using a visible light source and a scanning device. Unlike a photographic plate, image plates could be erased and used over and over.

Thermoluminescece, i.e. the phenomenon by which a material after being exposed to radiation will release the accumulated energy upon heating, was first described by Boyle in 1663 and later by Wick in 1927-1928. An example of such a material is LiF which came into large scale use as a personnel dosimeter in 1966 after the studies started by L.F Heckelberg in 1948. Among others, this type of dosimeter, the thermoluminescent dosimeter (TLDs) is gradually replacing film based badge dosimeters.

The ionization properties of ionizing radiation were used in visual detectors used in some of the most important discoveries of particle physics, among which the cloud chamber, invented by Wilson circa 1911, the bubble chamber invented in 1952 by Donald A. Glaser and the streamer chamber invented in the early 1960s by G. E. Chikovani [13] and B. A. Dolgoshein [14] as a result of the development of spark and discharge chambers. The early observations that radiation discharged an electroscope and that X-rays had the ability to make dry air electrically conductive led to the development of the first ionization chambers. Simple ionization chambers were in fact an essential tool in the early studies of X-rays and a famous example of its usage by Victor F. Hess was the results obtained with an ionization chamber aboard an high altitude balloon, which in 1910 provided the first evidence of cosmic rays. Between 1908 and 1913 Rutherford and Geiger made further developments in counters both for alpha and beta particles. It was in 1928 that Geiger and Muller introduced a new gas filled detector: the Geiger-Muller counter (GM), capable of response to individual radiation induced events with a high level output signal. This device was further developed and found wide use until the present day due to its simplicity, ease of operation and low cost. In the 1940s there were new developments with the gridded ionization chamber by Frisch and in the late 1940s the *proportional counter* was invented by

Samuel Curran which amplified the charge originating in the gas [15]. One important application of proportional counters has therefore been in the detection and spectroscopy of low-energy X-radiation [7]. Today proportional counters are still widely used in many laboratories for alpha or beta radiation measurements. In fact, the GM and the proportional counter are the same basic instrument but working under different operation parameters, exploiting different phenomena [8]. In 1968, Georges Charpak while working at European Organization for Nuclear Research (CERN) invented the multi-wire proportional chamber. This type of detector was position sensitive and had a much higher detection rate ($\sim$1 kHz) than the bubble chamber ($\sim$1 Hz) and soon replaced bubble chambers as it could be linked to a computer so that data did not need to be physically examined in the same way as photographs from the bubble chambers.

During the 1990s, some techniques originally introduced in the semiconductor industry led to the development of a new type of gas-filled detectors generally classified as micropattern gas detectors. They are characterized by having microscopic structures permitting high spatial resolutions, excellent time characteristics and high rate operation capability. Among many design variations are for example the microstrip gas chamber and the gas electron multiplier. Solid state semiconductor ionizing radiation detectors emerged only in the late 1950s and early 1960s. This type of detectors developed rapidly due to its detecting capabilities and the fact that its dimension could be kept much smaller than those of equivalent gas-filled detectors. These detectors typically have very good energy resolution and relatively fast timing characteristics. However, they are usually limited to small sizes and have relatively high performance degradation due to radiation-induced damage.

1.4 Gas filled scintillation detectors

According to reference [11], the first gas scintillation counter was developed by Grün and Schopper in 1951. The scintillations resulting from the excitation of a gas were counted with a PMT through a quartz window and a Plexiglas[3] light guide. The strongest scintillation pulses were obtained with nitrogen and with argon mixed with 2% nitrogen and corresponded to about 1000 photons/MeV between 300 and 400 nm wavelength for 5 MeV alpha particles. Due to the fast scintillation pulses an application for the triggering

[3]Plexiglas is a commercial name of methyl methacrylate (PMMA) a transparent thermoplastic.

of cloud chambers was envisaged. The efficiency of the scintillation counter was improved by Muehlhause in 1953 using a wavelength shifter to convert the UV component to the wavelength range compatible with the PMT sensitivity. Furthermore he suggested that scintillation efficiency in gases should be practically independent of the stopping power thus giving a linear response for heavy ions. He also estimated the decay time of a gas to be in the order of 10×10^{-9} second or less. It was in the late 1950s and early 1960s that Lydie Koch studied the influence of an electric field in the luminescence of xenon at atmospheric pressure excited by $4.7\,\mathrm{MeV}$ alpha particles [11]. She found a large increase of the scintillation pulse height with an applied electric field larger than $100\,\mathrm{V/cm}$ i.e. a light amplification effect. She also realized that the scintillation signal consists of two components, a prompt primary component, not affected by the applied electric field, and a secondary component delayed relatively to the primary component. While the primary component was attributed to the direct excitation of the gas molecules the secondary component was attributed to the excitation of the gas by accelerated electrons on the electric field. This findings led to the introduction of a new type of detector by Policarpo and Conde [16], based on the fact that electron drifting in gases under an electric field may produce detectable radiative excitation of atoms of the gas without the production of any charge multiplication. According to Charpak in reference [17] the work from Policarpo et al. in reference [18] was a real breakthrough in the field of particle detection with improvements over the operation in charge amplifying that could be summarized as follows: a) The amount of light produced per unit energy deposited in the gas is much larger than in a sodium iodine crystal (NaI); b) The suppression of the fluctuation proper to the charge amplification process lead to much better energy resolution; c) The absence of space charge effects leads to a high-rate capability $\sim 10^5$ counts per second. By the end of 1970s the scintillation drift chamber (SDC) was invented by Charpak, Ngoc, and Policarpo and registered in the US Patent Office in 1981 [19]. The confirmation of the remarkable properties of this type of particle detector came shortly after in a series of works, of which an example the 1975 paper from Conde found in reference [20] is an example. In reference [17], Charpak foresaw a series of applications for these type of detectors that would be materialized in subsequent developments. To name a few he claimed the advantage of this method over solid scintillators since the properties of the light pulses may be controllable in terms of intensity and duration. He also envisaged the possibility of using an array of photodetectors to attain bi-dimensional

read out (as happens in an Anger camera [21]) and referred to the self triggering capability that could be used in the localization of neutral particles such as neutrons and X-rays. From this time on, further new developments improved the performance of gaseous proportional scintillation counters as a result of the advances in optical imaging, research on the scintillating properties of gases, the appearance of electron multiplication microstructures such as GEM [22] and the microstrip gas chamber [23] that could also be used to produce light multiplication. A few recent examples are for example the X-ray Imaging detector based on GEM scintillation light [24]. In this detector, the light amplification was made using a GEM and the scintillation light was viewed with a CCD (charged coupled device). A similar detector design but filled with a $^3\mathrm{He} - \mathrm{CF}_4$ mixture was also successfully used in neutron detection [25]. Another design with light amplification made using a microstrip gas chamber plate instead of a GEM was proposed by Manzin [26]. More recently, these researches led to the development of a 2D position sensitive gas scintillation detector for thermal neutrons [1]. This detector was operated with a $^3\mathrm{He} - \mathrm{CF}_4$ mixture, the light multiplication was made using a microstrip and the optical readout was made using the Anger camera principle [21] with a planar array of PMTs.

1.4.1 Operation principles of gaseous scintillation detectors

In this section a short overview of the fundamental operation principles of gaseous scintillation detectors is presented, with particular attention to the primary and secondary light yield, time characteristics and optical readout. Attractive features of these detectors are that it is generally simple to obtain a 2π or even 4π geometry and their scalability in terms of size and scintillator volume. Moreover, varying the gas pressure it is possible to adjust the detector performance allowing for example a reduction of the detector sensitivity to more penetrating particles.

1.4.2 Primary scintillation

When ionizing radiation passes through a gas it may result in the ionization and excitation of its molecules. The excited molecules return to the ground state either dissipating energy by non-radiative quenching processes or by radiative emission of photons, which occur in the visible and ultraviolet range. The light emitted from such a process is commonly known as the *primary scintillation*. The primary process of excitation and ionization is quite

insensitive to the nature and energy of the ionizing radiation, being near linear over a wide range of energies and stopping powers [11].

A gaseous scintillation detector is shown schematically in figure 1.4. It consists of a gas filled vessel with a radiation entrance window, transparent optical window (for the relevant scintillation light wavelength range) and a photodetector. The primary light is emitted isotropically along the path of

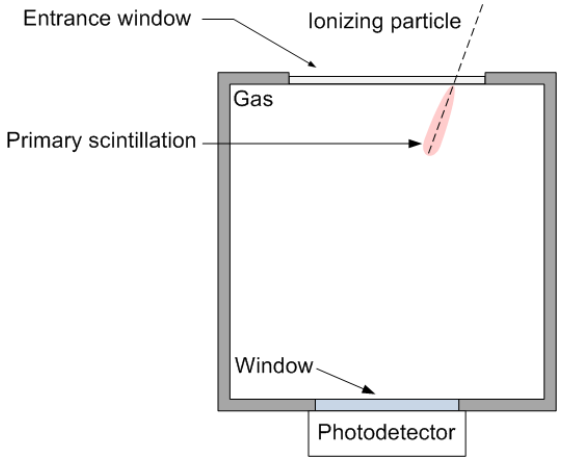

FIGURE 1.4: Schematic representation of a gaseous scintillation detector. The scintillation light is generated along the ionizing particle track.

the ionizing radiation in the gas. The spatial profile of the scintillating gas volume depends on the nature of the ionization particle, the filling gas and its pressure. This type of simple detectors was used in many early gas studies, for example reference [27], and it was observed that the light yield from nitrogen and argon was about 100 times greater than for example hydrogen, oxygen or carbon dioxide. This envisaged the technical interest in nitrogen and the inert gases as potential scintillators. The light yield and the mean wavelength of emission of some gases is given in table 1.1.

TABLE 1.1: Light yield of some gases excited by $4.7\,\mathrm{MeV}$ alpha particles measured at P = $1\,\mathrm{bar}$. The given wavelength corresponds to the mean wavelength of the emitted light above $200\,\mathrm{nm}$. The light yield of NaI(Tl) is shown for comparison purposes.

Gas	Wavelength (nm)	N. of photons
Xenon	325	3700
Krypton	318	2100
Argon	250	1100
Helium	390	1100
Nitrogen	390	800
NaI(Tl) (for comparison)	415	41000

As can be seen from table 1.1 the primary scintillation light yield of xenon is about ten times smaller than that of NaI(Tl), compromising the usage of primary scintillation in position sensitive detectors. However, as light emission in gases typically occurs within the nanosecond range, gaseous scintillators may represent an attractive solution when the goal is to have very high count rate ($> 1 \times 10^5$ counts per second).

1.4.3 Secondary scintillation: light amplification by an electric field

In the presence of an electric field, the free electrons created along the track of the ionizing particle through the gas will drift, following the field gradient towards the highest potential (see figure 1.5). If the electric field is strong enough, the energy of the electrons may be sufficient to excite some molecules of the gas through collisional excitation which then may return to the ground state, emitting light commonly known as *secondary scintillation light*. This is the fundamental mechanism for the operation of a gas propor-

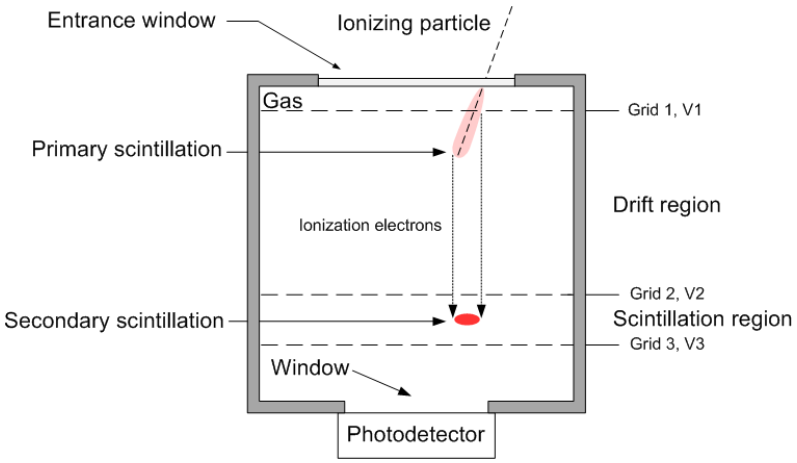

FIGURE 1.5: Schematic representation of a gaseous scintillation detector with light multiplication by an electric field. The relationship between the potential of the grids is as follows: V3>V2>V1.

tional scintillation counter. The schematic representation of such a detector is shown in figure 1.5 where two regions are delimited: the *drift region* and the *scintillation region*. In the drift region, the free electrons generated by the interaction of the ionizing particle with the gas molecules drift to the scintillation region due to the presence of an electric field (the *drift field*) generated by the applied voltage difference between grid 1 and grid 2 $\Delta V_{Driftregion} = V2 - V1 > 0$. In the scintillation region electrons excite the gas molecules due to the presence of a stronger electric field between grid 2 and grid 3 which

are kept at a potential difference $\Delta V_{Scintillationregion} = V3 - V2 > \Delta V_{Driftregion}$, with V2 and V3 the respective electric potential of grid 2 and grid 3. Therefore, the light output of such a detector consists on a prompt signal (primary scintillation) and a delayed signal due to light emission in the scintillation region (secondary scintillation). The secondary scintillation yield can be several orders of magnitude greater than the equivalent output from the standard scintillator NaI(Tl). In fact, a single primary electron could in principle produce an unlimited number of secondary photons, if the high-field region (scintillation region in figure 1.5) is extended indefinitely [7]. In the context of proportional scintillation counters, it is common to state that there is *light amplification* in the scintillation region. A major advantage of a gas scintillator over a solid scintillator is the fact that the light yield in a gas scintillation proportional counter can be controlled, i.e. the light amplification can be controlled. The time delay between the primary scintillation signal and the secondary signal depends on the drift velocity of the electrons for the particular detector geometry and gas filling[4]. The scintillation decay time of the secondary light may also be very fast. In CF4 for example, Margato [29] showed that at least 90% of the secondary light is emitted with a characteristic decay time of $15\,\mathrm{ns}$ or shorter and that the slowest component has a typical decay time of about $40\,\mathrm{ns}$. These facts, combined with the relative large light yield, make CF_4 a very attractive medium for high count rate imaging detectors with optical readout.

1.4.4 Micropattern gas detectors

In the early 1990s, a new category of gas filled devices appeared, collectivelly classified as *Micro-Pattern Gas Detectors* (MPGD) [30]. To this class of detectors belong the gas electron multiplier (GEM) detector [22] and the microstrip gas chamber (MSGC) [23] which have found applications in proportional scintillation counters (e.g. [24], [1]). Light amplification using a GEM occurs at the region of the holes (see figure 1.6), where the electric field lines converge attaining values as high as some tens of kV/cm over a distance of some tens of microns. Figure 1.7 (left) shows the setup used by Fraga at al. [24] to record the luminescence in a position sensitive X-ray detector using a GEM plate (see figure 1.7 (right)). Due to the high density of holes in a

[4]As an example, the drift velocity of CF4 (which is a gas with a relatively large drift velocity) is larger than $1 \times 10^7\,\mathrm{cms}^{-1}$ at a reduced field E/N = $10 \times 10^{-17}\,\mathrm{Vcm}^2$. Thus, under these conditions the delay between the primary and secondary light would be under $1\,\mu\mathrm{s}$, assuming a distance of $\approx 10\,\mathrm{cm}$ between the two scitillation events [28]

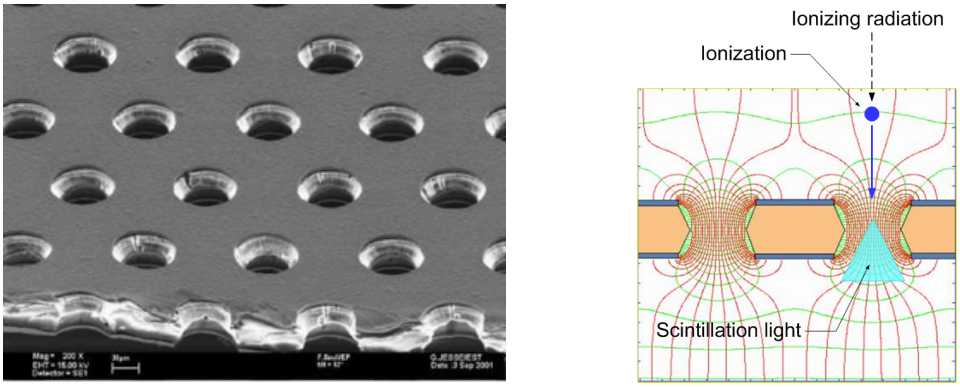

FIGURE 1.6: Left: Electron microscope image of a GEM electrode. Right: Field and equipotential lines near the GEM holes (original images retrieved from http://fabio.home.cern.ch/fabio/. The scintillation light was added by the author).

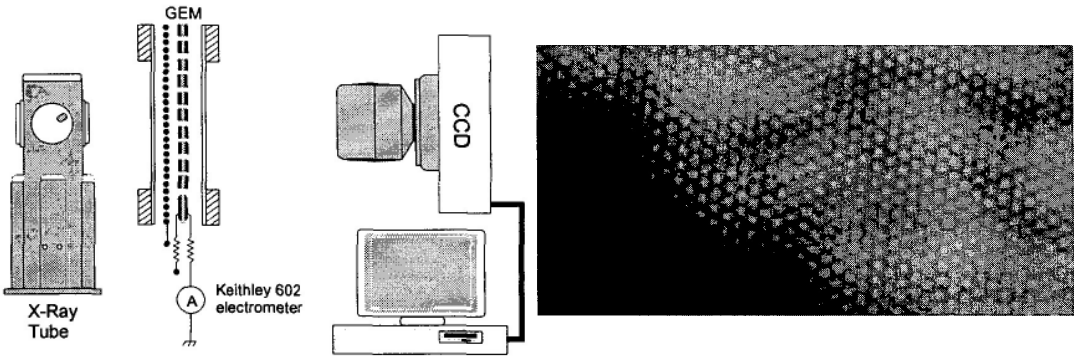

FIGURE 1.7: Left: Schematic drawing of the experimental system (image retrieved from reference [24]). Right: Image of the scintillation light produced by the GEM avalanches in a small irradiated zone (the distance between two adjacent holes is $140\,\mu m$. Image retrieved from reference [24].

GEM (typically around 50 - 100 mm^{-2}), and since the secondary light emission occurs within a few microns of the holes, these detectors can be used in combination with a suitable optical readout to attain relatively high spatial resolution (see figure 1.7).

The luminescence from the microstrip gas chamber (MSGC) (see figure 1.8) was reported in 1993 by Geltenborg et al. [31]. The secondary light is emitted in the vicinity of the anodes, where the electric field is stronger and electrons gain sufficient energy to excite the gas molecules and produce a strong scintillation. Figure 1.9 (left) shows a photograph of the visible component of secondary scintillation from a MSGC irradiated with alpha particles. The red glow at the anodes corresponds to the emission of the CF_4 in the visible range (500 to $800\,nm$) [32]. As can be seen in figure 1.9 (right) showing the visible light emission profile at one of the anodes of a MSGC, the secondary scintillation light is emitted close to the anode. Due to the nature

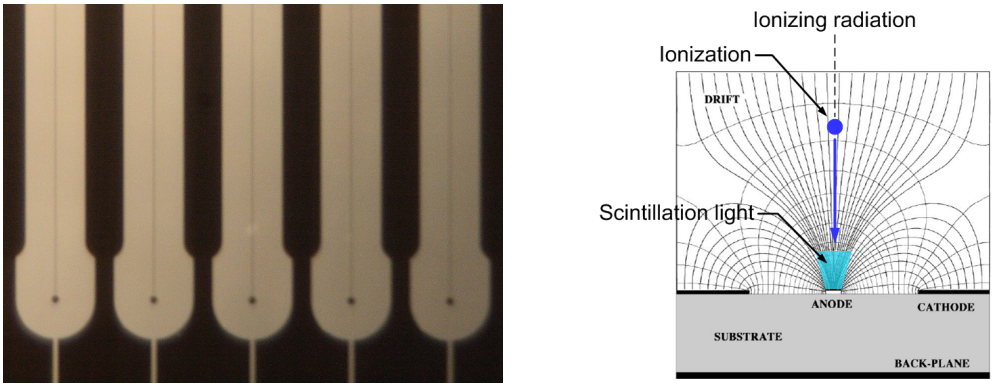

FIGURE 1.8: Left: Close up view of a microstrip. The $10\,\mu m$ anode strips alternate with $600\,\mu m$ cathodes. The pitch is $1\,mm$. Right: Equipotential field lines in a MSGC computed close to the substrate. Image retrieved from reference [30]

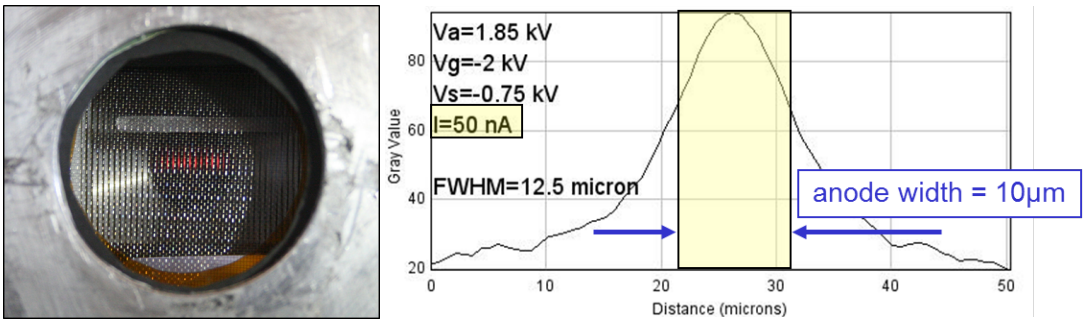

FIGURE 1.9: Left: Luminescence from a MSGC operate with CF_4 at 3 Bar pressure. Right: Luminescence profile at an anode.

of the scintillation process, the light emission is isotropic, and for typical observation distances it can be considered punctual (if the primary interaction volume is small and the electron straggling in the drift field is also small). These conditions can be met with certain gases at high pressures.

1.5 Position sensitive scintillation detectors

Some applications require the knowledge of the interaction point of the ionizing radiation inside the detector volume. For this purpose, the detector should be *position sensitive*. If large areas have to be covered and high rates are required, the *Anger type optical readout* (hereafter *Anger readout*) is the most common solution (see for example reference [1]). The Anger readout is based on the *Anger camera*, named after its inventor H.O. Anger [21] who introduced it in the late 1950s and represents a landmark in medical imaging by allowing two dimensional images of the activity of a radionuclide distribution inside the body to be obtained (see figure 1.10). The gamma photons,

emitted by the radionuclide, pass through a collimator and deposit their energy in a solid scintillator, e.g. NaI(Tl). The scintillation light is collected

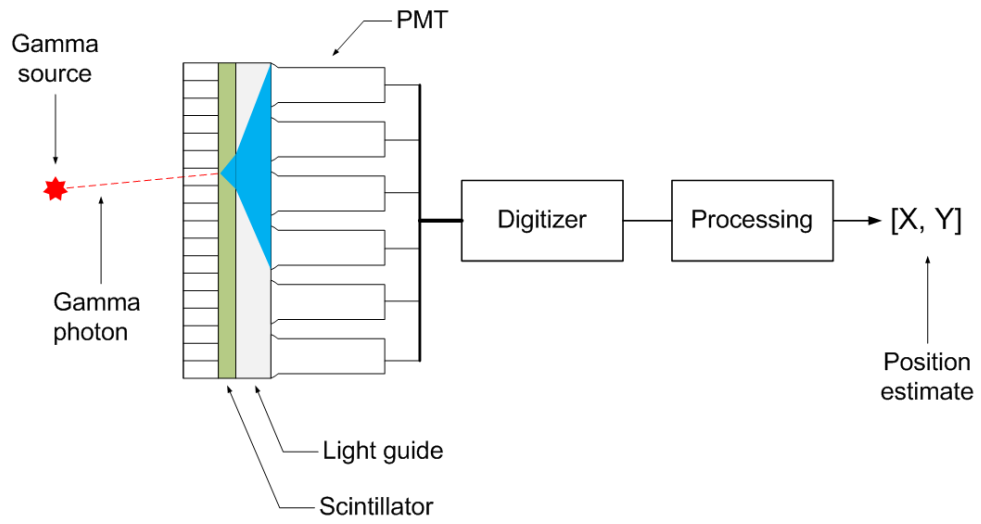

FIGURE 1.10: Schematic representation of an Anger camera.

by an array of photodetectors and the position of the gamma source is estimated from the corresponding signals of the photodetectors using a suitable algorithm[5] that computes the event location (and possibly the event energy) using the relative signal of the PMTs. This concept was adopted with gaseous scintillators to localize scintillation events inside a gas vessel either in 2D or even 3D. In the context of gaseous scintillation detectors, it is common to refer to this readout scheme as "Anger type optical readout" or an "Anger camera" particularly if it is based on a planar configuration of photodetectors as in the H. O. Anger scintillation camera.

Optical readout has several advantages over charge readout: as the electronics are decoupled from the detection media, they become insensitive to electronic noise or radio frequency pickup signals coming from the detector media and housing [5]; it is possible to cover large areas with a large filling factor leaving nearly no dead spaces; using true pixel readout it is possible to record complex events and real multi-hit capability is possible [5]. On the other hand, optical readout typically adds complexity, size and cost to the detector.

1.5.1 Photodetectors

This section provides a brief review of some photodetectors, commonly used in the context of scintillation detection. The characteristics of PMTs will be

[5]Event reconstruction algorithms are discussed in chapter 3.

briefly addressed here, as they will be discussed in detail in a dedicated chapter.

Photomultiplier tubes

The developments in light detection during the beginning of the 20th century triggered research into scintillation properties of gases and ultimately the development of gaseous detectors. During the last 80 years PMTs were used as the main low light level detector due to its outstanding characteristics. PMTs can be made with windows ranging from $1\,\mathrm{cm}$ to $50\,\mathrm{cm}$ in diameter, the typical gain is on the order of 1×10^6, and they can be made very fast, with output signal rise time in the order of $1\,\mathrm{ns}$. Depending on the incident light wavelength and photocathode material, the quantum efficiency of a PMT can be typically up to 25%. Moreover, cooled photon counting grade PMTs can have extremely low background noise and an excess noise factor around 1.2. Though impressive developments were made, they still have some drawbacks: they are sensitive to magnetic fields, they are bulky and fragile, they require high voltage, power consumption is relatively high and they are expensive.

Multianode PMTs

For some applications multianode photomultipliers tubes may represent a compact solution. Structurally, they can be viewed as a PMT with several dynode chains each converging on a single anode but with a common photocathode. They are commercially available in various sizes and number of anodes[6].

Microchannel plate PMT

A micro channel plate - photomultiplier tube (MCP-PMT) is basically a PMT tube with the dynode chain replaced by a micro-channel plate (MCP) which is a relatively thin glass (up to a few millimeters thick) with a very high density of holes ($\sim 10^6$ per cm^2), each covered with an electron emissive material. A voltage is applied across the tube length which causes electrons to cascade through the tube, reaching typical gains for a single plate of 10^4 when operated at $\sim 1\,\mathrm{kV}$ supply (MCPs can be stacked to provide gains up to 10^8 or 10^9). The MCP-PMTs feature very good time characteristics, with very small

[6] As of today, Hamamatsu sells multianode PMTs with window sizes up to $52\,\mathrm{mm} \times 52\,\mathrm{mm}$ and relatively small length $\sim$30 mm with up to 64 anodes.

transit times (in the order of a hundred picoseconds), fast signal rise time (in the order of a hundred picoseconds). The main advantage of MCP-PMT over PMTs are their compact size and timing characteristics. The main disadvantage are their relatively higher noise and cost.

Silicon PIN diode

Silicon PIN diodes are simple, reliable and cheap. The quantum efficiency can exceed 90% and the response time is in the nanosecond or even subnanosecond range. However, low light level signal detection is limited to a few hundred photons even if a slow low-noise amplifier is used [33].

Hybrid photodetector (HPD)

The hybrid photodetector (HPD) is a vacuum tube with a photocathode that detects light as it happens in a PMT. However, whereas in a PMT the electron multiplication is made in a dynode chain, in a HPD this task is made by silicon layers. The voltage across the semiconductor junction is very high, typically between 10 to $15\,\mathrm{kV}$. The gain of a HPD is typically $\sim 10^5$ and they have excellent photoelectron discrimination which results from a very low excess noise factor (~ 1). The time characteristics are very good, with output signal rise time $\sim 400\,\mathrm{ps}$ and very low or none after pulses. Like PMTs, they can be built in various sizes ranging in diameter from a few millimeters to as large as $30\,\mathrm{cm}$ [34]. They are immune to magnetic fields.

Avalanche photodiode (APD)

An avalanche photodiode (APD) combines the advantages of a PIN photodiode i.e. low cost, small, high quantum efficiency and insensitivity to magnetic fields, with those of a photomultiplier i.e. high gain and fast time response. In an APD, gain is obtained using an a high reverse bias voltage across the p-n junction (typically 100-$200\,\mathrm{V}$ in silicon), where electrons generated by photons are multiplied. The gain of an APD can be around 1000. The excess noise factor can be larger than 2 and therefore they have limited photon counting capability. APDs have to be operated at moderate internal gain and require low noise amplifiers because of the strong sensitivity to voltage stability and temperature.

Silicon photomultiplier (SiPM)

A silicon photomultiplier (SiPM) is the common name by which an array of avalanche photodiodes operating in geiger-mode have become known[7]. The first devices were built in the late 1990s [35] and since then have become increasingly improved and it is foreseen that in the near future they may replace PMTs in many applications. A typical SiPM is made of an array of microcells with dimensions ranging from $\sim 10\,\mu\mathrm{m} \times 10\,\mu\mathrm{m}$ to $\sim 100\,\mu\mathrm{m} \times 100\,\mu\mathrm{m}$. As of today, the options include single square chips with area size from $\sim 1.3\,\mathrm{mm} \times 1.3\,\mathrm{mm}$ to $\sim 6\,\mathrm{mm} \times 6\,\mathrm{mm}$ and arrays of up to 8 by 8 chips with a total area as large as $\sim 57.4\,\mathrm{mm} \times 54.4\,\mathrm{mm}$ [8]. Each microcell is an independent APD operating in Geiger-mode, thus working as a binary device, i.e. the signal from each cell is identical either activated by one photon or by many. The signals from the individual cells add up in a common load resistor and the output signal of a SiPM is the sum of the signals of the individual cells that fired at the same time. The gain of each cell is generally between 10^5 to 10^7, and consequently it may not require further amplification or at most a simple amplification stage. The number of cells limits the linearity range; however, as it can be in the order of 10^4, these devices may be linear over a broad range of light intensities. Typically, the spectral response ranges from $\sim 270\,\mathrm{nm}$ to $\sim 900\,\mathrm{nm}$, peaking at around $450\,\mathrm{nm}$. Inside the active area of a single microcell, the photon detection efficiency is similar to that of an APD. However, the effective photon detection efficiency of the device is limited by the fill factor of the micro cells. The sensitivity at the peak sensitivity wavelength can be as high as 50% for SiPMs with high fill factor ($\sim 80\%$); however, for small cell sizes the fill factor can be as low as $\sim 50\%$ and the effective sensitivity will be reduced by half (for some applications small cell size may represent the best solution as it improves the time characteristics of the device). Similarly to APDs, SiPMs have very good time characteristics with resolutions in the order of 100 ps FWHM for single photons and the dead time for a single cell can be short as $6\,\mathrm{ns}$ for $\sim 10\,\mu\mathrm{m} \times 10\,\mu\mathrm{m}$ microcells. The dark count rate of SiPM is high, ranging from 100 kcps (kilo counts per second) for small devices ($1.3\,\mathrm{mm} \times 1.3\,\mathrm{mm}$) to 2000 kcps for larger devices ($6\,\mathrm{mm} \times 6\,\mathrm{mm}$). However, the dark count rate drops dramatically for signal equivalent at ~5 photoelectrons and is therefore of little concern for medium

[7] The name is inherently wrong as it is in fact a photoelectron multiplier. Hamamatsu, for example, markets this device under the name *multi-pixel photon counter (MPPC)*; however, many other names have been proposed. For reasons of simplicity it will be referred to here as *silicon photomultiplier which has become part of the jargon of the scientific community*

[8] Presently marketed by the Irish company Sensl - see `http://www.sensl.com/`

light level applications. For low light level applications, high dark count rate is of major concern and may have to be reduced by cooling the SiPM. Due to the rather high dark count rate, SiPMs are not suited for single photon event detection.

The problem of cross talk in SiPMs appears due to photons generated inside the microcells during the avalanche process. These photons can travel to neighbouring cells and trigger an avalanche there. This process contributes to the increase in the excess noise factor which, although relatively low it can be between 1.1 to 1.2. The cross talk probability has been successfully reduced, including physical barriers between pixels. The variation of the gain with temperature is significant in SiPMs, with temperature coefficients as high as $\sim 2\,\%$ per $^{\circ}\mathrm{C}$ and it may require an output temperature feedback for some operational conditions. SiPMs are immune to magnetic fields and they can not be damaged by exposure to a strong source of light. As SiPMs are based on CMOS like technology it is expected that the price will keep reducing in the near future.

Photodetector matrices

Photodetector matrices used in position sensitive scintillation detectors consist of an array of photodetectors, each having either a single pixel (like a PMT) or many pixels (like a SiPM matrix or a multi-anode PMT). As the performance of the detector improves with the amount of collected light, the spatial distribution of the individual photodetectors in a matrix is typically the one that minimizes the non-sensitive area between them (dead space). A common configuration with round and hexagonal PMTs is a hexagonal packing, whereas devices with square windows such as multi-anode PMTs or SiPMTs are usually placed in a square packing. However, in all these cases, the fill factor of the photodetector matrix, i.e. the percentage of the photodetector matrix surface area that is sensitive to light, is under 100%, since the sensitive area of each individual photodetector is typically smaller than the window of the photodetector. Sometimes the fill factor can be further increased by adding optical elements placed between the photodetectors in order to redirect the light that otherwise would fall within the dead space (see for example [36]).

1.6 Some recent position sensitive scintillation detectors

1.6.1 The 2D gas scintillation detector for thermal neutrons from the FP7 NMI3 JRA programme

This 2D position sensitive gas scintillation detector for thermal neutrons was developed under the European FP7 NMI3 JRA programme (Project 226507)[1], a project with which I was personally involved. The aim was to build a detector capable of sub-millimetric 2D position resolution, high rate capability (>1 MHz count rate), high efficiency (> 50% for 1 Å neutrons) and an active area of $200\,\mathrm{mm} \times 200\,\mathrm{mm}$. A detector with these characteristics is of interest for reflectometry and micro-focusing small angle neutron scattering instruments at the neutron scattering facilities. The detector consisted on a gas scintillation proportional counter with an Anger type optical readout filled with a gas mixture of $^3\mathrm{He}$ (stopping gas) and $\mathrm{CF_4}$ (scintillation gas). The operation principle of the detector was as follows: neutrons entered the gas volume through an aluminum entrance window, a material with low neutron absorption cross section, and may interact with the $^3\mathrm{He}$ resulting in proton-triton pairs according to equation

$$n +^3 He \rightarrow p +^3 H + 0.77\,\mathrm{MeV} \tag{1.14}$$

Both the proton and triton deposit their energy in the $\mathrm{CF_4}$ which results in ionization electrons and scintillation light (primary). The electrons drift toward a microstrip (MS) due to the influence of a drift field. At the MS, the electrons are further accelerated towards the anodes by the strong field and where emission of secondary scintillation light occurs. A planar array of PMTs, placed in optical contact with the scintillation light through a transparent window, collects the secondary scintillation light and a suitable position reconstruction algorithm provides an estimate of the interaction position in the plane of the MS. The last prototype tested achieved sub-millimetric resolution with $8\,\mathrm{bar}$ ($1\,\mathrm{bar}$ $^3\mathrm{He}$ + $7\,\mathrm{bar}$ $\mathrm{CF_4}$) and was tested without any performance degradation up to $300\,\mathrm{kHz}$ (higher rates were not tested).

1.6.2 Large underground xenon experiment

The Lux-Zeplin (LZ) collaboration (the collaboration homepage can be found at: `http://luxdarkmatter.org/`) was born from the merging of two

previous collaborations namely the LUX (Large Underground Xenon) and Zepelin (ZonEd Proportional scintillation in LIquid Noble gases). Like its predecessors, it aims to directly detect dark matter particle interactions with ordinary matter on Earth. The detector is an hybrid gas-liquid scintillation detector operating as a time projection chamber (TPC). The structure is based on a cylindrical vessel filled with seven tonnes of liquid xenon with PMT arrays at the extremities (247 PMTs at the top and 241 at the bottom). To minimize the signal contamination from natural radiation, it will be built at a depth of about $1.5\,\mathrm{km}$. It is expected that when a weak interacting massive particle (WIMP) interact with the liquid xenon, it will result in the generation of scintillation light (primary) and the production of electrons. The electrons drift in the liquid xenon under the influence of an electric field towards the liquid surface. A stronger electric field in the gas phase will further accelerate them, resulting in the production of a relatively stronger secondary scintillation signal. A single particle interaction in the liquid xenon therefore be identified by the corresponding primary and secondary scintillation signals. In order to increase the amount of light collected per event, the internal surface of the detector is covered with PTFE, which has remarkable properties as a reflective material in the vacuum ultraviolet, allowing to an estimation of the depth of interaction, XY plane position and energy of the event. Moreover, to further reduce the background radiation, the detector is surrounded by another detector filled with gadolinium-loaded liquid scintillator and a layer of ultra pure water, to identify and reduce false signals. The underground experiments are expected to begin in 2020 [37].

1.6.3 NEXT Experiment

The *Neutrino Experiment with a Xenon TPC* (NEXT) (the collaboration homepage can be found at: `http://next.ific.uv.es/next/`) is an experiment to search for double beta decay processes ($\beta\beta0\nu$) in gaseous xenon enriched with $^{136}\mathrm{Xe}$ [38]. The fundamental interaction that describes the neutrinoless beta decay ($\beta\beta0\nu$) is as follows

$$A_Z^X \rightarrow A_{Z+2}^X + 2e^- \tag{1.15}$$

However, this reaction is much less probable than the already rare double beta decay ($\beta\beta2\nu$)

$$A_Z^X \rightarrow A_{Z+2}^X + 2e^- + 2\bar{\nu_e} \tag{1.16}$$

The only way to discriminate these $\beta\beta2\nu$-decay from $\beta\beta0\nu$-decay is through the energy of the electrons, making experimental energy resolution particularly important. The detector consists of a cylindrical gas scintillation proportional counter filled with high pressure xenon ($\sim$ 15 bar) operating as a TPC. The scintillation photons are collected by two photodetector planes, one consisting of an array of photomultipliers (to measure the event energy) and at the other end a tracking plane consisting of an array of SiPMTs. The time projection chamber is triggered by the primary scintillation light seen by both photodetector arrays and, the tracking of the event is made using the information from the light collected by the SiPMTs. The third stage of the project, which is known as NEXT-100, consisting of a detector with $100\,\mathrm{kg}$ of enriched xenon is planned to start operation in 2018 [3].

1.6.4 SNO and SNO+

The neutrino detector at the Sudbury Neutrino Observatory (SNO) (the homepage of the experiment can be found at: `http://snoplus.phy.queensu.ca/Home.html`) is installed $\sim$2 km deep in Sudbury Canada. This detector first operated as a water Cerenkov detector, consisting of a $12\,\mathrm{m}$ diameter acrylic vessel with about 1000 tonnes of heavy water. The Cerenkov light was detected by an array of 9600 PMTs mounted on a geodesic structure surrounding the heavy water vessel. Nowadays the detector is being converted to a scintillation detector by replacing the heavy water with a linear alkylbenzene [9] (LAB) which will act both as a target and scintillation material. To investigate the neutrinoless beta decay, several tons of Tellurium-130 (which has the highest abundance of any double beta decay isotopes) will be added to the scintillator medium. The operation of this detector loaded with Tellurium is expected to begin in 2017 [39].

[9] The linear alkylbenzene is a family of organic compounds commonly used to produce detergents. It has good optical transparency, high light yield ($\sim$13000 ph/MeV), peak emission at $425\,\mathrm{nm}$, fast decay time ($\sim$3.5 ns), a low amount of radioactive impurities, low toxicity, high flash point ($> 100\,^{\circ}\mathrm{C}$), is compatible with plastics and is cheap.

Chapter 2

Photomultiplier tubes

Photomultiplier tubes (PMTs) were the light detectors chosen for the position sensitive thermal neutron detector developed under the European FP7 NMI3 JRA programme (Project 226507) [1]. One of my contributions to this project was the characterization of PMTs and consequently during this time I accumulated a great deal of experience with these devices. Moreover, it was also during this project that the main guidelines of this thesis were established and therefore PMTs become the natural choice for this work. Nevertheless, it is worth noting that the fundamental concepts of this thesis are, in general, independent of the type of photodetector.

The first mass produced photomultiplier tube (PMT), model 931, was design by RCA[1] in the late 1930s and was until very recently commercially available from Burle[2] with its design practically unchanged. Today PMTs are probably the most widespread vacuum electronic devices still being used in industry and experiments in practically every scientific field. Some notorious examples of PMT applications are, for example the Super-Kamiokande neutrino observatory [40], the fine guidance sensor installed in the Hubble telescope [41], the medical gamma camera [21] and oil well logging tools [42]. Physics experiments, particularly high energy physics, are possibly the most active users of PMTs and consequently in recent decades, the PMT tube development was tailored to meet the requirements of these experiments [40]. Although for today's standards, PMTs are somewhat bulky and fragile, the following combination of characteristics make them truly remarkable devices: good quantum efficiency, high gain, low noise, large sensitive area, fast response and photon counting operation.

[1]The Radio Corporation of America (RCA) was an American electronics company in existence from 1919 to 1986.

[2]Burle Industries Inc. was an American company that carried the RCA PMT business after 1986. In 2005 Burle was acquired by Photonis which in turn ceased the production of PMTs in 2009.

2.1 Structure and operation

The basic structural elements and operation of a PMT are depicted in figure 2.1 and are as follows:

- Window: Typically materials are borosilicate glass, ultraviolet glass, quartz, magnesium fluoride and sapphire. The choice between these materials depends mostly on the required optical transmission and the amount of naturally occurring radioactive contaminants.
- Photocathode: A thin film deposited on the PMT window, where electrons (photoelectrons) are emitted by photoelectric effect. There are several different photocathode compounds matching different wavelength ranges and sensitivities.
- Electron multiplier: A chain of dynodes, where electrons undergo multiplication by secondary emission.
- Anode: Where the charge is collected forming the PMT output signal.
- Voltage divider: An electric circuit that establishes the electric field from the photocathode, through the dynodes down to the anode. There are many voltage divider types, designed to enhance different operational characteristics of a PMT.

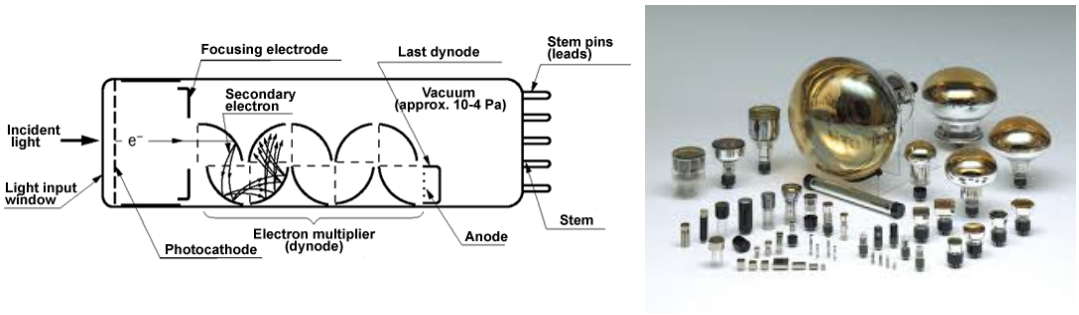

FIGURE 2.1: Left: Schematic drawing of a photomultiplier tube. Right: Different available PMT types and sizes. Images retrieved from reference [43]).

When a photon hits a PMT window it can be either reflected, absorbed or refracted towards the photocathode, depending on the optical properties of the window, the photon wavelength and angle of incidence. If the photon reaches the photocathode it may trigger the emission of an photoelectron[3]

[3]Photoelectron is the name given to an electron emitted as a result off the photoelectric effect.

by photoelectric effect. A focusing electric field accelerates the photoelectron towards the first dynode of the multiplication chain and several secondary electrons are emitted (the number of secondary electrons depends on the energy of the photoelectron and the photoemissive material on the dynode). The multiplication process is repeated to the last dynode, with current amplification up to as much as 10^8 times, and the electrons are finally collected at the anode.

2.2 Photocathode sensitivity

The photocathode sensitivity quantifies the efficiency of the photoconversion process. When the photocathode sensitivity is presented as a function of the wavelength, it is called photocathode spectral response. The photocathode response, at wavelength λ may be expressed as quantum efficiency $QE(\lambda)$, radiant sensitivity $E(\lambda)$ or luminous sensitivity $S(\lambda)$. Although they are equivalent, the choice among these three units is usually determined by the field of research. The $QE(\lambda)$ is probably the most common way to refer to the photocathode sensitivity of a PMT. It relates directly to the photoconversion process in terms of the mean number photons that will be converted into photoelectrons. It describes the efficiency of photoconversion process at wavelength λ and is expressed as a percentage (e.g. $QE(\lambda = 470\,\mathrm{nm}) = 30\%$ means that on average 30% of the $470\,\mathrm{nm}$ photons hitting the photocathode will be converted into photoelectrons). As can be seen in figure 2.2 (left), the spectral photocathode sensitivity is mostly determined by the composition of the photocathode, and should be chosen to match the requirements of the measurements to make. Nowadays the QE of a commercially available PMT can be as high as ∼43% [44]. Radiant sensitivity is used when it is required to specify the photocathode sensitivity in radiometric quantities and is defined as follows

$$E(\lambda) = \frac{I}{E_{photons}}\ (\mathrm{mA/W}) \tag{2.1}$$

where I is the current generated at the photocathode and $E_{photons}$ the energy of the photons hitting the photocathode. The photocathode radiant sensitivity of a PMT is depicted in figure 2.2. The luminous sensitivity $S(\lambda)$, is used when it is convenient to express the sensitivity in terms of photometric units which usually happens when the human eye perception is involved. The luminous sensitivity is defined as the output current obtained from the cathode

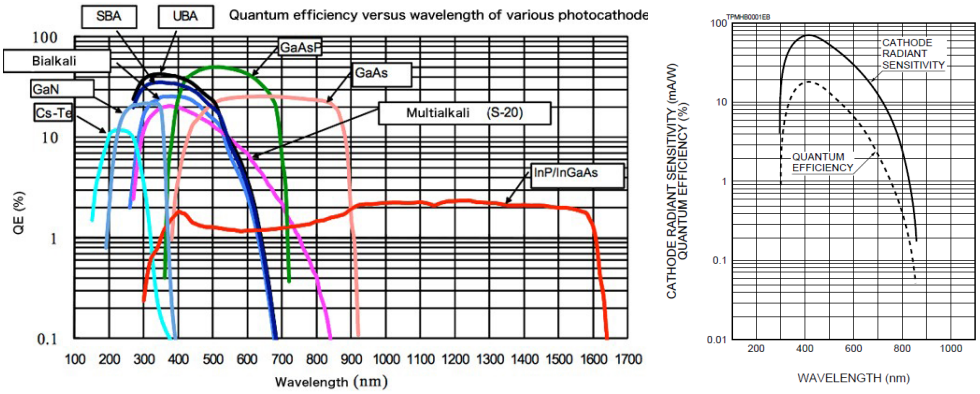

FIGURE 2.2: Left: Spectral quantum efficiency for several different types of photocathodes in the wavelength range from $100\,\mathrm{nm}$ to $1000\,\mathrm{nm}$ (image retrieved from [44]). Right: Spectral cathode radiant sensitivity and quantum efficiency of the PMT Hamamatsu R1387 (image retrieved from the datasheet provided by the manufacturer (see appendix A))

.

divided by the incident luminous flux Φ from a tungsten lamp at a distribution temperature of 2856 K. The luminous sensitivity is typically expressed in μA/lm and is given by

$$S(\lambda) = \frac{I}{\Phi_{T=2856K}}\,(\mu\mathrm{A/lm}). \tag{2.2}$$

2.3 Collection efficiency

Photoelectrons emitted from the photocathode are focused onto useful areas of the first dynode by an electron-optical input system. The ratio between the number of photoelectrons reaching the first dynode and the number leaving the photocathode is called *collection efficiency*, CE. The CE is usually expressed as a percentage, it varies somewhat with the wavelength of the incident light and is typically a value larger than $80\,\%$ [43].

2.4 Gain

The gain (or current amplification) of a PMT G is defined as the ratio between the anode current and the photocathode current. It varies with the power supply voltage as follows

$$\frac{G_{V_2}}{G_{V_1}} = (\frac{V_2}{V_1})^{\alpha N} \tag{2.3}$$

where G_{V_1} and G_{V_2} are the gains at supply voltages V_2 and V_1 respectively. α is a coefficient typically varying between 0.6 and 0.8, and N is the number of dynodes. Typical gain curves showing the dependence of the PMT gain with the power supply voltage are shown in figure 2.3 for electron multipliers with 10, 12 and 14 dynodes. As can be seen in figure 2.3, the gain increases

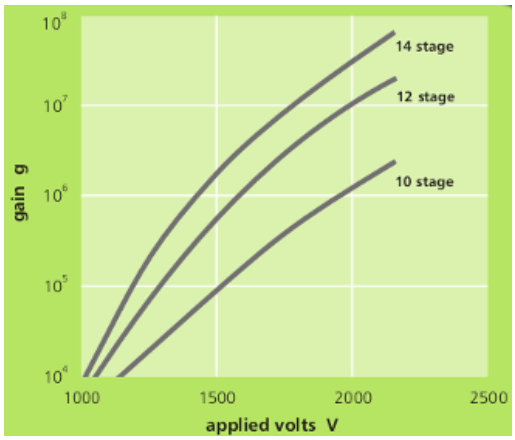

FIGURE 2.3: Typical PMT gain versus supply voltage for an electron multiplier with 10, 12 and 14 dynodes. Image retrieved from reference [45].

rapidly with the supply voltage (note the log scaling of the axis of ordinates) and gains up to 10^8 are easily attained with common PMTs. For this reason, in many applications the PMT signal can be read directly at the anode without further amplification.

2.5 Time characteristics

PMTs have excellent time characteristics. The transit time, which is defined as the time interval between the arrival of a light pulse at the photocathode and the appearance of the output signal, is in the order of tens of nanoseconds. The rise time of a common PMT can be less than $1\,\mathrm{ns}$ whereas the pulse width can be as low as $1\,\mathrm{ns}$. The time resolution of a PMT, determined by differences in the transit time, can be less than $1\,\mathrm{ns}$ (FWHM).

2.6 Linearity

PMTs have typically good linearity over a wide range of incident light levels. Nevertheless, for large amounts of incident light they increasingly deviate from an ideal linear behaviour. The main factors limiting the linearity of a PMT are: the voltage divider circuit characteristics, space charge effects

due to a large current flowing in the dynodes and, to a lesser extent, the photocathode linearity. When a PMT is operating in DC mode, linearity is limited by changes in the voltage-divider voltage due to the magnitude of the signal current. While there are differences depending on the type of PMT and divider circuit being used, the maximum practical anode current in a DC output is usually 1/20th to 1/50th of the divider current and if linearity better than $\pm 1\%$ is required the maximum output must be held to less than 1/100th [43]. Figure 2.4 (left) shows the deviation from linearity as a function of the anode current for a PMT operated in current mode. If the PMT is operated in

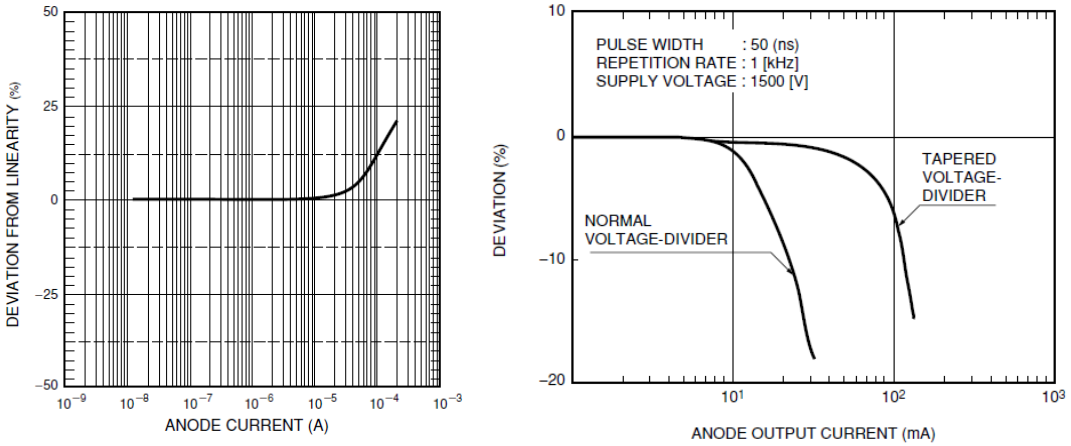

FIGURE 2.4: Left: DC mode deviation from the linearity of the anode current with increasing incident light intensity. Right: Pulse mode deviation from linearity of the output peak current for a PMT with a normal divider and a tapered voltage divider. Images retrieved from reference [43].

pulse mode, the amount of charge at the later stages will limit linearity and cause saturation. Consequently, the pulse mode linearity is highly dependent on the peak signal current. There are several techniques to modify the voltage divider in order to extend pulse mode linearity such as adding decoupling capacitors or using a tapered voltage divider [4]. As can be seen in figure 2.4 (right), with these countermeasures a high peak output current, more than thousand times as large as the divider current, can be attained. Nevertheless, the average anode current should be kept within the values presented for DC operation, in order to keep the PMT in linear operation.

[4] A tapered voltage divider allows space charge effects to be overcome by creating a larger potential difference between the last dynodes than the standard voltage distribution [43].

2.7 Spatial uniformity and angular response

The PMT response depends on the location where photons strike the photocathode as well as its angle of incidence and wavelength. The term uniformity is used to characterize the variation in the PMT response to directional light incident over the photocathode surface. In general the spatial uniformity deteriorates as the incident light shifts to longer wavelengths. Relatively large variations of the PMT response between different points on the photocathode ($> 20\%$) are common for unselected PMTs (see example figure 2.5 (left)). The dependence of the PMT response with the angle of incidence

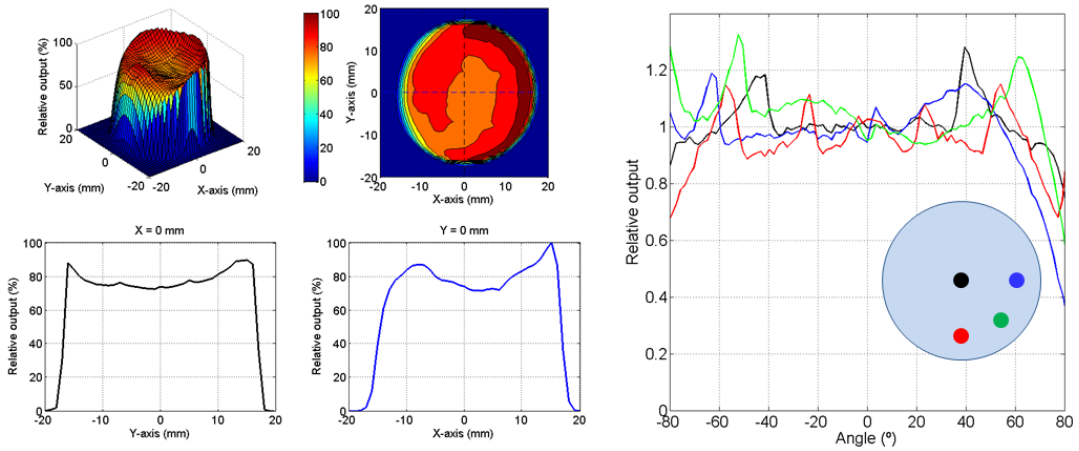

FIGURE 2.5: Example of results obtained by the author during measurements of spatial and angular uniformity made in the context of this thesis. Left: Spatial uniformity of a PMT (Hamamatsu R1387) measured at $\lambda = 470\,\mathrm{nm}$. Right: Angular response of a PMT (Hamamatsu R1387) measured at different locations on the photocathode at $\lambda = 390\,\mathrm{nm}$. The plot lines are color coded to the position on the photocathode where the measurement took place and which are schematically represented by the corresponding colored circles in the drawing depicting a PMT window.

is called angular response and it is often shown for whole photocathode illumination conditions with a collimated light source. Nevertheless a detailed characterization of the photocathode response will require the knowledge of the local angular response, i.e. the angular response over the photocathode area. Due to the optical paths of the photons and the internal reflective metallic surfaces of the PMTs the local angular dependence may exhibit large variations with the angle of incidence and vary from point to point (see example in figure 2.5 (right)).

2.8 Dark current

Even when a PMT is operated in complete darkness, it is possible to measure a small current at the anode. This output current is called *dark current* and it has several causes both structural (e.g. dynode material, glass envelope) and environmental (e.g. temperature and background radiation). Although the dark current is generally not a problem if the PMT is operating in pulse mode with high peak currents at room temperature, for applications aiming to detect minute amounts of light, the dark current should be kept as low as possible which can be attained by reducing the temperature of the PMT and choosing PMTs with low amounts of radioisotopes in the photocathode and glass envelope.

2.9 Photon counting

Photon counting is a low light level PMT operation mode, possible when the incident light is sufficiently low that there is no overlapping in the sequence of detected photons, i.e. each detected photon originates a separate time resolved signal at the anode. Under such operation conditions, PMT signals observed at an oscilloscope are similar to those depicted in figure 2.6 (left). The gain of a PMT suitable for single photon counting should be high enough in order to easily discriminate single photoelectron signals from background noise. The spectrum of the amplitudes of the signals of such a PMT, when operated under single photon counting conditions, is similar to those depicted in figure 2.6 (right) (this spectrum is usually called *single electron response* (SER)). However, PMTs are often not able to discriminate the single photolelectron peak, as in the example shown in figure 2.6 (right, PMT SN8933). Ideally, the SER would be a symmetric distribution, with a peak at the amplitude corresponding to the average single photoelectron signal. In reality, however, a SER spectrum typically has an excess of small amplitude pulses, mostly originated from thermionic emission of electrons at the dynodes that just undergo a fraction of the dynode multiplication chain. The PMT signals resulting from these electrons often overlap with the signals from single photoelectrons to form a valley as shown in figure 2.6 (right, PMT SN8918). Another structure that can be seen in figure 2.6 (right) is the large amount of small charge signal, which is due to the electronic noise and is typically referred to as the *pedestal*. Peak-to-valley ratio is often used as

an indicator of the photon counting quality of the PMT as it reflects the capability to discriminate signal from low amplitude background events (with a peak-to-valley ratio of about 2, the single photoelectron signal is already easily isolated from the pedestal (electronic noise)).

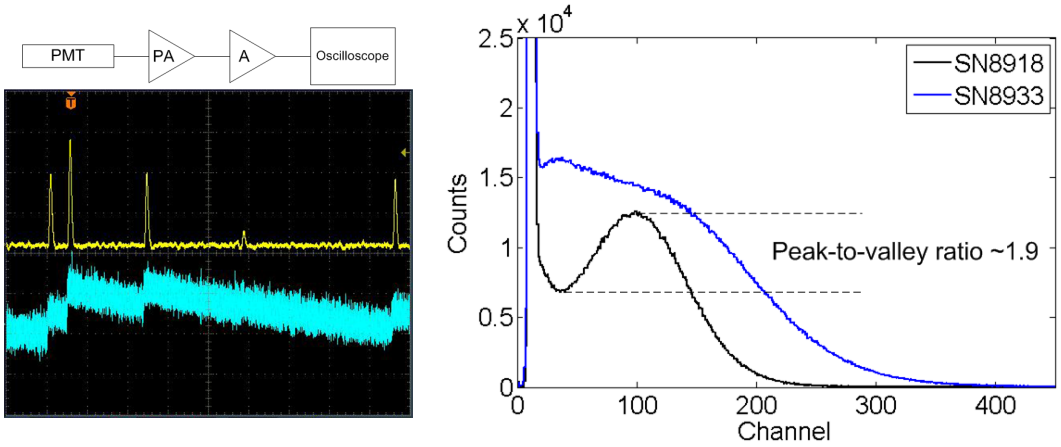

FIGURE 2.6: Left: A schematic representation of a readout electronics chain used to visualize single photon events at an oscilloscope is shown at the top. It consists of a preamplifier (PA), an amplifier (A) and an oscilloscope. The typical oscilloscope output at the preamplifier (cyan) and at the amplifier (yellow) is shown in the image below. Right: Single electron response spectrum of two PMTs of the same model (identified by the serial numbers SN8918 and SN8933). The PMT SN8918 has a well defined single photoelectron peak with a peak-to-valley ratio ~ 1.9. The PMT SN8933 doesn't discriminate the single photoelectron peak.

2.10 Noise

Ideally, if the multiplication process was noiseless, the PMT output signal distribution would just reflect the photolectron distribution characterized by the mean number of photoelectrons μ_{Phe} and the standard deviation σ_{Phe}. Assuming that the number of emitted photoelectrons and the secondary emission processes at the dynodes are well characterized by a Poisson distribution [5] it would be possible to compute the mean number of photoelectrons from the output signal distribution as follows

$$\frac{\sigma_{Phe}}{\mu_{Phe}} = \frac{\sigma_{out}}{\mu_{out}} \Rightarrow \mu_{phe} = (\frac{\mu_{out}}{\sigma_{out}})^2 \tag{2.4}$$

[5]The secondary emission process has also been modeled by a Polya distribution [46], which is capable of representing a broader range of shapes of secondary electron distributions because it contains as extreme cases both the Poisson and the exponential distribution.

where μ_{out} and σ_{out} are respectively the average and the standard deviation of the output PMT signal distribution. However, there is noise added during each step of the charge multiplication process at the dynode stages; this noise is taken into account by the excess noise factor (ENF)[6]. The excess noise factor is a measure of the deviation of the observed photodetector resolution from the expected resolution. Assuming that no other sources of noise are present we can thus write

$$\mu_{phe} = ENF \times \left(\frac{\mu_{out}}{\sigma_{out}}\right)^2 \tag{2.5}$$

The ENF values typically range from ~ 1.2 for photon counting grade photomultipliers to about 2 for unselected tubes. Additionally, there is also the noise from the readout electronics (pedestal noise) which is taken into account by the equivalent noise charge ENC[7] as follows

$$\left(\frac{\sigma_{out}}{\mu_{out}}\right)^2 = \left(\frac{\sigma_{Phe}}{\mu_{Phe}}\right)^2 ENF + \left(\frac{ENC}{\mu_{out}}\right)^2 \tag{2.6}$$

If $ENC << \mu_{out}$, which is a reasonable assumption for a typical PMT readout the equation 2.6 is reduced to equation 2.5.

2.11 Photon statistics

The number of photons hitting the photocathode of a PMT being illuminated by a light source emitting a constant number of photons can be calculated from the output signal distribution. As was seen in section 2.10, if the ENF is known (and the readout noise is small) it is possible to obtain the mean number of photoelectrons entering the multiplication chain of a PMT from its output signal distribution. The mean number of photoelectrons ejected from the photocathode $\mu_{Phe,Photocathode}$ is related to the number of photoelectrons striking the first dynode n_{Phe} by

$$\mu_{Phe,Photocathode} = \frac{n_{Phe}}{CE} \tag{2.7}$$

where CE is the electron collection efficiency. The mean number of photoelectrons $\mu_{Phe,Photocathode}$ is related to the mean number of photons striking

[6] A detailed discussion of the excess noise factor is presented in Appendix B.
[7] See Appendix C for more details.

the photocahode $n_{photons}$ by

$$n_{Photons} = \mu_{Phe,Photocathode}\frac{1}{QE} \tag{2.8}$$

where QE is the quantum efficiency of the photocathode. Using equations 2.7 and 2.8 it is now possible to write the mean number of photons striking the photocathode as a function of the output signal distribution characterized by the mean μ_{out} and standard deviation σ_{out}, i.e.

$$n_{Photons} = \left(\frac{\mu_{out}}{\sigma_{out}}\right)^2 \frac{ENF}{QE \cdot CE} \tag{2.9}$$

As for a given PMT the QE, CE and ENF are constant values at constant supply voltages and therefore equation 2.11 can be written as follows

$$n_{Photons} = \left(\frac{\mu_{out}}{\sigma_{out}}\right)^2 \cdot C \tag{2.10}$$

with

$$C = \frac{ENF}{QE \cdot CE} \tag{2.11}$$

being a constant. Equation 2.10 states that the mean number of photons hitting the photocathode of a PMT may be calculated from the signal distribution provided one knows the value of the constant C which is a characteristic of the PMT.

Chapter 3

Event reconstruction algorithms

In this chapter, a short overview of the following event reconstruction methods is presented: center of gravity, maximum likelihood and neural networks. The center of gravity method (COG) is a biased estimator i.e. it produces relatively large differences between the estimator's expected value and the true value. Nevertheless, the COG is still widely used due to its simplicity and robustness. The maximum likelihood event reconstruction method (ML) provides unbiased event reconstruction, but is computationally more complex than the COG and requires a model of the detector. The last section of this chapter is dedicated to event reconstruction using neural networks (NN) which, contrary to analytical methods such as COG and ML, may produce unbiased results in near real-time and are therefore an option to consider when such tight requirements are mandatory [47], [1]. Furthermore, there has been extensive work in this field (and related fields such as machine learning and pattern recognition) which, combined with the development of specific NN oriented hardware [48], may turn NN in an increasingly adopted solution in the context of event reconstruction.

3.1 Introduction

Event reconstruction consists of finding the coordinates and energy of an event given a set of corresponding photodetector signals. For an event at position **r** producing N_{ph} scintillation light photons, the *i-th* photodetector will detect n_i photons. The mean number of detected photons by the *i-th* photodetector μ_i can be written as

$$\mu_i = N_{ph}\eta_i(\mathbf{r}) \tag{3.1}$$

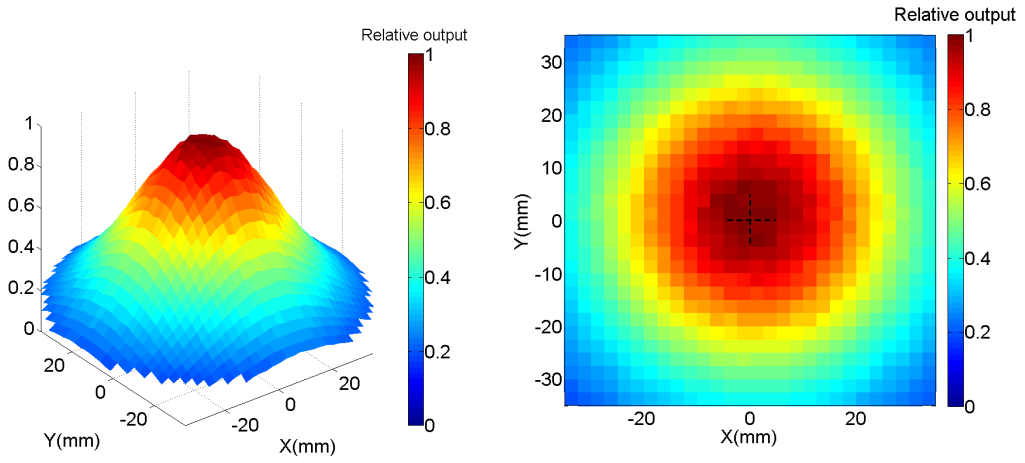

FIGURE 3.1: Relative output of a photomultiplier Hamamatsu R1387 measured over the XY plane at $Z = 30\,\mathrm{mm}$ (distance between the light source and the PMT window plane). The output is normalized to the maximum, which occurs close to the center of the PMT. Left: isometric view. Right: view normal to the XY-plane (the black cross indicates the center of the PMT).

where $\eta_i(\mathbf{r})$ is a function that describes the $i-th$ photodetector. η is typically known as the light response function of the photodetector (LRF), and characterizes the response of a given photodetector as a function of the position of an event inside the sensitive volume of the detector. An example of an experimentally measured LRF from a PMT Hamamatsu R1387 is depicted in figure 3.1. The distance between the light source and the PMT window was $30\,\mathrm{mm}$. The LRF has approximately axial symmetry, as expected, due to the geometry of the PMT. It is worth noting that the LRFs do not only depend on the characteristics of the individual photodetectors but also on the characteristics of the detector itself such as the reflectance of the materials or the geometry of the walls.

3.1.1 Center of gravity method

The center of gravity method (COG) is the most often used event reconstruction method for position sensitive detectors involving optical readout due to its computational simplicity and robustness. The position estimate of an event $(\hat{x}, \hat{y})$ is given by

$$\hat{x} = \frac{\sum_i w_i s_i X_i}{\sum_i w_i s_i}, \qquad \hat{y} = \frac{\sum_i w_i s_i Y_i}{\sum_i w_i s_i} \tag{3.2}$$

where X_i and Y_i are the coordinates of the *i-th* photodetector in a reference frame with origin at the center of the camera. s_i and w_i are respectively the weight and measured signal from the same *i-th* photodetector. The positions (X_i, Y_i) as defined in 3.2, depend not only on the position and shape of the photosensitive area but also on its photo-conversion characteristics such as uniformity and angular dependence. Additionally, due to scattered light, (X_i, Y_i) may even depend on the geometry and materials of the detector as a whole.

In general, photodetectors of the same type may have significantly different response to the same illumination conditions. The differences happen mostly due to differences in the quantum efficiency and charge multiplication from photodetector to photodetector. These differences are equalized in the COG estimation assigning a weight to each individual photodetector. The weights w_i can be experimentally estimated by measuring the output signal of each detector under the same illumination conditions s_i and comparing it to a reference value given by the signal of the photodetector with the largest signal s_{REF} i.e.

$$w_i = \frac{s_{REF}}{s_i} \tag{3.3}$$

Poorly assigned weights generally result in the occurrence of spatial distortions of the reconstructed images. One intrinsic limit of the COG method is that the reconstruction provides acceptable results only for events located inside the region delimited by the position of center of the most peripheral detectors. This is a consequence of the fact that there is no possible configuration of the photodetector signals in an event that could bring the center of gravity outside this region. Moreover, as the PMT signals do not vary linearly with the event distance, the COG can produce strongly distorted images.

Another limitation of the COG is that events close to the outer photodetectors of the camera will have the reconstructed positions shifted to the center which is commonly referred as the *border effect* and is caused by the finite size of the detector. The border effect is exemplified in figure 3.2 depicting the reconstruction of the same simulated events with a hexagonal array of 7 and 19 PMTs. Each event consisted of isotropic emission of light at the locations shown left (LIP logo) superimposed on the drawing of the two different PMT arrays.

Fluctuations of the photodetector signals are caused by several underlying processes and lead to uncertainties $\delta_{\hat{x}}$ and $\delta_{\hat{y}}$ in the reconstructed positions $\hat{x}$ and $\hat{y}$. Using straightforward computation of the error propagation on equation 3.2, and assuming that the formation of the photodetectors signal

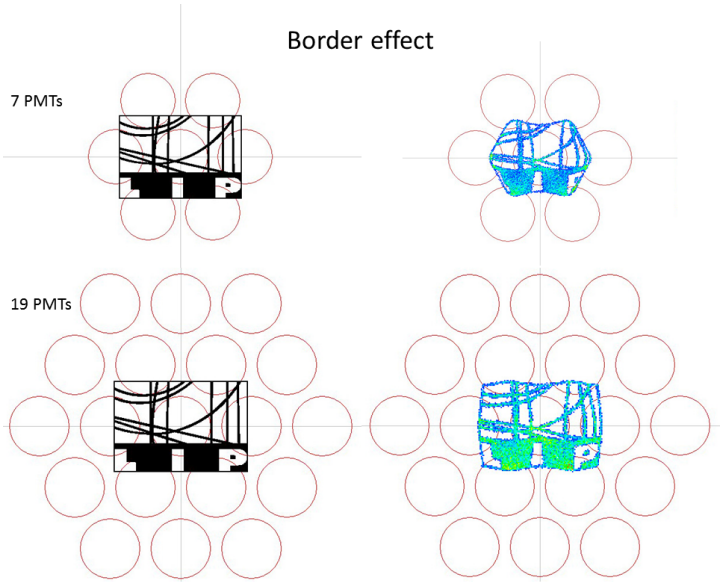

FIGURE 3.2: Border effect in COG position reconstruction. Left: event locations. Right: COG reconstruction.

is a Poisson process, it can be seen that the fluctuation of the reconstructed positions decreases as the signal distribution narrows (see appendix D). Furthermore, these fluctuations also scale with the inverse of the square root of the sum of all photodetector signals $S = \sum s_i$ i.e. the total amount of charge produced by the incoming scintillation photons. Consequently, for a given scintillation camera, it is generally expected a better position estimate, i.e. higher spatial resolution, from the COG when the number of emitted photons per event is large and narrowly distributed. This fact is somewhat generic and valid for all position reconstruction algorithms. The variation of the spatial resolution with the number of emitted photons per event is exemplified in figure 3.3. In all four cases, the events were generated at the same locations with the same detector model and only the number of emitted photons per event was changed in the range between 500 and 500×10^3.

3.1.2 Maximum likelihood method

The maximum likelihood (ML) position estimation algorithm consists of finding the set of coordinates $(\hat{x}_{event}, \hat{y}_{event})$ that maximizes the likelihood of obtaining the experimentally measured photodetector signals. The fluxogram depicted in figure 3.4 shows the basics steps of the maximum likelihood position estimation of an event occurring at some position (x, y) inside a detector. The procedure starts by calculating a likelihood function $\mathcal{L}$ using the LRFs of the individual photodetectors and the measured photodetector signals. The

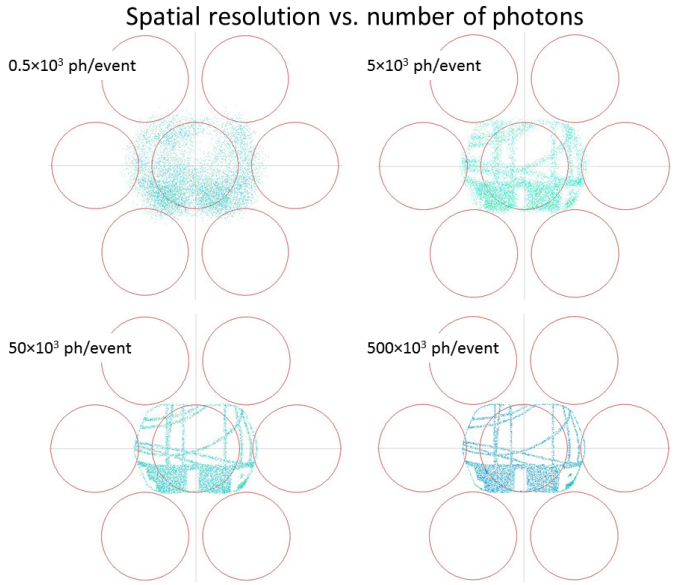

FIGURE 3.3: COG spatial resolution vs. number of emitted photons per event.

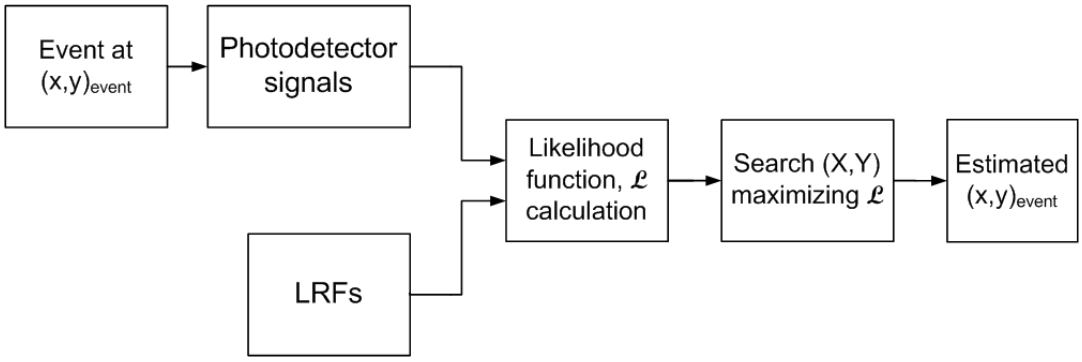

FIGURE 3.4: Fluxogram showing the data flow in an implementation of the maximum likelihood for position estimation.

ML position estimate $(\hat{x}, \hat{y})$ is found searching for the coordinates $(\hat{x}, \hat{y})$ that maximize $\mathcal{L}$. Assuming that the signals of the individual photodetectors are independent from each other, the likelihood function $\mathcal{L}$ is given by the joint probability of detecting n_i photons at the *i-th* photodetector,

$$\mathcal{L} = \prod_i P(n_i) \tag{3.4}$$

where $P(n_i)$ is the probability of n_i photons being detected at the *i-th* photodetector. As the photodetection statistics are generally well described by a Poisson distribution, the probability of n_i photons being detected at the *i-th* photodetector can be written as follows

$$P(n_i, \mu_i) = \frac{e^{-\mu_i} \cdot \mu_i^{n_i}}{n_i!} \tag{3.5}$$

where $P(n_i, \mu_i)$ is the probability of n_i photons being detected at the *i-th* photodetector when the average number of detected photons is μ_i. This allows the likelihood function $\mathcal{L}$ to be written as follows

$$\mathcal{L} = \prod_i \frac{e^{-\mu_i} \cdot \mu_i^{n_i}}{n_i!} \tag{3.6}$$

For computational simplicity, it is usual to work rather with the natural logarithm of the likelihood function $\mathcal{L}$ [1].

$$\ln(\mathcal{L}) = \sum_i \ln(P(n_i, \mu_i)) = \sum_i (n_i \ln(\mu_i) - \mu_i) - \sum_i \ln(n_i!) \tag{3.7}$$

Taking into account that $\mu_i = N\eta_i(\mathbf{r})$ is the mean number of detected photons by the *i-th* photodetector for an event occurring at **r**,

$$ln(\mathcal{L}) = \sum_i (n_i ln(N\eta_i(\mathbf{r})) - N\eta_i(\mathbf{r}) + C) \tag{3.8}$$

where C does not depend on either **r** or N. If the LRFs $\eta_i(\mathbf{r})$ are known, the best estimates $\hat{r}$ and $\hat{N}$ can be found straightforwardly by maximization of the function $ln(\mathcal{L})$. The best estimate of N at given **r**, $\hat{N}(r)$ can be found analytically by solving $d(\ln \mathcal{L})/dN = 0$ which gives

$$\hat{N}(\mathbf{r}) = \frac{\sum_i n_i}{\sum_i \eta_i(\mathbf{r})}. \tag{3.9}$$

By substituting $\hat{N}$ for N into equation 3.8 one obtains

$$ln(\mathcal{L}_m) = ln(\mathcal{L}(\mathbf{r}, \hat{N})) \tag{3.10}$$

which is a function of the position only. Then $\hat{N}$ and $\hat{r}$ are found maximising $ln(\mathcal{L}_m)$ either analytically or by numerical methods. In figure 3.5 the same data presented in the previous section (see figure 3.2) is shown reconstructed using the maximum likelihood method with LRFs given by the solid angle subtended by the photodetector sensitive window at the light emission position[2].

[1] This fact comes from the fact that the $\ln(\mathcal{L})$ is monotonous with $\mathcal{L}$. Therefore the minimum and maximums occur at the same independent variable values.

[2] In a detector where scintillation light is emitted isotropically and scattered light is suppressed the LRF of a photodetector with a uniform circular window is axially symmetric and given by the solid angle subtended by the photodetector window at the event position.

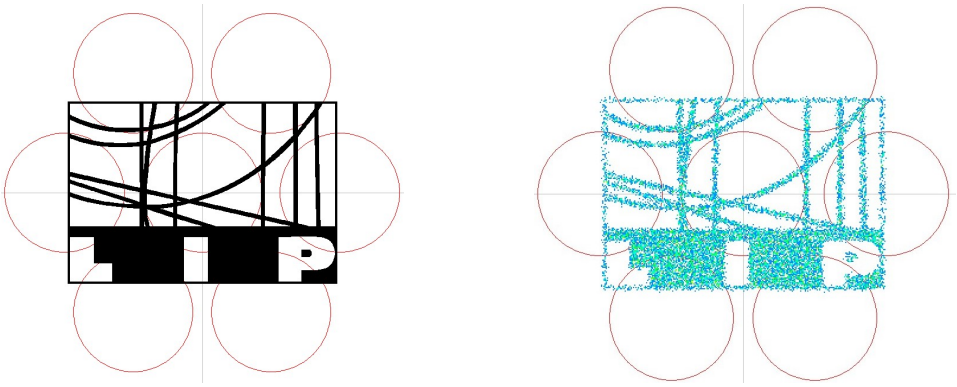

FIGURE 3.5: Maximum likelihood position reconstruction of events generated in a simulated simplistic planar detector consisting of an array of 7 photodetectors ($39\,\mathrm{mm}$ diameter) with a interaxial distance of $40\,\mathrm{mm}$. The distance between the light source and the plane containing the PMT windows is $25\,\mathrm{mm}$. The number of events simulated was 10×10^3. The number of photons generated per event was 10×10^3. Left: LIP-logo mask. Right: Reconstructed positions.

3.1.3 Artificial neural networks

An alternative to event reconstruction using analytical methods (e.g. COG or ML) is to a use an artificial neural network (NN). An artificial neural network is a computational algorithm that, by using feedback of the output, may approximate the solution of complex non-linear problems [49]. The field of artificial networks is vast and it is beyond the scope of this work to provide an exhaustive description of the methods used to choose, implement, train and optimize a NN for position reconstruction. Here, just some of the most relevant characteristics of the NN will be pointed out in the context of event reconstruction. In the previous sections we saw that the COG algorithm has a very small computation overhead but it is biased, whereas the ML is unbiased but computationally more complex and have for that reason a relatively high computation overhead. An artificial neural network may deliver both i.e. it can provide unbiased results with relatively small computational overhead. The layered arrangement is the most common configuration of artificial neural networks consisting on an input layer, one or several hidden layers and an output layer. Inside each layer there are nodes connected by weighting factors, called weights. There is no limit to the number of nodes and layers but the computational overhead generally increase with the complexity of the NN [49]. An example of an neural network configuration is depicted in figure 3.6 showing a neural network built to provide position estimation $(\hat{X}, \hat{Y})$ from a seven photodetector array. The sequence of calculations at a NN typically goes as follows: each node receives a set of inputs

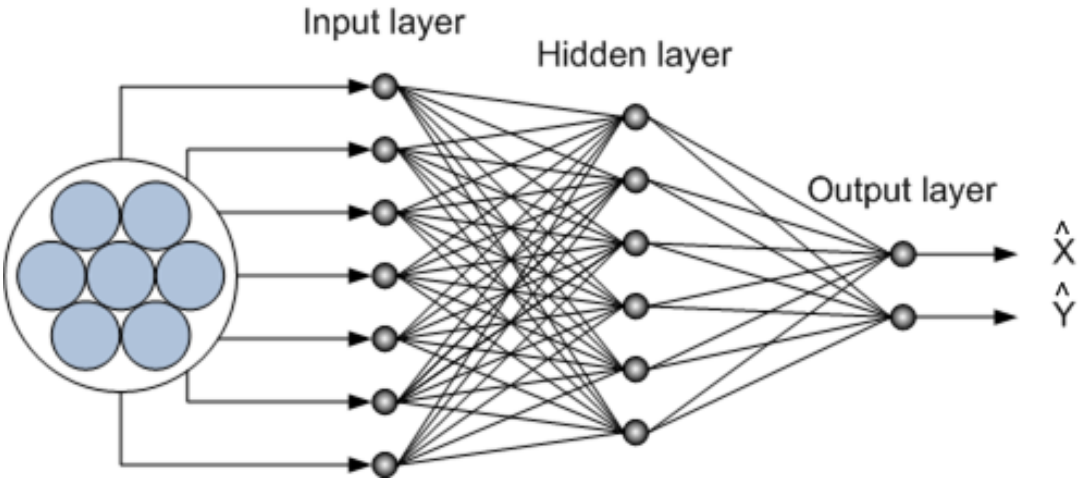

FIGURE 3.6: Schematic representation of an artificial neural network with an hidden layer. The input layer has seven nodes (photodetector signal inputs) and two nodes at the output layer (reconstructed event position (X, Y)).

either from outside or from a previous layer. Each input signal is then multiplied by a weight and the product summed. Then this summation is passed through an activation function to produced the output signal[3]. Once a network has been structured for a particular application it is ready to be trained. The objective of training a neural network is to adjust the weights so that application of a set of inputs produces the desired set of outputs (more details on the training process can be seen here [49].

The structure of the NNs is inherently parallel but most of the times they are implemented using Von Neumann (sequential) architectures. However, there are commercially available dedicated hardware design specifically for the implementation of neural networks commonly known as *hardware neural networks* (HNN) (see e.g. reference [48]). Other solutions have also been implemented with more generic hardware such as GPU-accelerated computing which takes advantage of the parallel architecture of the modern GPUs (Graphic Processing Units) [50] or using FPGAs (Field Programmable Arrays) [51].

[3]There are many activation functions that might be used as long as they are everywhere differentiable. A very common activation function is the sigmoid function which is used because is self-limiting, has a simple derivative and it may introduce a non-linear stage in calculation process.

Chapter 4

Emulation workbench: design details

Early in this project, the primary goal was to build a system capable of controlled emulation of scintillation events occurring inside the active volume of a position sensitive gaseous scintillation neutron detector filled with $^3\mathrm{He} + \mathrm{CF}_4$ gas mixture at $\sim 10\,\mathrm{bar}$ (see reference [1]). In such a detector, the detection of a neutron occurs through the interaction with a He^3 molecule, which leads to the emission of a proton and a triton with sufficient energy to ionize and excite the CF_4 gas molecules (see reaction details in table 1.3). As the gas pressure of the $^3\mathrm{He} + \mathrm{CF}_4$ mixture is relatively high ($\sim 10\,\mathrm{bar}$) the range of the proton/triton is small and consequently the primary scintillation emitted along its tracks is localized within a small volume ($\sim 1\,\mathrm{mm}$) in diameter inside the gas mixture. For these reasons, the scintillation emission occurring along the proton-triton path in the high pressure gas mixture can be considered, from the point of view of the optical system, as isotropic and punctual[1].

The ionization electrons generated by the proton/triton move towards the anodes of the microstrip under the influence of the drift electric field with relatively small spatial spreading. Close to the microstrip anodes, the strong electric field accelerates the electrons originating secondary scintillation which is also localized and can also be approximated by an isotropic point source.

[1] A source is considered to be punctual (or a point source) if the inverse square law for the irradiance holds i.e. the intensity per unit area varies in inverse proportion to the square of the distance [52]. The general rule of thumb is the "five times rule": the distance to a light source should be greater than five times the largest dimension of the source [53].

4.1 Light source

Following the arguments discussed in chapter 1 and above, the major requirements of the light source for this work were set as follows:

- Isotropy better than 10% in greater than 2π solid angle.
- Capable of operating in short pulse width mode ($\sim$10 ns).
- Precisely controllable number of emitted photons per pulse in the range from $\sim 1 \times 10^3$ to $\sim 1 \times 10^6$.
- Wavelength suitable for PMTs typically used in these detectors ($300\,\mathrm{nm}$ – $700\,\mathrm{nm}$).
- Form factor and weight allowing integration into the available 3D positioning system.
- Comparable emission volume ($\sim$1 mm).

Almost all of the aforementioned requirements are met by a light emitting diode (LED), except that LEDs do not typically emit light isotropically. The solution presented here was based on the work of Stavern [54], where he describes two different methods for the construction of a spherical isotropic fiber optic light diffuser, using a pre-fabricated sphere or using a photo-polymerization method. Spheres of white, light diffusing ceramic are commercially available in several diameters (0.2 - $100\,\mathrm{mm}$ from SWIP AG[2] and Ceratec[3]) and can be ordered with a pre-drilled blind hole of a desired diameter and depth. However they are relatively expensive and the mounting characteristics should be determined experimentally in order to achieve a good isotropy. On the other hand, the manufacture of the spheres using the photo-polymerization method is relatively inexpensive which allows iterative improvement of the quality of the light sources and discard those that do not comply with the required criteria. For these reasons, it was decided to manufacture the light source following the guidelines described by Stavern in the construction of spherical light diffusers [54]. Stavern cures spherical tips at the end of optical fibers by immersing them on a photopolymer excited by an intense blue laser. The process found here uses the same principle but the light source used to cure the diffuser was replaced by an blue

[2]Saphirwerk AG, Brügg, Switzeland: http://www.saphirwerk.com.
[3]Ceratec, Geldermalsen, The Netherlands: http://www.ceratec-ceramic-bearings.com/

LED which also will be used as a source of light in the final device. This solution allowed the specifications above to be met with a very compact and robust device. Although all this work will be based on a single wavelength ($470\,\mathrm{nm}$), it is possible to use the same mounting with different wavelengths, however in this case the diffuser tip should be cured with suitable light and then coupled to the LED with the required wavelength by a suitable optical fiber.

4.1.1 Manufacturing process

A 5 mm (T-1 3/4) round light emitting diode (LED) was chosen as it has a convenient size to be easily handled and modified. The type used to produce the light sources had a brightness of $\sim 6000\,\mathrm{mcd}$ and a sharp emission peak at 470±15 nm which allowed the photopolymer to be cured in a very short time (∼1 hour). The manufacturing sequence is schematically depicted in figure 4.1. The optical fiber (OF) used was a BFH48-200 multimode fiber

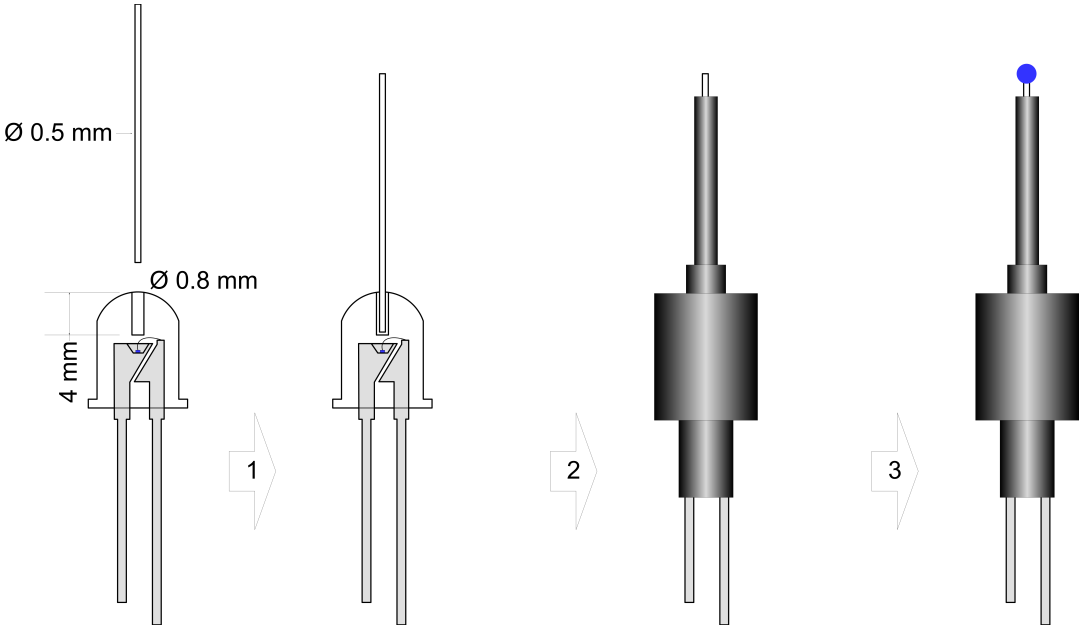

FIGURE 4.1: Light source manufacturing process sequence.

sold by Thorlabs[4]. It featured a $200\,\mu\mathrm{m}$ diameter pure silica core and an external $500\,\mu\mathrm{m}$ diameter polymer coating. The optical fibers were cut to $\sim 50\,\mathrm{mm}$ length and the extremities prepared as follows: one was sanded with fine grit sandpaper in order to smooth the OF core surface and to improve the optical coupling to the LED. At the other extremity, the coating was made rough

[4]Thorlabs Inc. is a company specialized in optical equipment with headquarters in Newton, New Jersey, USA. Url: https://www.thorlabs.com/.

by sanding with a coarse grit sandpaper in order to increase the adhesion of the photopolymer to the optical fiber. The manufacturing process started by drilling a hole with $0.8\,\mathrm{mm}$ in diameter and $4\,\mathrm{mm}$ in length in the epoxy resin encapsulant along the axis of the LED as shown in figure (see figure 4.1). The purpose of this hole was to mechanically hold the optical fiber and to increase its coupling efficiency. The OF was inserted into the hole and fixed with a transparent glue. Then the LED and the OF were wrapped in several layers of a black heatshrink tube which provided an adequate light tight, low reflectance enclosure while simultaneously adding mechanical stability. The diffuser was manufactured with a photopolymer[5] in a process similar to the one described in [54]. The optical fiber was immersed in the photopolymer and the LED operated at $20\,\mathrm{mA}$ direct current. Under these conditions, a $1\,\mathrm{mm}$ diameter spherical diffuser could be grown within 1 minute. After a rinse in methanol the diffuser was hard cured while immersed in paraffin for about 1 hour with the LED operated at the same current. Figure 4.2

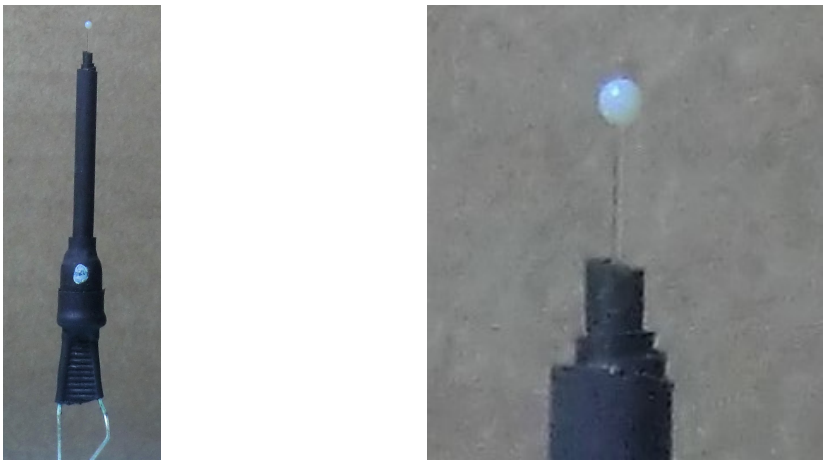

FIGURE 4.2: Light source photos (left: whole view, right: detail view).

.

shows two photos of the final look of the light source and a detailed views of the polymeric diffuser cured at the tip of the optical fiber. As there was poor control of the coupling conditions between the LED and the optical fiber during the manufacturing process, the time the OF should be immersed in the photopolymer, in order to produce a diffuser inside the required diameter, varied significantly. Therefore during the immersion, the diameter of the diffuser was systematically controlled by visual inspection and if the dimension of the diffuser was close to the requirements the process stopped. By the end of this process the light source was very robust and the diffuser was tightly

[5] A dental fissure sealant with commercial designation *Helioseal* produced by Ivoclar Vivadent Group, Schaan, Liechtenstein.

bonded to the optical fiber easily resisting the expected mechanical stress (see figure 4.2).

4.1.2 Intensity distribution and stability

During the manufacturing process, the spatial light distribution of each light source was measured with a goniophotometer in steps of $5°$ along the azimuthal and polar planes. A light source was rejected if the isotropy at any point was worse than $10\,\%$. The light intensity distribution of a light source that passed this quality test is shown in figure 4.3 (left) at a fixed azimuthal angle. In order to build a set of light sources matching these requirements, many were built and approximately just one in ten passed the required specifications.

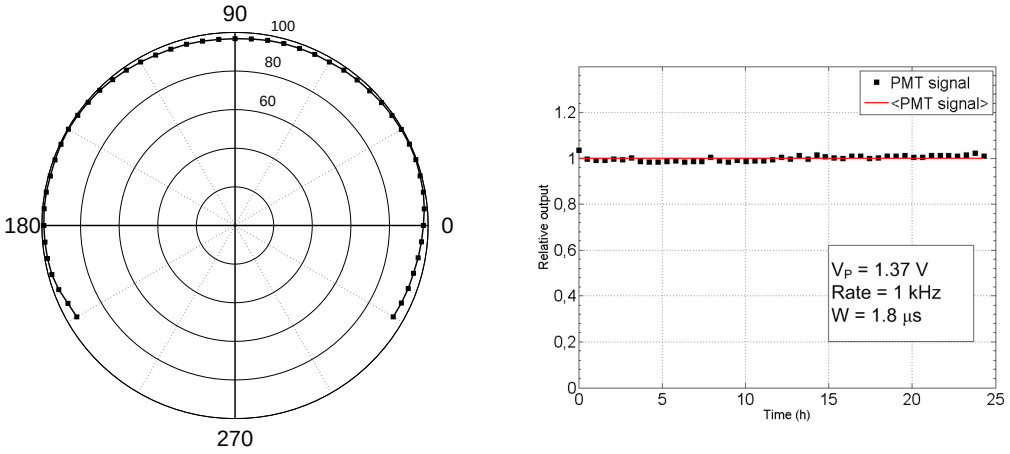

FIGURE 4.3: Left: Light source intensity distribution. Right: Stability vs. time.

Another requirement was that the light source should operate in steady conditions during the duration of experimental work. It is well known that LEDs are very stable light sources and intensity variations of a few percent over several hours operating time are easily obtained without any particular elaborated experimental arrangement. However, as the LED was wrapped in black plastic the thermodynamic heat dissipation characteristics of the device may have changed significantly and influenced the operation stability. In fact, for each set of experimental conditions a stability check should be made. It was seen that for the nominal operational conditions of the LED (short term continuous operation, operation in pulse mode with repetition rate around $1\,\mathrm{kHz}$ and pulse width between $100\,\mathrm{ns}$ and $10\,\mu\mathrm{s}$) the light source was very stable and there was no need for continuous monitoring. Instead, the light source intensity was typically checked at the beginning, middle and end of

the experimental data acquisition. The light source output[6] measured over a period of ∼25 hours is shown in figure 4.3 (right).

4.1.3 Light source positioning stage

The light source vertical positioning stage assembly is shown in figure 4.4. It comprises an holding tube fitted with a LED connector and three $2\,\mathrm{mm}$ screws that allow small position adjustments of the diffuser position to be performed in the XY plane. The holding tube slides within a cylinder to avoid movement in the XY plane[7]. The cylinder is screwed to a support structure containing the linear actuator, which is coupled to the light source holding tube. This whole assembly is mounted on an XY stage, as shown in figure 4.10 (right).

4.2 Optical readout

The optical readout assembly is depicted in figure 4.5. It consisted of an array of seven, $38\,\mathrm{mm}$ diameter photomultipliers Hamamatsu R1387 (datasheet in appendix A) held in place by a black plastic structure with two parts: a frame and a mask. The frame had seven slots, each $80\,\mathrm{mm}$ long, placed in an hexagonal configuration with an interaxial distance of $40\,\mathrm{mm}$. The PMTs were inserted through the holes down to a flange at the mask, with $34\,\mathrm{mm}$ in diameter[8] and $0.5\,\mathrm{mm}$ thick. The optical readout was coupled to the top side of the light tight box frame as described in section 4. During operation of the system the back side of the whole optical readout assembly was covered with black, light tight fabric. The Hamamatsu model R1387 is head-on type photomultiplier tube with a $\sim 38\,\mathrm{mm}$ diameter, $\sim 2.2\,\mathrm{mm}$ thick borosilicate glass window and a multialkali photocathode (see figure 4.6). According to the specifications provided by the manufacturer (see appendix A) the spectral response ranges between $300\,\mathrm{nm}$ and $800\,\mathrm{nm}$ having a maximum at $420\,\mathrm{nm}$ ($\sim 20\%$) with typical gain of $\sim 3 \times 10^5$ at $-1\,\mathrm{kV}$ operating voltage (see figure 4.7). The voltage divider circuit of the PMTs is shown in 4.8. It features a common, passive design, with three $10\,\mu\mathrm{F}$ capacitors in the three last stages

[6] In fact it was not just the light source output that was measured but also the system stability, i.e. PMT and light source.

[7] Although the linear actuator has a linear resolution of $\sim 250\,\mu\mathrm{m}$ this value only holds along the axis of the actuator. There are, however, precision solutions on the market, but the solution reported here worked very well and the maximum lateral straggling value was reduced to less than $250\,\mu\mathrm{m}$ over a $50\,\mathrm{mm}$ excursion.

[8] The PMT photocathode active area is $\sim 34\,\mathrm{mm}$ (see appendix A).

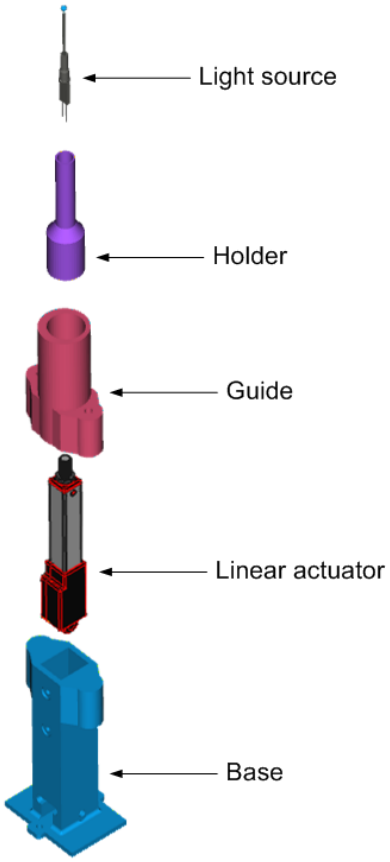

FIGURE 4.4: Exploded view of the light source moving stage assembly.

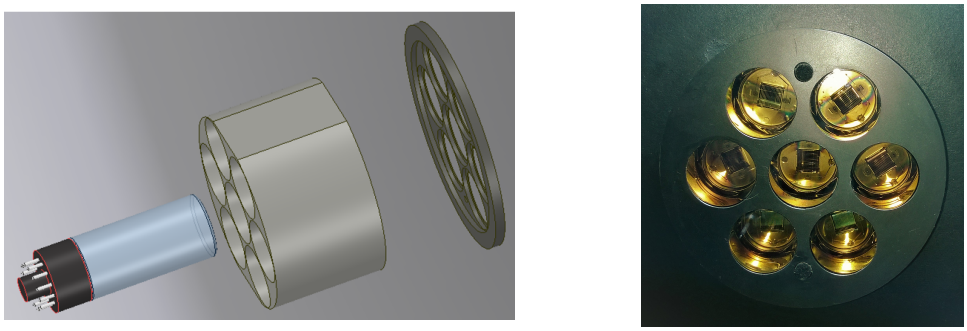

FIGURE 4.5: Left: Exploded view of the optical readout assembly. Right: PMT array.

to improve the linearity in pulsed applications. However, the voltage divider does not have other linearity countermeasures and therefore, as will be seen in section 5, it results in a somewhat limited linearity ($\sim 1\,\mathrm{mA}$ maximum peak current). The nominal supply voltage used during this work was, unless the contrary is explicitly stated, $-1\,\mathrm{kV}$ which provided anode pulses with suitable characteristics to be measured by the charge ADCs. The anode signal was measured through a $50\,\Omega$ resistor, matching the input impedance of the

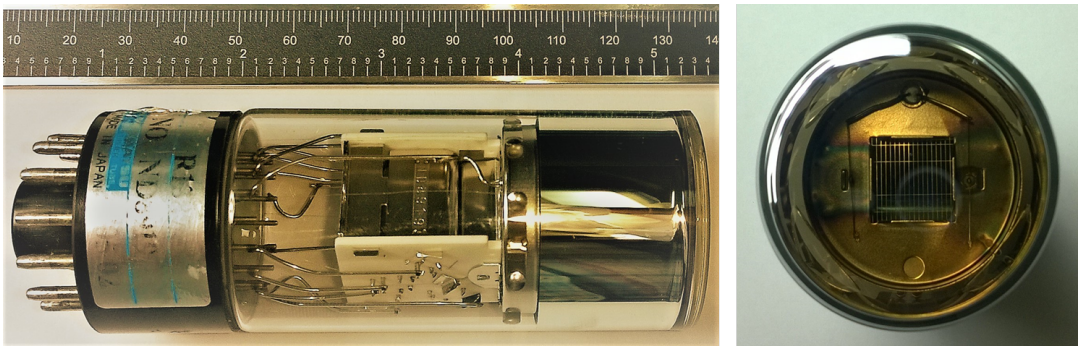

FIGURE 4.6: Left: Hamamatsu R1387 PMT (left: side view, right: top view).

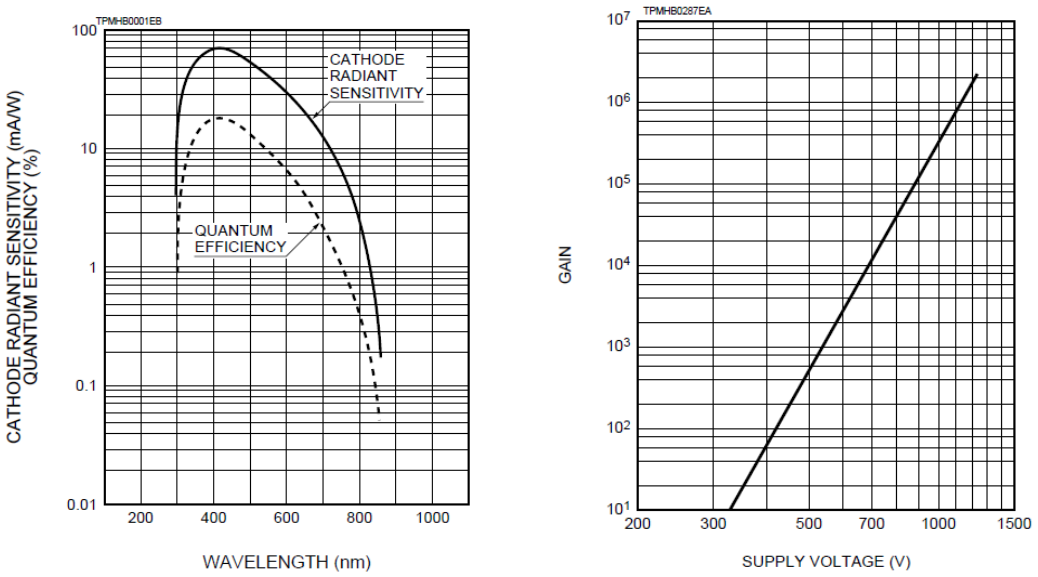

FIGURE 4.7: Cathode radiant sensitivity (left) and gain vs. voltage characteristic of a PMT Hamamatsu R1387. Source: Manufacturer datasheet (see also appendix A).

charge ADCs.

4.3 3D positioning system

The light source was mounted on a custom 3D positioning system consisting of a NEAT[9] motorized XY stage (for the horizontal movement) and a linear actuator Firgelli L12-P[10] mounted inside the light source vertical moving stage assembly (see figure 4.4). Along both X and Y directions the XY stage had $100\,\mathrm{mm}$ excursion and was driven by two $1.9°$ step motors which resulted in a linear resolution of $\sim 2.5\,\mu\mathrm{m}$. Four built-in end-of-line position sensors

[9]NEAT: New England Affiliated Technologies. This company was bought in 1999 by Kollmorgen Corporation, Radford USA.

[10]Firgelli Automations, Ferndale, USA.

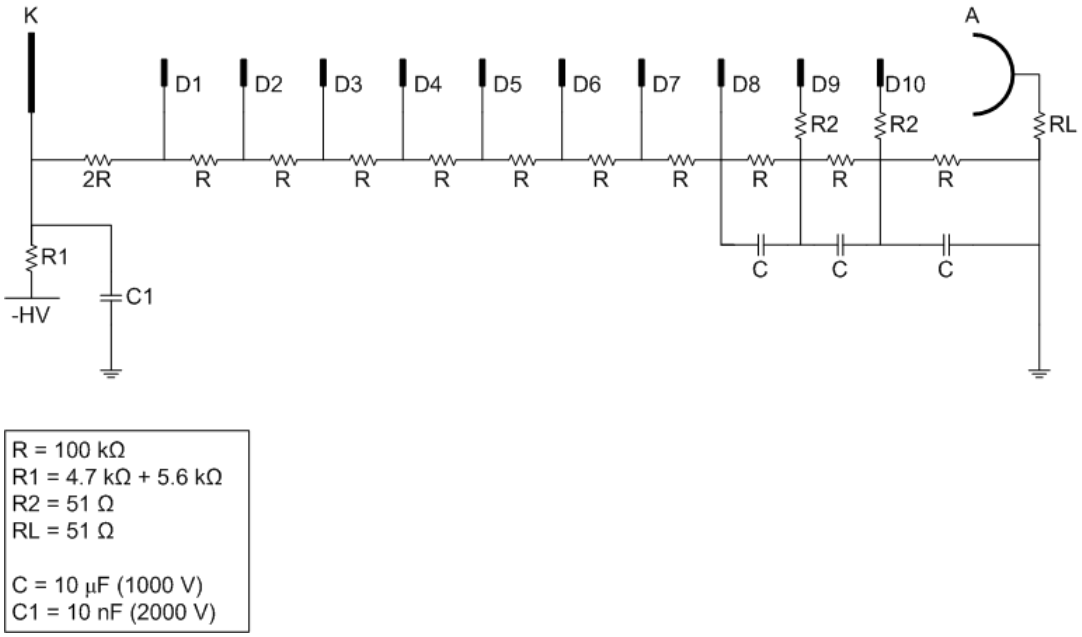

FIGURE 4.8: Voltage divider.

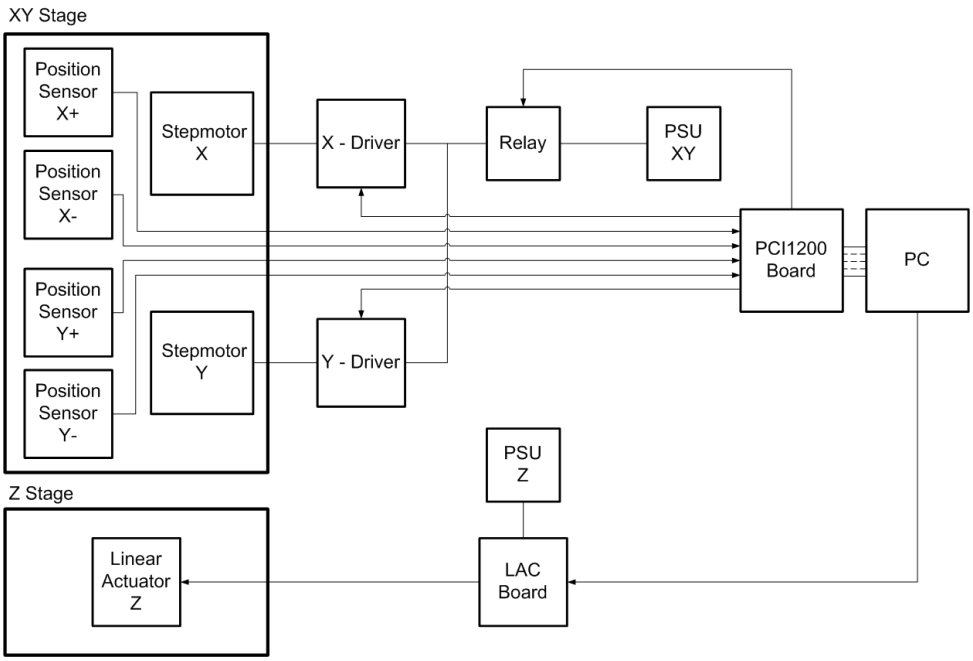

FIGURE 4.9: Scheme of the 3D positioning system control.

established the origin of coordinates of the system $(X-, Y-)$ and protected it from damage due to an outrun of the nominal excursion $(X+, Y+)$. Each stepping motor was driven by a CW5045 microstepping driver [11], both powered by a single Mean Well SP-200-27 power supply unit (PSU)[12]. The PSU

[11] CW-5045 is a generic microstepping driver sold by the UK company CNC4YOU. Url: https://cnc4you.co.uk/

[12] Mean Well Enterprises Co. LTD. (Taiwan). Url: www.meanwell.com

was connected to the drivers through a relay controlled by a digital line, which allowed the power supply to the step motors to be fully disconnected. Each driver features a enable/disable input, which allowed reduction of the current by approximately half. This feature was used every time the motors were not running, and reduced the amount of generated heat and electromagnetic noise potentially affecting the operations of the PMTs.

The linear actuator was mounted on an adjustable metallic frame at the center of the XY stage and consisted of a micro actuator Firgelli L12-P with $50\,\mathrm{mm}$ excursion and $\sim 250\,\mu\mathrm{m}$ linear resolution. This version of the actuator (P) provided an analogue position feedback signal that was used to control the position of the actuator using a LAC board (Linear Actuator Control board from Firgelli) connected via USB to the PC. The power to the actuator was supplied from a generic power supply through the LAC board. The XYZ stage was controlled by a computer through a NI-PCI 1200 board from National Instruments. The control of both XY and Z stages was integrated into the software ACEWrench which will be discussed in section 4.7.

4.4 Light tight box

The light tight chamber (see figure 4.10) was built from a cubic metallic frame with $500\,\mathrm{mm}$ side length. The walls consisted of $3\,\mathrm{mm}$ thick cardboard panels painted in black on the inner side. The PMT array was coupled to the metallic

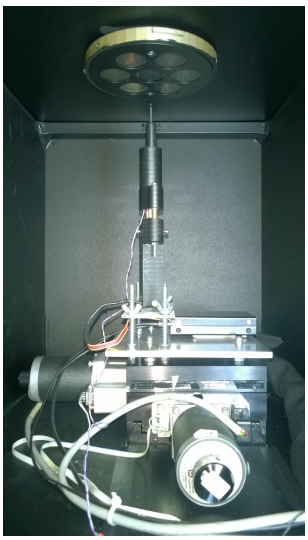

FIGURE 4.10: Optical readout, light source and 3D positioning system installed inside the light tight box.

frame at the center of the top face of the box. The inner side of the box was

accessed through a removable side-wall coupled to the frame by four wing nuts. The cables connecting the XY stage, the actuator and the light source were passed to the exterior by a set of holes at the bottom of the box fitted with tight rubber rings covered by light tight plastic.

4.5 Scattering surfaces

Figure 4.11 shows an exploded view of the structure built to study the effect of scattering in event reconstruction. It consisted of two grooved frames (in figure 4.11 they are named as the top and bottom frame) that allow a cylindrical wall made of the required material to be hold in position. The wall is held in place in each frame by three PTFE screws. The frames and wall are mounted as a unique piece that could be easily coupled (or decoupled) rotating it into a holder mounted on the mask. The holders were manufactured with several grooves, allowing the diameter of the walls to be changed from $162\,\mathrm{mm}$ to $202\,\mathrm{mm}$. The maximum wall thickness is $5\,\mathrm{mm}$. Figure 4.12 (left) shows a photo of the system fitted with a PTFE wall. An internal view of the aluminized Mylar is shown in figure 4.12 (right).

4.6 Readout electronics

The readout electronics are depicted schematically in Figure 4.13. The PMT signals, were fed directly to a 11 bit charge ADC (LeCroy 2249W) through relatively short coaxial cables ($\sim 1\,\mathrm{m}$) and integrated during an adjustable time, set by an external gate signal. If required a 12 channel amplifier (LeCroy 612A) was used to amplify the PMT signals before being fed to the ADC. A gate generator (LeCroy 222), triggered synchronously with the light source excitation pulse generated the gate signal to the ADC. The gate line delay and the gate width were adjusted in order to integrate the whole charge of the PMT signal. On some occasions an attenuator (not depicted in Figure 4.13) was used connected to the PMT with highest gain in order to extend the dynamic range of the measurements. As will be seen in chapter 5, to avoid pulse mode saturation of the PMTs, peak current should be limited. Therefore, in order to generate light pulses with a very large number of photons, it is required to extend the duration of the pulse keeping the peak amplitude inside the linearity range. Under these conditions a charge ADC is very useful as the whole PMT charge signal can be directly read from the PMTs without further intermediate signal processing. The ADC had a CAMAC form factor

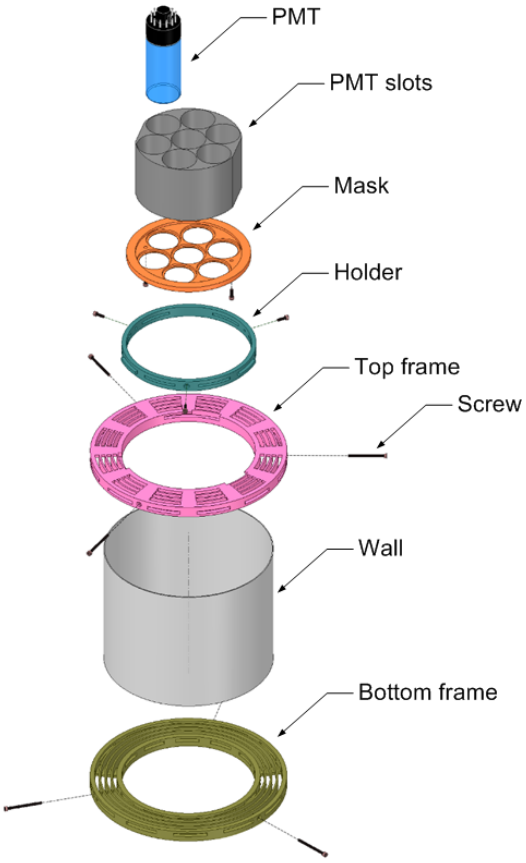

FIGURE 4.11: Exploded view of the structure built to study the effect of scattering from a wall in position reconstruction.

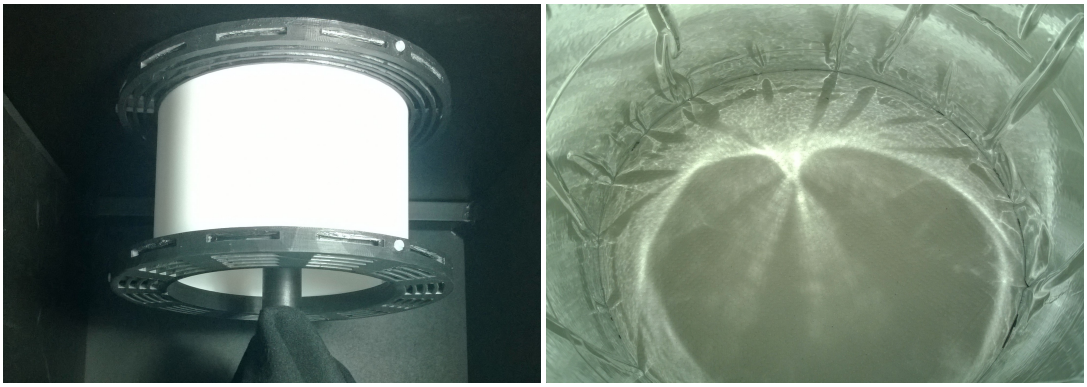

FIGURE 4.12: Left: A PTFE wall mounted on the workbench. Right: aluminized Mylar wall.

and was read through a software written in C programming language[13] by a dedicated computer.

[13]This software was an adaptation of an existing code in order to be triggered by an external digital signal through the parallel port of the master PC that controlled the CAMAC modules.

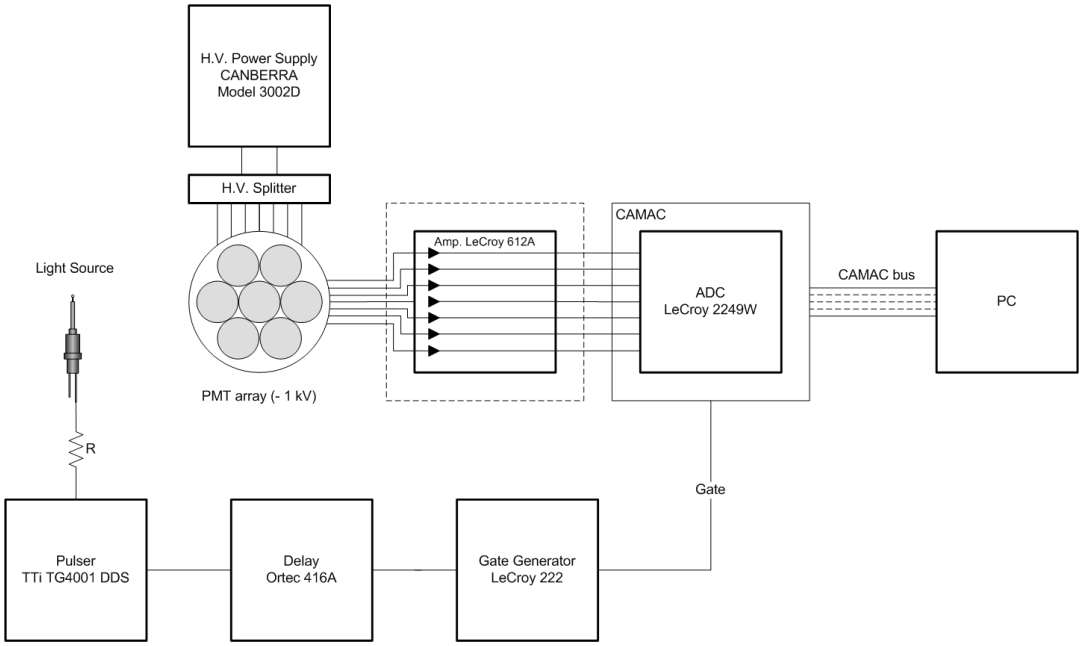

FIGURE 4.13: Diagram of the readout electronics. The amplifier LeCroy 612A was only used when it was required to increase the dynamic range of the digitalization of small signals.

4.7 Control and data acquisition

The data acquisition, light source positioning and experimental data preprocessing were integrated in a single application, developed during this work in LabVIEW programming language[14] named *ACEWrench* from **A**cquisition and **C**ontrol of an **E**mulation **W**o**R**kb**ENCH**. The graphic user interface of the latest versions of the program is shown in figure 4.14. Throughout this work, successive versions of the ACEWrech have been developed in order to fulfill the requirements of the ongoing experimental work. In its latest version, it featured the following main modules: light source position control, data acquisition, signal monitoring and pre-processing. The position control module allows the absolute position of the light source to be established either by setting a final position or moving the light source in small user defined increments until it reaches the desired position. Frequently used positions, such as the positions of the PMTs could be stored in memory for operational convenience. To easily calibrate the positioning system the main settings of the of the XY motorized stages and linear actuator are available in the main user interface of the ACEWrench, complemented with a tool that sets the origin of coordinates by continuously moving the XY

[14]LabVIEW is the acronym of Laboratory Virtual Instrument Engineering Workbench which is a system-design platform and development environment for a visual programming language from National Instruments Corporation, Austin, USA.

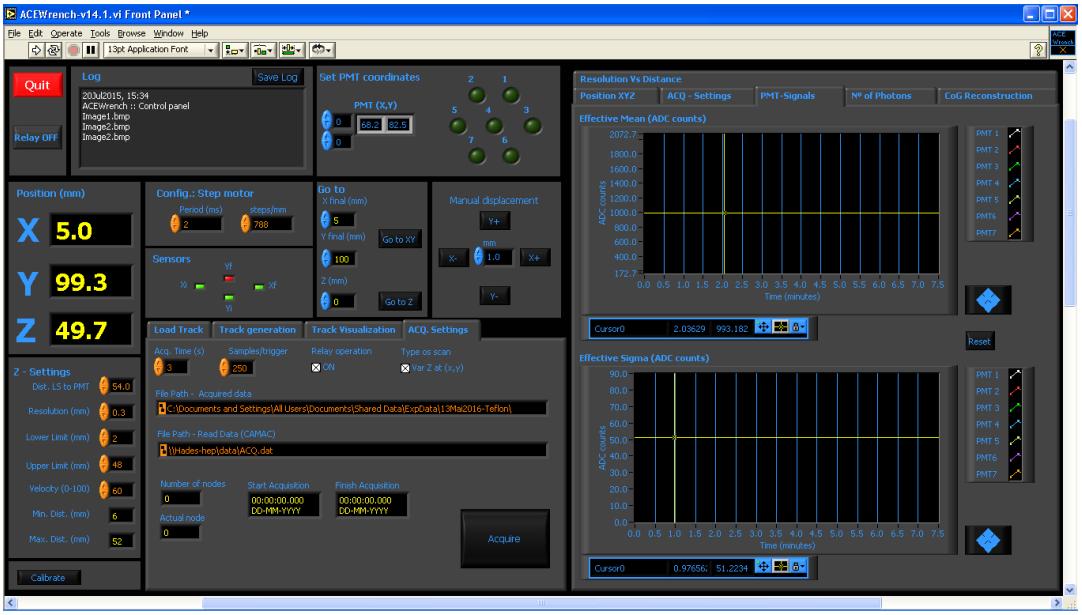

FIGURE 4.14: Graphic user interface of the control and data acquisition software ACEWrench: ACEWrench from **A**cquisition and **C**ontrol of an **E**mulation **W**o**R**k**b**ENCH.

stage until stopped by the reading of the end-of-line sensors[15]. The current position is displayed at the GUI and the position history is shown at a dedicated XY plot. The XYZ scanning module comprises a set of track generation tools that allow to build the required tracks with light source position where the PMT signals will be acquired. As an option, a file could be loaded with a custom XYZ track. The configuration of the data acquisition is done in a set of specific tabs and the acquired data is then saved in a file compatible with ANTS2 [6] with the following structure: [PMT_1 PMT_2 ... PMT_7 X Y Z]. The PMT signals are monitored at a set of specific plots in the GUI. The number of emitted photons per pulse is monitored by continuously displaying its most important statistical information. It is also possible to acquire and store pedestal values of the PMT channels in order to correct, and display, the pedestal corrected ADC counts for each PMT. In the pre-processing module, the current light source position was reconstructed using the center of gravity algorithm, allowing the consistency of the recorded experimental data to be checked on the fly.

[15]Nevertheless the accumulated error along the X and Y directions was very small; even for high density of node grids, it did not exceed $100\,\mu m$.

Chapter 5

Emulation workbench: characterization

In this chapter, the calibration procedures of the *emulation workbench* are presented, with particular focus on the critical parameters required to emulate a scintillation detector and to properly reconstruct *emulated scintillation events*. The geometry of the main components of the system, PMTs, light source, light tight box and movable scattering surfaces are characterized. The PMTs' pulse mode linearity was studied and the relative and absolute gains were experimentally determined. The detection probability of the PMTs was also estimated along with the light response functions, since both are required to build the detector model to be used with the maximum likelihood position estimation algorithm. Other characteristics of the PMTs such as spatial and angular uniformity were also investigated and are briefly discussed.

5.1 Geometry

The position of the projection of the axis of each PMT on the XY plane $(x_c, y_c)_{PMT}$ was mapped using a collimated light beam placed inside each PMT slot as depicted in figure 5.1. To produce a narrow beam of light, a red laser diode was mounted on a 39 mm diameter, 25 mm high plastic cylinder with a $0.8\,\mathrm{mm}$ hole at the center. This collimator fitted tightly into the PMTs slots and the laser beam illuminated the XY plane perpendicularly. For each PMT, the position $(x_c, y_c)_{PMT}$ was determined as follows: the PMT was removed from the slot and replaced by the collimator. Then the light source was moved towards the direction of the laser light beam until very close to the light beam. At this point, the position was varied by small increments until the laser illuminated just the center of the light source diffuser. The position $(x_c, y_c)_{PMT}$ in the *XYZ stage coordinate system* was then assigned. As the laser beam was very narrow ($800\,\mu\mathrm{m}$), and the radius of the light source

diffuser was $\sim 2\,\mathrm{mm}$, and since the intensity of the reflected light from the diffuser was very sensitive to the position of the light source, the expected uncertainty along both X and Y directions is expected to be smaller than $0.5\,\mathrm{mm}$ [1].

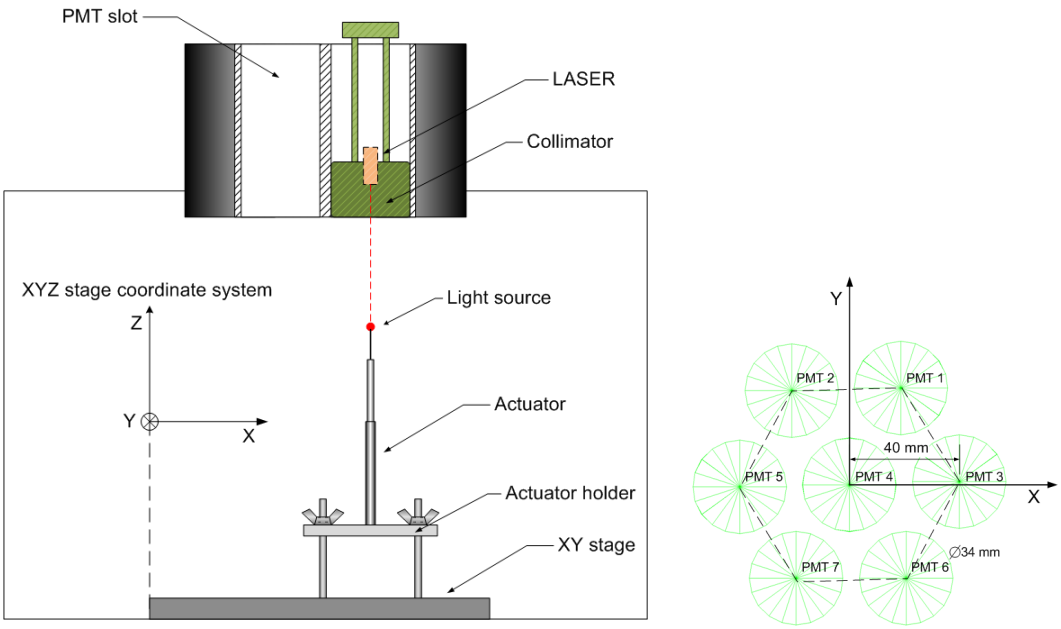

FIGURE 5.1: Left: Set-up used to determine the coordinates of the center of the PMTs. Right: *Camera coordinate system*. The directions X and Y are coincident with the directions with the same name in the *XYZ stage coordinate system*.

The plane on which the light source holder stands was tuned in order to minimize the deviation of the diffuser trajectory from the laser beam when the distance between the diffuser and the PMT windows is moved from $5\,\mathrm{mm}$ to $50\,\mathrm{mm}$. The maximum deviation in the XY plane less than $250\,\mu\mathrm{m}$ over the full diffuser excursion ($50\,\mathrm{mm}$). The *camera coordinate system* was then defined with the XY origin at the $(x_c, y_c)_{PMT4}$ and the Z origin on the plane of the PMT windows. Figure 5.1 (right) shows the positions of the PMTs in the *camera coordinate system*. As can be seen from the superimposed hexagon shown with dashed contour, the PMT array follows very nearly a hexagonal arrangement with $40\,\mathrm{mm}$ side length (the hexagon is rotated clockwise by $\sim 1.7°$ around the center of the *camera coordinate frame*.)

[1] It is envisaged that the accuracy of this operation could be increased by using the LED in the light source as a light detector. This solution would probably require the replacement of the red laser diode by a blue one, as generally LEDs are sensitive to the same wavelengths of the emission or shorter.

5.2 Light source

The intensity distribution of the light source was measured using a goniophotometer. The measurement was made in angular steps of 5° in both azimuthal and polar planes. The results are shown in figure 5.2 which depicts the normalized relative intensity distribution at fixed azimuth (see figure 5.2 (left)) and a color coded surface plot where the light source is considered to be at the origin of the system of coordinates with the distance to the plotted surface (and color coding) proportional to the recorded signal at that position (see figure 5.2 (right)). The anisotropy of the light source is better than $\sim 10\%$ over $\sim 3.5\pi$. Due to the small anisotropy and size of the light source it

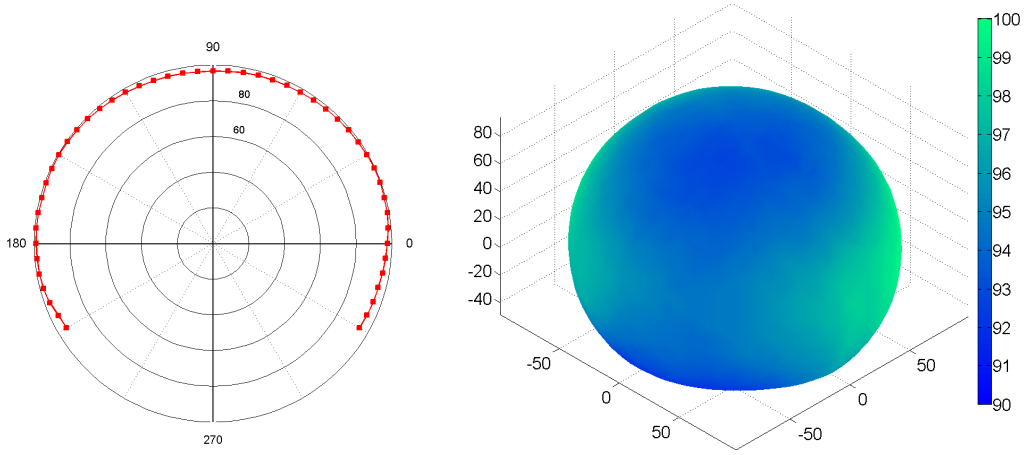

FIGURE 5.2: Normalized relative intensity distribution of the diffuser used in this study: (left: cross section, right: 3D representation in Cartesian coordinates). The light source is considered to be at the origin of the system of coordinates and the distance to the plotted surface (and color coding) is proportional to the recorded signal at that position.

is expected that the point source approximation holds for distances between the light source and the PMT window as small as $10\,\mathrm{mm}$. In order to evaluate the applicability of the point source approximation to our experimental conditions, the signal of a PMT from the experimental workbench was measured varying the distance along the axis of the PMT between the light source and photocathode (d) from $7.2\,\mathrm{mm}$ to $52.2\,\mathrm{mm}$. The results were then compared plotting the *normalized signal to solid angle ratio* defined as follows

$$Normalized\ S_{PMT}\ to\ \Omega\ ratio = \frac{S_{PMT}}{\Omega} \times \frac{1}{\left\langle \frac{S_{PMT}}{\Omega} \right\rangle} \times 100 \tag{5.1}$$

where S_{PMT} is the signal of the PMT and Ω is the solid angle subtended by the PMT photocathode at the position of the center of the light source diffuser (approximated by a $34\,\mathrm{mm}$ diameter circle). The term $\frac{1}{\left\langle \frac{S_{PMT}}{\Omega} \right\rangle}$ is the average value of S_{PMT}/Ω calculated over the whole d range. As follows from simple geometry the $Normalized\ S_{PMT}\ to\ \Omega\ ratio$ should be constant with the distance d if the light source approximation holds. The result is shown in figure 5.3 (left), revealing a good agreement with the point source approximation assumption. The light source stability[2] was checked during several measure-

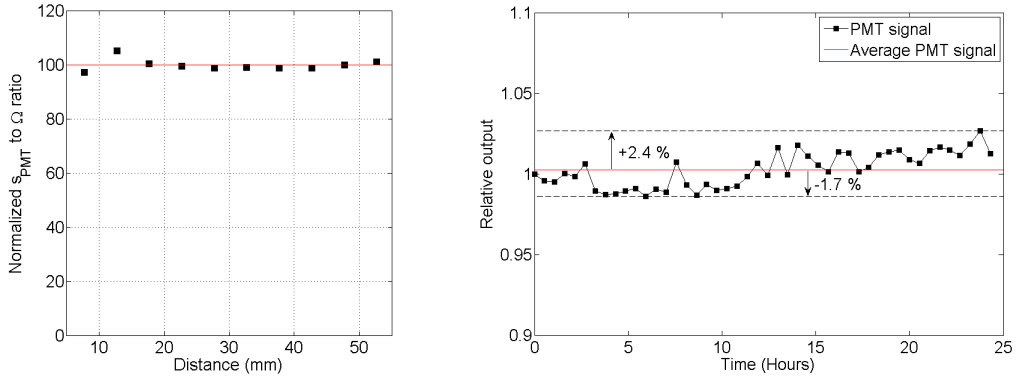

FIGURE 5.3: Left: $Normalized\ signal\ to\ solid\ angle\ ratio$ versus distance between the light source center and the photocathode. Right: PMT signal versus time. The red line represents the value of the mean PMT signal calculated over the entire acquisition time.

ments in different conditions. It was seen that within the conditions used during this work, mostly pulsed light source, low current, relatively small duty cycle $\sim 1\,\mathrm{kHz}$ and pulse widths up to $3\,\mu\mathrm{s}$ the light source was very stable even on the long term measurements. In figure 5.3 (right) the signal of the light source was measured recording a PMT signal over a period of ∼25 hours. The light source was operated at $1\,\mathrm{kHz}$ and with pulses of $2.7\,\mu\mathrm{s}$. The amplitude of the pulses was set, keeping the PMT operating under linear conditions. The measurements depicted in figure 5.3 (right) are normalized to the mean of the relative output over the whole acquisition time. The maximum deviation found during this measurement was about $4\,\%$; nevertheless, acquisitions often took less time and the maximum deviation in these cases was smaller.

[2] Accurately, the light source stability as presented here is in fact the light source and read out stability, as the PMT signal may be also subjected to gain variations.

5.3 PMT characterization

5.3.1 PMT linearity

The PMT anode linearity is defined as the direct proportionality between the number of photons hitting the photocathode and the charge collected at the anode. Uncompensated non-linear PMTs may strongly reduce the overall performance of the camera, generating spatial distortions or reducing the energy accuracy of event reconstruction. Considering the relatively large dynamic range of the detected light pulses in this work, the following linearity study was conducted in order to search for the characteristics of the PMT pulses (amplitude, duration and rate) that allow simultaneous linear operation of all PMTs thus avoiding further linearity compensations[3]. The PMT linearity is mainly limited by two factors: the voltage-divider circuit and space charge effects due to a large current flowing in the dynodes [43]. Although the PMTs are all from the same model, with the same voltage divider design, characteristics such as quantum efficiency and gain may vary significantly among them. This fact means that for the same illumination conditions, the total charge collected at the anode of each PMT may be different and therefore the PMTs may have different linearity ranges.

Pulse mode linearity

As the voltage divider circuit (see figure 4.8) has serial connected $10\,\mu\mathrm{F}$ decoupling capacitors between the three last stages, which at $-1\,\mathrm{kV}$ (nominal operation voltage of the divider) are able to store a charge $Q_0 \approx 800\,\mu\mathrm{C}$ much larger than the charge of the largest pulse charge within the ADC dynamic range $Q_{max} \approx 500\,\mu\mathrm{C}$, it is expected that at $1\,\mathrm{kHz}$ pulse repetition rate, the linearity loss will be mostly dominated by spatial charge effects [43]. As the light signal amplitude and duration can be controlled, the non-linearity due to the spatial charge effect may be avoided by limiting the peak amplitude of the PMT signal.

[3] As the pulse characteristics of the light source are controllable in amplitude, duration and rate, it is possible to set a broad range of illumination conditions without significant loss of linearity of the camera: in general, the saturation due to the spatial charge effect is avoided limiting the peak current of the charge pulses at the anode, whereas the saturation due to large current flowing through the divider may be avoided reducing the pulse rate.

Experimental set-up and methods

The pulse mode linearity was measured using the double pulse amplitude technique. At sufficiently low light levels the ratio between the PMT charge signals for the higher and lower pulse amplitudes is equal to the ratio between the number of photons emitted by the light source at those amplitudes which can formally be written as

$$\frac{S^0_{higher}}{S^0_{lower}} = \frac{N^0_{higher}}{N^0_{lower}} \tag{5.2}$$

where S^0_{higher} and N^0_{higher} are respectively the PMT charge signal and the number of emitted photons at higher pulse amplitude, and S^0_{lower} and N^0_{lower} are respectively the PMT charge signal and the number of emitted photons at lower pulse amplitude. As the light source is brought closer to the PMT, the output current increases and the PMT output begins to deviate from linearity. At this position the ratio between the output charge signal for the lower amplitude pulsed light (S^1_{lower}) and the output charge signal for the higher pulsed light (S^1_{higher}) is related to S^0_{higher} and S^0_{lower} as follows

$$\frac{S^0_{higher}}{S^0_{lower}} \neq \frac{S^1_{higher}}{S^1_{lower}} \tag{5.3}$$

Assuming that S^0_{higher} and S^0_{lower} are obtained in the linear range, the extent of deviation from linearity at the anode output is given by

$$\frac{S^1_{higher}/S^1_{lower} - S^0_{higher}/S^0_{lower}}{S^0_{higher}/S^0_{lower}} \times 100\% \tag{5.4}$$

The measurements of the pulse mode linearity of the PMTs were made in the *emulation workbench* with a dedicated experimental arrangement as shown in the block diagram depicted in figure 5.4. An arbitrary waveform generator TGA 1241 was programmed to alternately produce equally wide pulses of amplitudes $A_1 > A_2$ at fixed ratio. The measurements were made at $1\,\mathrm{kHz}$ and $500\,\mathrm{Hz}$ repetition rates (here the repetition rate is defined by two consecutive pulses e.g. at $1\,\mathrm{kHz}$ pulse rate, the pulses with amplitude $A1$ and $A2$ are pulsed at $500\,\mathrm{Hz}$ with $1\,\mathrm{ms}$ delay between them). For each individual PMT the light source was placed at $(x_c, y_c)_{PMT}$ and moved from d = $10\,\mathrm{mm}$ to d = $50\,\mathrm{mm}$ away in steps of $2.5\,\mathrm{mm}$. The acquisition was made using the ACEWrench control software by recording 1000 samples of the PMT signal at each distance d.

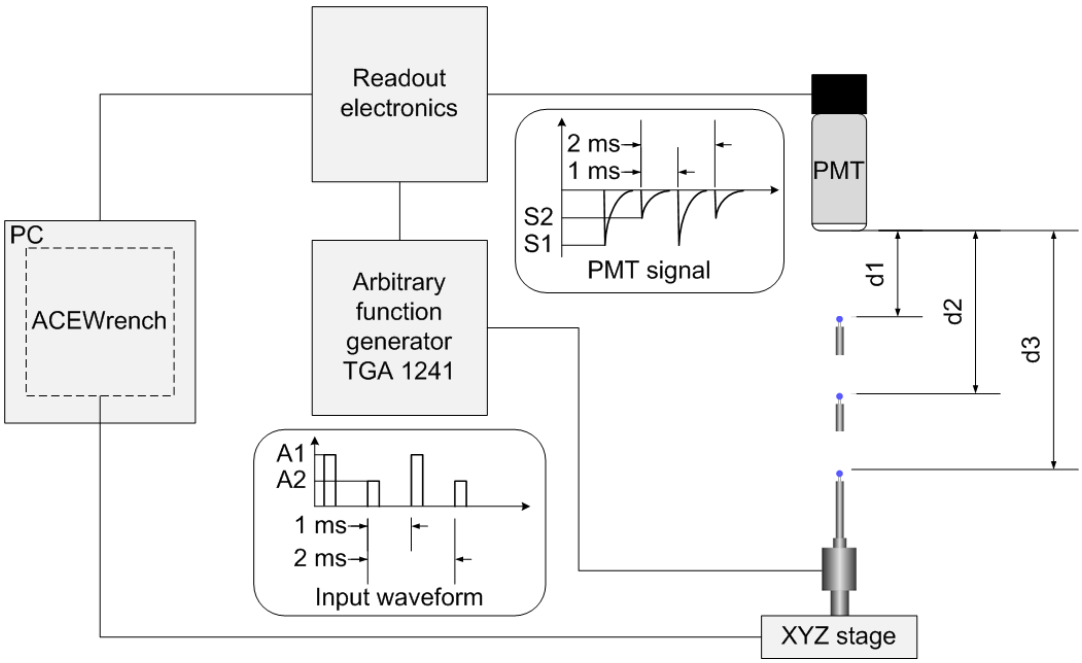

FIGURE 5.4: Block diagram of the experimental system used for pulse mode linearity measurements.

Results

The results shown in figure 5.5 were obtained in high light output and exhibit the non-linear behaviour of the PMT 4 (figure 5.5 (left)) and PMT 5 (figure 5.5 (right)). Each figure depicts the signal measured at higher (S_H, blue curve) and lower (S_L, black curve) excitation pulse amplitude as a function of the distance between the light source and the PMT window. The light source was pulsed at $1\,\mathrm{kHz}$ with $600\,\mathrm{ns}$ pulses, which originated peak current amplitudes of up to $\sim 4.7\,\mathrm{mA}$ from PMT 4 at $d = 10\,\mathrm{mm}$. The red curve represents the deviation of the ratio of the two signals relative to the value measured at $d = 50\,\mathrm{mm}$. The two PMTs have different deviation rates, the PMT 4 having a higher deviation rate than PMT 5. This deviation can be explained due to the fact that the PMT 4 gain is about double of the PMT 5 and therefore the spatial charge effect is more intense. From the experimental results depicted in figure 5.6 and figure 5.7, it can be seen that when the light source is at distances larger than $\sim 25\,\mathrm{mm}$ the deviation from linearity of all PMTs is better that $\sim 2\,\%$. The signal of PMT 4 was used as a reference to establish the linear operation conditions of all PMTs. It was seen that if the PMT4 peak current was kept below $\sim 1\,\mathrm{mA}$ (which happens at $\sim 25\,\mathrm{mm}$), all PMTs were operating under linear condition with a linearity better that $2\,\%$[4]. Accordingly to these

[4]The relatively low peak current ($\sim 1\,\mathrm{mA}$) is expected as the PMT passive voltage divider did not include other pulse output linearity countermeasures than the decoupling capacitors

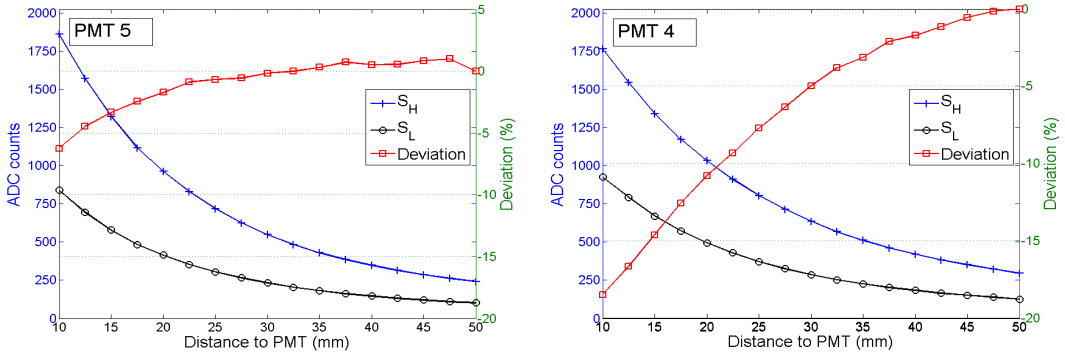

FIGURE 5.5: PMT 5 (left) and PMT 4 (right) charge signal measured at higher (A_1, blue curve) and lower (A_2, black curve) excitation pulse amplitudes. The light source was pulsed at $1\,\mathrm{kHz}$ with $600\,\mathrm{ns}$ width pulses. The red line represents the deviation from linearity of the ratio of the two curves at each position d (see definition in equation (5.4)).

results, for each illumination conditions i.e. number of photons per pulse, the pulse characteristics were set such that the PMT 4 anode signal peak current was always smaller than $1\,\mathrm{mA}$. As can be seen under these operational conditions, the linearity is better than $2\,\%$ showing the negligible effect of the increased pulse width from $1.4\,\mu\mathrm{s}$ to $1.9\,\mu\mathrm{s}$ to pulse mode linearity. Additionally, there is a good agreement between the results obtained at $500\,\mathrm{Hz}$ (figure 5.7) and $1\,\mathrm{kHz}$ (figure 5.6), showing as expected, the negligible contribution to non-linearity of the variation of the voltage distribution in the voltage divider due to the current flowing. In this work, unless stated otherwise, the pulse rate will be always $<=1\,\mathrm{kHz}$.

5.4 Relative gain

In general, under the same illumination conditions, the output signal of a set of PMTs of the same model may vary substantially. As stated in chapter 2, this difference is mostly due to variations in the quantum efficiency and dynode chain gain. To compare the output of the PMTs under the same illumination conditions, *relative gain* is typically used, which is defined as the ratio of the signal of a specific PMT to that of a reference PMT, $PMT_{ref.}$[5]. The

between the 3 last stages. However as the pulse characteristics of the light source are controllable, this did not constitute a problem in this study. There are, however, other voltage divider designs that allow high pulse linearity 5 to 10 times more than that obtained with "normal voltage-dividers" (equally divided circuits) such as the tapered voltage divider [43].

[5]Accurately, there is an abuse of the term *relative gain*, as the signal of each PMT depends not only on the gain of the electron multiplier but also on other characteristics such as quantum efficiency or electron collection. The quantity that relates the output charge of a PMT

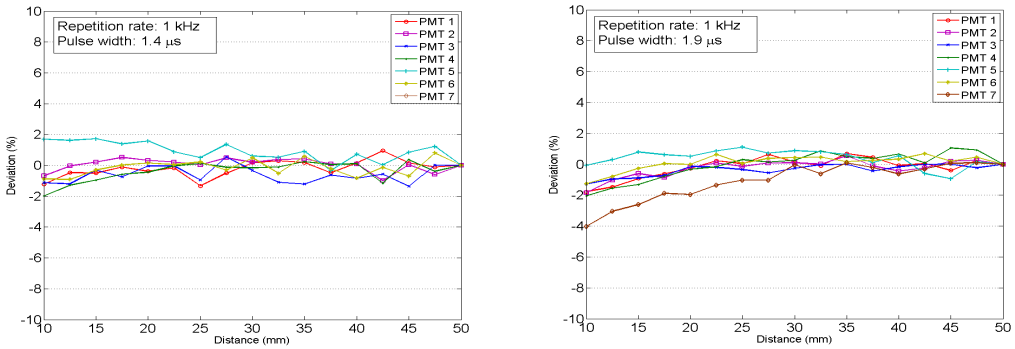

FIGURE 5.6: Ratio between the PMTs charge signal at higher and lower pulse amplitude vs. distance. The light source was pulsed at 1 kHz with 1.4 µs (left) and 1.9 µs (right) pulse widths.

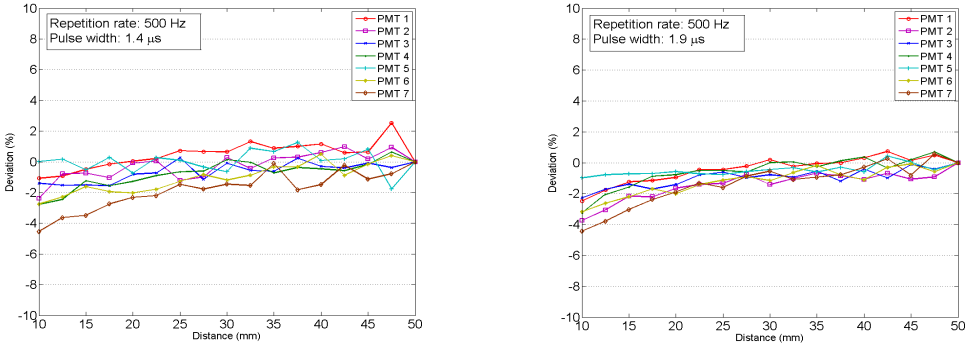

FIGURE 5.7: Ratio between the PMTs charge signal at higher and lower pulse amplitude vs. distance. The light source was pulsed at 500 Hz with 1.4 µs (left) and 1.9 µs (right) pulse widths.

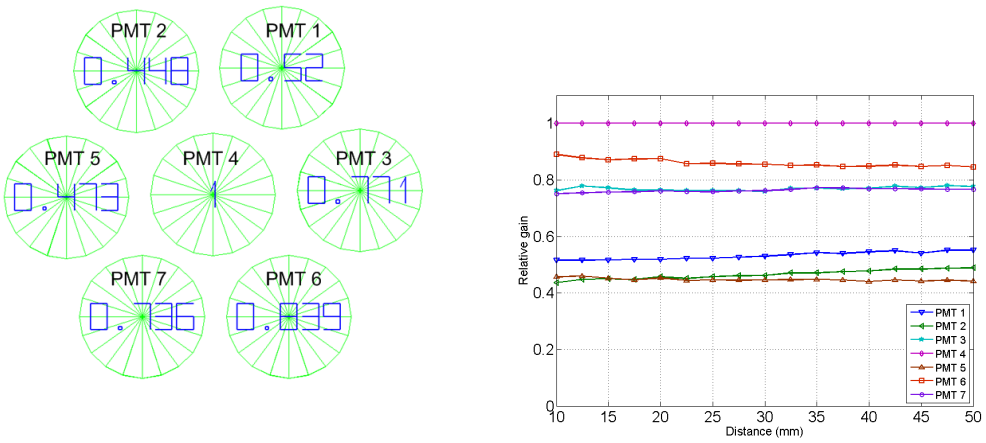

FIGURE 5.8: Left: Relative gains of the PMTs measured at 20 mm. Right: Relative gains of the PMTs vs distance between the light source and the PMT window.

relative gain is used in position reconstruction, for example with the center of gravity algorithm, where it is assigned as the weight to each PMT (see chapter 3). The measurement of the relative weights was done in the workbench, with the light source placed along the axis of the each PMT, as given by the position of the center of each PMT $(x, y)_{PMT}$ (measured in section 5.1) at the distance d. The light source was operated in pulse mode at 1 kHz with all PMTs operating linearly. The relative PMT gains measured at d = 20 mm are shown in figure 5.8 (left) depicting the array of PMTs with the relative gains calculated with reference at the central PMT. In figure 5.8 (right) the gains of the PMTs are shown *vs* the distance between the PMT and the PMT window. The PMT relative gain varies between ∼0.5 and 1 which is common between non-selected PMTs of the same type. As can be seen in figure 5.8, the overall variation of the relative gains with distance d is relatively small (under 5% for 5 out of the 7 PMTs). This result was not unexpected due to the small anisotropy of the light source and suppressed scattered light. There are, however, relative gain variations of 7% and 12% in PMT 1 and 2 respectively. These variations are most probably due to the combined effect of the photocathode spatial and the angular uniformity of the PMT.

with the incident light intensity is anode sensitivity (in units of A/lm) and therefore the correct term would be relative anode sensitivity.

5.5 Uniformity

In general, the output signal of a PMT also depends on the location where the photons hit the photocathode and on the angle of incidence. Formally that can be stated as follows

$$S_\lambda = S_\lambda(x, y, \theta, \phi) \tag{5.5}$$

where S is the output signal, (x, y) are the coordinates on the photocathode and (θ, ϕ) describe the angle of incidence. In this section, a study of the spatial uniformity and angle dependence is presented, which allowed a better understanding of these characteristics of the PMTs. These results also point out the difficulties of a parameterization of these characteristics based on detailed experimental measurements, as it would require a complex and time consuming experimental measurements.

5.5.1 Spatial uniformity

The variation of the output signal of a PMT with respect to the location where the photons hit the photocathotode is commonly referred to as "spatial uniformity". It depends very much on the wavelength and typically tends to improve near the spectral range corresponding to maximum sensitivity [55]. There are several factors that determine the spatial uniformity of a PMT, such as uneven photocathode deposition, variation of photoelectron collection and electron multiplier uniformity. Non-uniformity may have an adverse effect on the performance of an Anger camera, degrading the energy resolution of the reconstructed events [43].

Experimental system

The experimental system consisted of the workbench with the light source replaced by a collimator with an inbuilt light source. The data acquisition was controlled using the ACEWrech control software configured to scan each PMT window. The details of the design of the collimated light source are depicted in figure 5.9. The light generated by an LED passes through a series of metal discs placed at unevenly distances with $\sim 1\,\mathrm{mm}$ diameter holes at the center. The disc separation and the holes profile were design in order to reduced the amount of scattered light. The profile of the collimator light beam was measured by recording an image of the spot resulting from the impinging light beam on a white paper target placed at several different

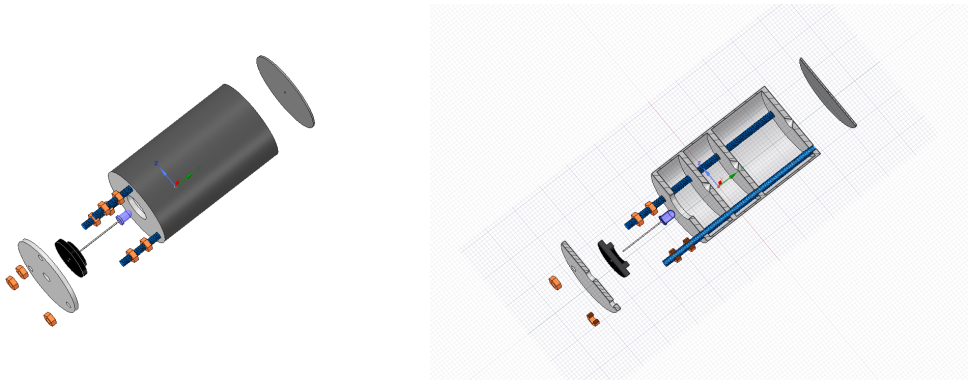

FIGURE 5.9: Collimated light source assembly: exploded view (left) and cut-away exploded view (right).

distances from the collimated light source output surface. The experimental set-up, consisting of the collimated light source, a white paper target and a digital single lens reflex camera (DSLR camera) is depicted in figure 5.10a. The results are shown in figure 5.11. The profile of the beam was approximately circular, with a suitable divergence having $\sim 1\,\mathrm{mm}$ FWHM at $5\,\mathrm{mm}$ and $\sim 1.1\,\mathrm{mm}$ FWHM at $20\,\mathrm{mm}$.

(A)

FIGURE 5.10: Left: Experimental set-up. Right: Color coded image of the measured light beam profile.

Results

The uniformity was mapped scanning the photocathodes in $1\,\mathrm{mm}$ steps for perpendicular incidence with the collimated light source fitted with an $470\,\mathrm{nm}$ LED. The distance between the light source output surface and the PMT window was $5\,\mathrm{mm}$. Figure 5.12 (left) shows the color coded PMT uniformity as a function of the light source position normalized to the maximum sensitivity. The black lines depict the glass envelope inner and outer limits, whereas a white line delimits the hole of the holding mask. Figure 5.12 (right) shows the PMT signal averaged over the radial distance of all PMTs and normalized to the signal at the PMT center. The uniformity of all PMTs is shown

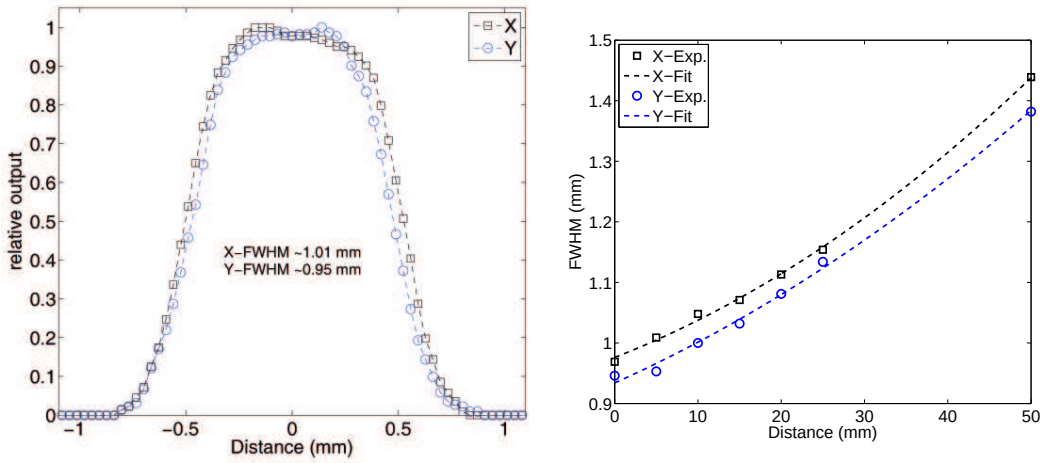

FIGURE 5.11: Left: Sections of the beam along the X and Y directions. Right: Variation of the FWHM of the X and Y section with distance between the collimator and the target.

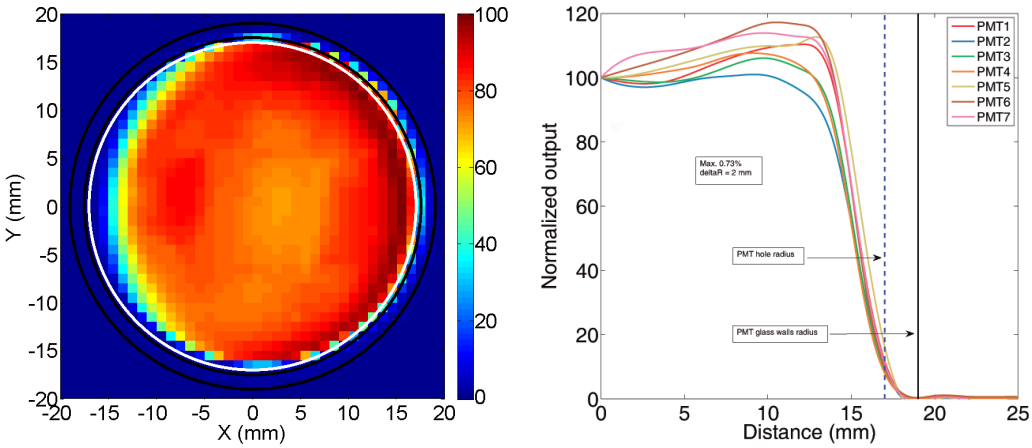

FIGURE 5.12: Left: Spatial uniformity of the PMT 5 (SN8932). The black lines represent the inner and outer limits of the glass envelope. The hole of the PMT holding mask ($34\,\mathrm{mm}$ diameter) is represented by a white line. Right: Average PMT output as a function of the distance to the center of the PMT. The output of each individual PMT was normalized to the value at the center.

in figure 5.13 at the positions they occupy in the camera. The uniformity of each PMT is shown normalized to the maximum output value. These results showed that the PMTs have a common uniformity pattern with the sensitivity increasing with the distance from the center of the PMTs. The typical sensitivity increases from the center to the border are in the order of $20\,\%$.

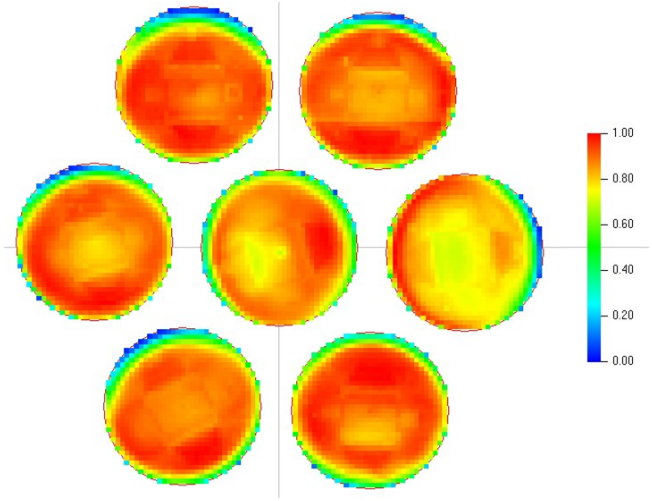

FIGURE 5.13: Camera spatial uniformity.

5.5.2 Angular response

The PMT response also depends on the angle of incidence of the light on the photocathode. This dependence is usually called the angular response [43]. Generally, the photocathode sensitivity improves at large angles of incidence as the incident light transmits across a longer distance increasing the photoconversion probability. Additionally, this increase in sensitivity usually becomes larger at longer wavelengths due to the optical dispersion [43]. To measure the angular response the photocathode was illuminated with a rotating collimated light source while measuring the output signal of the PMT. A schematic diagram of the experimental set-up is shown in figure 5.14 (left). The collimated light source was fixed to an arm moving around an axis contained in the plane of the photocathode of the PMT. The angular step of the circular motion was 1.8°. The light was generated by a common $5\,\mathrm{mm}$ diameter blue LED ($470\,\mathrm{nm}\pm15\,\mathrm{nm}$). The PMT was mounted on an XYZ stage in order to allow changes in the position of the light spot over the surface of the photocathode. The distance between the PMT window and the collimator output was $20\,\mathrm{mm}$. The PMT signal was fed to a charge ADC LeCroy 2249w gated synchronously with the pulsed LED. The readout and acquisition system were controlled using a custom-made specific LabVIEW application. The light spot had approximately $1.1\,\mathrm{mm}$ FWHM for perpendicular incidence on the photocathode (i.e. theta = 90°). For larger angles of incidence it became an ellipse with a major axis increasing with the angle of incidence as demonstrated in figure 5.14 (right) showing the variation of the major axis length with the angle of incidence. For larger angles of incidence, the loss of locality and the photocathode non-uniformity limits the validity of the measurement.

However, for angles of incidence smaller than 80° the length of the major axis is smaller than $6\,\mathrm{mm}$, which combined with a relatively smooth variation of the response over the photocathode area, introduces a negligible error. The

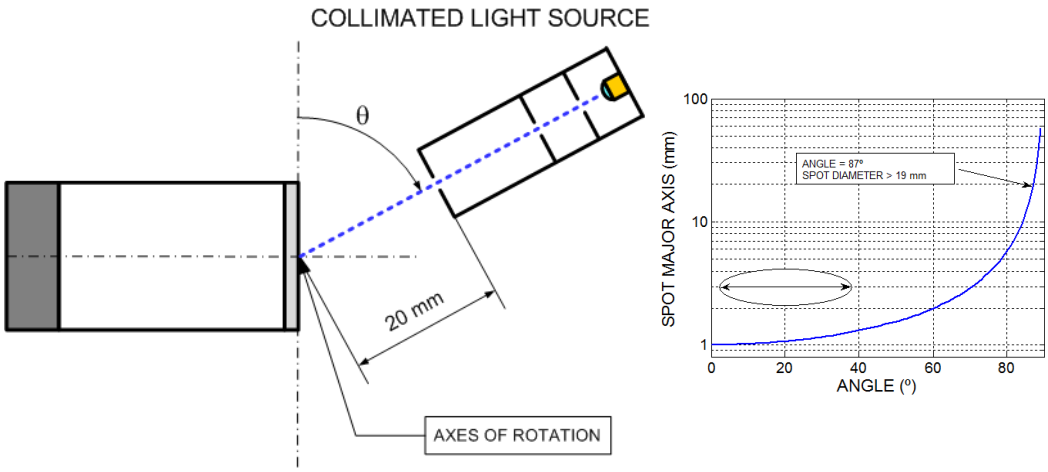

FIGURE 5.14: Left: Experimental system used to measure the angular response of the PMT at several positions on the window. Right: Variation of the major axis of an ellipse with the angle of incidence. At perpendicular incidence both major and minor axis are equal to $1\,\mathrm{mm}$ (i.e. it is a $1\,\mathrm{mm}$ diameter circle). For large angles of incidence the photocathode non-uniformity limits the validity of the measurement.

light source was operated in pulse mode with pulses of $50\,\mathrm{ns}$ in duration. The light output was set in order to allow linear operation of the PMT with readings within the dynamic range of the ADC. The measurements were done as follows: the position of the spot on the PMT window was chosen by moving the PMT along XY plane when the collimated light source was at $\theta = 90°$ (see figure 5.14). The control system positioned the collimated light source at 0° and acquired 100 signal samples between $\theta = 0°$ and $\theta = 180°$ at angular steps of 1.8°. Several measurements assured the stability and reproducibility of the system. Figure 5.15 (right) was made to aid the interpretations of the results shown in figure 5.15 (left) and it shows the internal metallic structure of the PMT as seen perpendicularly to the window. The blue circles represent the positions where the measurements occur. The variation of the PMT response with the angle of incidence is shown in figure 5.15 (left) for the "TOP" and "CENTER" positions as depicted in figure 5.15 (right). The profile of the local angular dependence depends on the position on the photocathode. For the same position, the angular dependence is very structured and the results indicate a correlation with the internal metallic high reflective structure of the PMT, which seems to enhance the response of the PMT by reflecting light back to the photocathode.

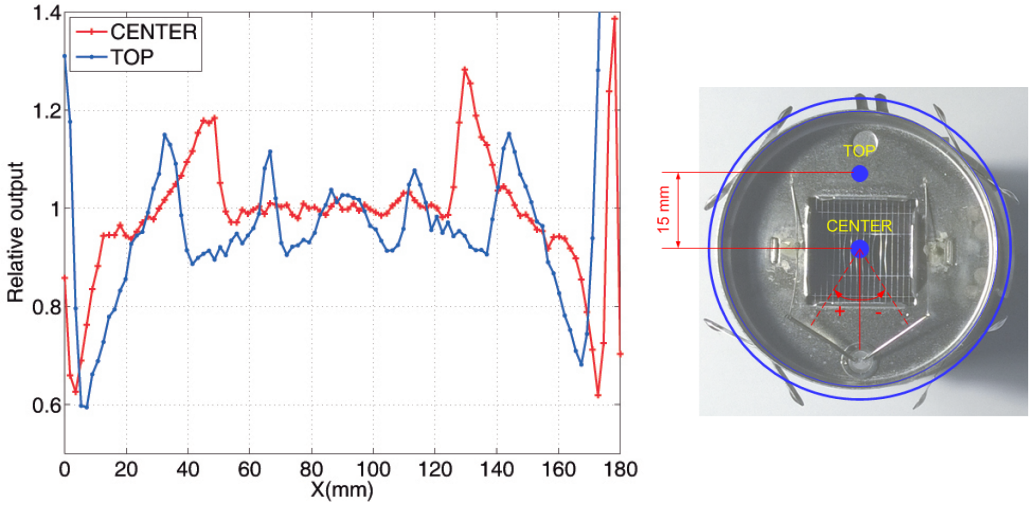

FIGURE 5.15: Left: Variation of the PMT response with the angle of incidence. Right: Location of the positions "TOP" and "CENTER" on the PMT window. Note the metallic, highly reflective PMT internal structure.

5.5.3 Comments on the uniformity

The experimental results presented in this section demonstrate the rather difficult task that is to parametrize the PMT response from experimental data. At each location on the photocathode of a PMT, the response to light of a definite wavelength will vary with the direction of incidence given by (θ, ϕ). This means that in order to parametrize $S_\lambda(x, y, z, \theta, \phi)$ at each single location (x, y), the response would have to be measured varying the polar θ and the azimuthal angles ϕ.

5.6 Light response function (LRF)

The light response functions of the PMTs (see chapter 3) were measured at a distance Z between the light source and the PMT plane, sweeping the light source in XY plane through the nodes of a grid of regularly spaced $2.5\,\mathrm{mm} \times 2.5\,\mathrm{mm}$ positions while recording the PMT signal at each node. Results are shown in figure 5.16 for Z = $10\,\mathrm{mm}$, $30\,\mathrm{mm}$ and $50\,\mathrm{mm}$. The response of the PMTs has nearly perfect axial symmetry, confirming that scattered light has a small contribution to the signal, as was intended for these verification conditions of the setup. The center of symmetry of each PMT, found by fitting a Gaussian surface to the corresponding signal mapping, had a maximum deviation from the PMT's window axis smaller than $1\,\mathrm{mm}$. Taking advantage of the axial symmetry the LRFs can be represented as functions of the distance to the center of symmetry as shown in figure 5.17. As it can be seen in figure

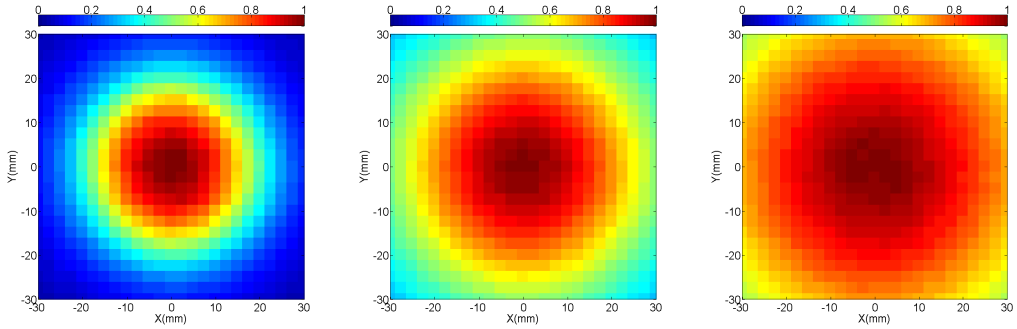

(A) Z = 10 mm (B) Z = 30 mm (C) Z = 50 mm

FIGURE 5.16: Signal of the PMT 4 vs light source position in the XY plane measured at Z = 10, 30 and $50\,\mathrm{mm}$ distance between the light source and the PMT window.

5.17 (right) the solid angle subtended by the PMT photocathode at the source location, deviates very little from the experimentally measured LRF.

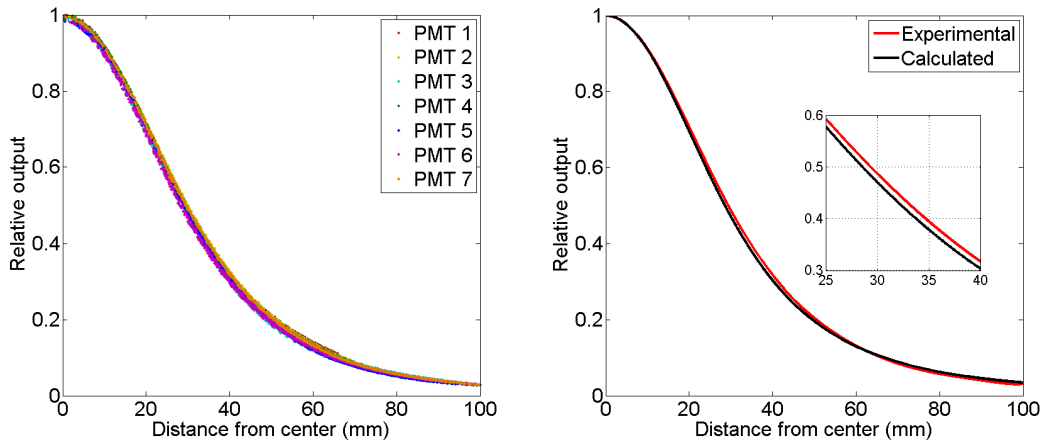

FIGURE 5.17: Left: measured light response function of the PMTs ($Z = 30\,\mathrm{mm}$). Right: experimental LRF (red line) and the calculated LRF (black line) considering the diameter of the PMT and the distance between the light source and the PMT plane ($Z = 30\,\mathrm{mm}$).

5.7 Absolute calibration of the PMT SN8938

5.7.1 Photodiode calibration

The absolute calibration of the PMT 4 (SN8938) was done using a calibrated photodiode AXUV100G[6]. This photodiode has an active area of $10\,\mathrm{mm} \times 10\,\mathrm{mm}$

[6]The photodiode AXUV100G is market by IRD Inc., U.S.A.

with responsivity $R_{PD(\lambda)}$ covering a broad spectral range from vacuum ultra violet (VUV) to near infrared (NIR). The photodiode had a recent responsivity calibration at NIST, but it was limited to the VUV-UV range and consequently it was necessary to extend it to the emission band of the light source ($470\,\mathrm{nm} \pm 15\,\mathrm{nm}$). The responsivity was measured at $450\,\mathrm{nm}$ wavelength using an L6402 calibrated halogen lamp[7]. This single wavelength calibration was then compared with the photodiode responsivity spectrum provided by the manufacturer to infer $R_{PD}(\lambda = 470\,\mathrm{nm})$[8]. The experimental set-up used during the calibration process on an optical rail mount is depicted in figure 5.18. The calibrated halogen lamp was powered by a HP 6642A pro-

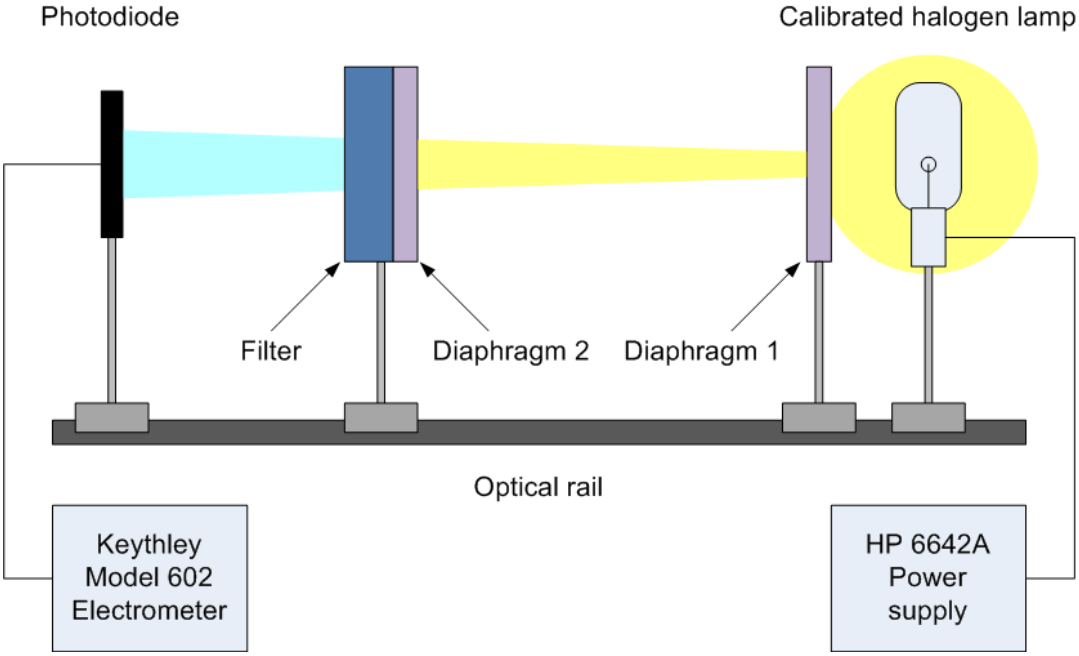

FIGURE 5.18: Experimental set-up to calibrate the photodiode.

grammable power supply. The light from the lamp was first screened by a diaphragm (Diaphragm 1) with $\sim 10\,\mathrm{mm}$ diameter aperture. The light was collimated by another diaphragm (Diaphragm 2) with $6\,\mathrm{mm}$ diameter aperture placed in contact with a $25.4\,\mathrm{mm}$ diameter bandpass filter with a center wavelength of $450\,\mathrm{nm}\pm2\,\mathrm{nm}$ and $10\pm2\,\mathrm{nm}$ FWHM. The photodiode current was measured by a Keythley model 602 electrometer. The optical elements (PD, filter and halogen lamp) are shown in the figure 5.20 jointly with calibration data provided by the respective manufacturer.

[7]These calibrated halogen lamps are market by International Light Technologies, Inc., U.S.A)

[8]This procedure was considered reasonable since the PD responsivity spectrum is a smooth curve close to that wavelength band. Moreover, the required responsivity, $R_{PD}(\lambda = 470\,\mathrm{nm})$ is just $20\,\mathrm{nm}$ away from the calibrated responsivity $R_{PD}(\lambda = 450\,\mathrm{nm})$.

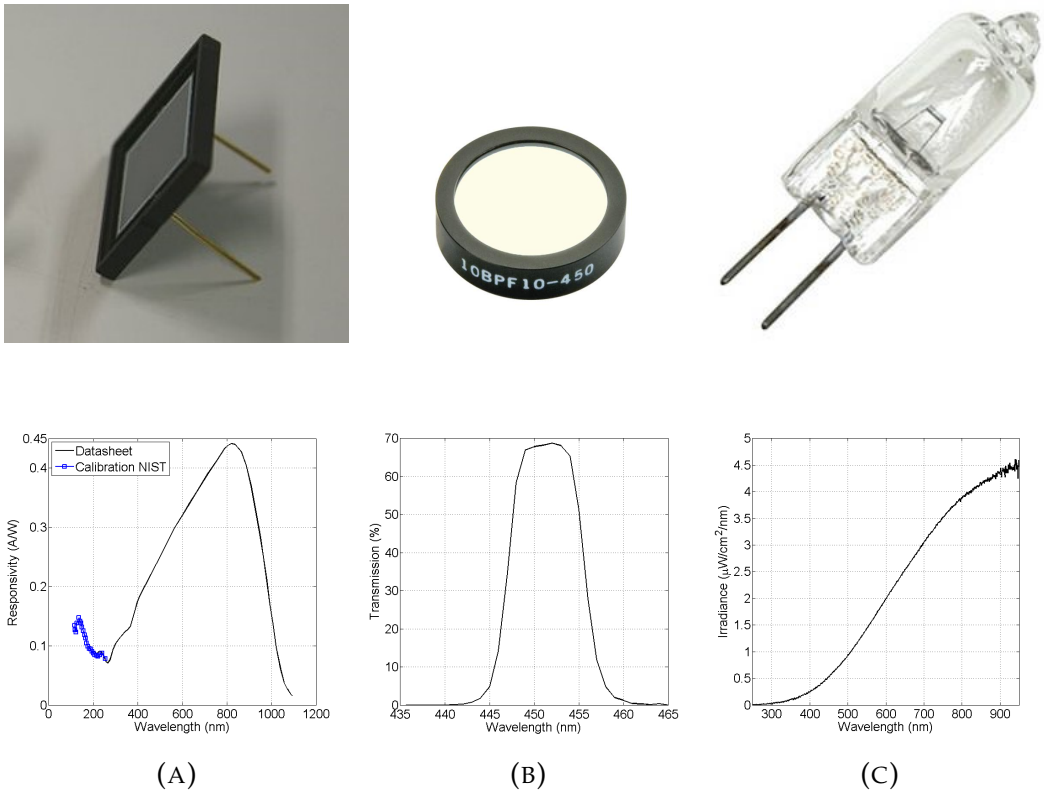

(A) (B) (C)

FIGURE 5.20: First column: photodiode. Photo (top) and responsivity (bottom); Second column: Bandpass filter ($450\,\mathrm{nm}\pm2\,\mathrm{nm}$ and $10\pm2\,\mathrm{nm}$ FWHM). Photo (top) and transmission spectrum (bottom); Third column: halogen lamp. Photo (top) and irradiance spectrum (bottom).

Since the photodiode and optical filter surfaces are partially reflective, the PD signal may have a non-negligible reflected light component from the filter if the filter is at a close distance from the photodiode. In order to evaluate the contribution of the reflected light to the PD signal, the light source position was fixed at $\sim 40\,\mathrm{cm}$ from the optical filter to keep the divergence of the light coming out of the optical filter small. The photodiode signal was registered while the distance between the photodiode and the optical filter was increased by moving the photodiode and keeping the position of the filter. The results show that for distances between the filter and the photodiode larger than $\sim 25\,\mathrm{mm}$, the contribution of the reflected light is negligible (figure 5.21 (left)). In accordance with this result, the distance between the photodiode and the optical filter was set to $\sim 25\,\mathrm{mm}$.

The point source approximation was tested measuring the photodiode current I_{PD} at several distances between the halogen lamp and the optical filter. The results are shown in figure 5.21 depicting the photodiode current vs distance from calibrated halogen lamp (black circles). If the calibrated halogen lamp can be approximated by a point source, then $L = I_{PD} \times$

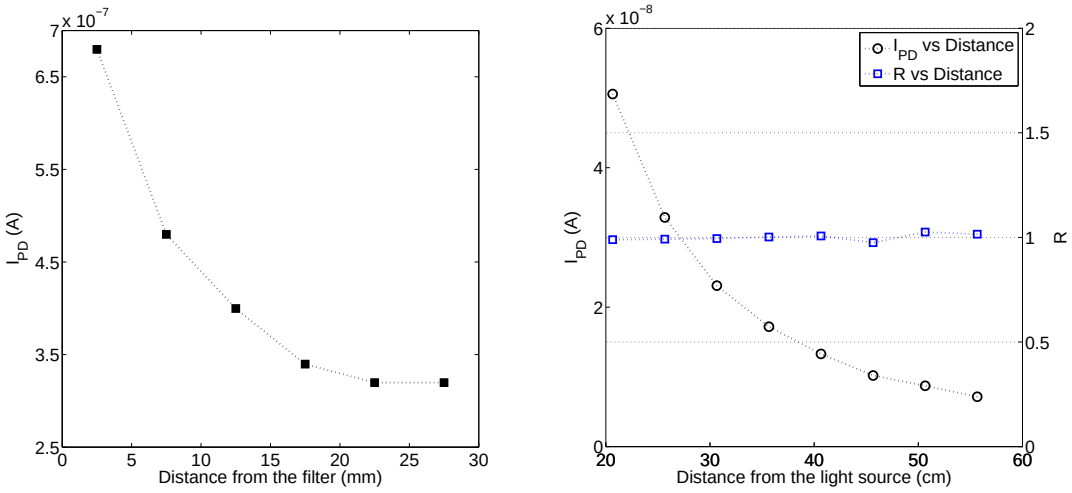

FIGURE 5.21: Left: evaluation of the contribution of the reflected light to the PD signal. Right: Evaluation of the point source approximation. The blue line represents the average $I_{photodiode} \times Distance^2$.

$D^2_{PD-Halogen\ lamp}$ should be constant (here d_{PD-HL} represents the distance between the photodiode and the calibrated halogen lamp.). L vs d_{PD-HL} is depicted in figure 5.21 (right) by blue squares, showing that the light source can be considered punctual[9] for $d_{PD-HL} > 20\,\mathrm{cm}$.

The radiant power P_{PD} received by the photodiode is calculated as follows

$$P_{PD} = \int_{\lambda_i}^{\lambda_f} E_e(\lambda) Tr(\lambda) \left(\frac{D_{PD}}{D_{calib}}\right) A_{PD} d\lambda \tag{5.6}$$

where $E_e(\lambda)$ is the light source irradiance, $Tr(\lambda)$ the filter transmission at wavelength λ, D_{calib} the distance between the detector and the center of the lamp during the halogen lamp calibration process ($10\,\mathrm{cm}$, according to the data provided by the manufacturer) and A_{PD} is the exposed area of the photodiode ($0.283\,\mathrm{cm}^2$). λ_i and λ_f define the wavelength range of the bandpass filter. With the light source operating at the calibration conditions reported by the seller i.e. ($6\,\mathrm{V}$, $1.6795\,\mathrm{A}$), the photodiode current measured with d_{PD-HL} = $21\,\mathrm{cm}$ was $40.7\,\mathrm{nA}$. According, to equation 5.6, the radiant power is $0.222\,\mu\mathrm{W}$ and therefore the corresponding photodiode responsivity is $R_{PD}(\lambda = 450\,\mathrm{nm}) = 0.214\,\mathrm{A/W}$ which is the same value given by the responsivity curve provided by the manufacturer ($0.214\,\mathrm{A/W}$). The uncertainties in the lamp irradiance and in the bandpass filter transmission (both

[9] As the filament of the lamp is $3\,\mathrm{mm}$ long this result was not unexpected due to the "five times rule" (general rule of thumb that states that the point source approximation can be used if the distance to the light source is greater than five times the largest dimension of the source).

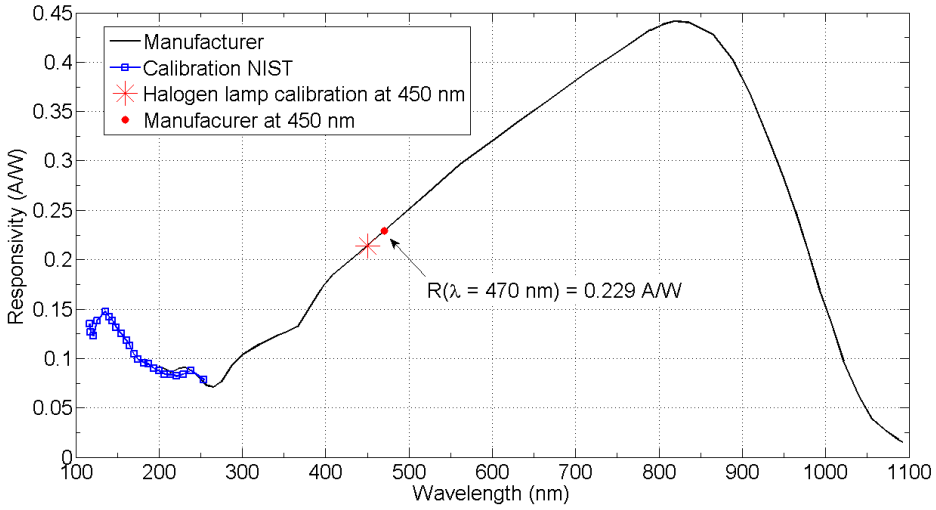

FIGURE 5.22: Photodiode AXUV-100G responsivity spectrum.

around 2%) contribute the most to the total uncertainty of the measurement. The uncertainties in geometry, current measurement are comparatively negligible. Following this result it was decided to use the photodiode responsivity curve ($R_{PD}(\lambda)$) reported by the manufacturer, which at $470\,\mathrm{nm}$ has a value of $0.229\,\mathrm{A/W}$. Since this wavelength is very close to the calibration wavelength ($450\,\mathrm{nm}$), an uncertainty of less than $\sim 5\%$ is also expected in $R_{PD}(\lambda = 470\,\mathrm{nm})$.

5.7.2 PMT calibration

The photodiode calibration presented in the previous section was done operating the calibrated halogen lamp in direct current mode whereas the photomultipliers will be operating in pulse mode. Hence, it is required to check if the photodiode DC mode calibration holds for pulsed light conditions, which is equivalent to checking the linearity of the photodiode with the pulsed light duty cycle up to $\sim 100\%$ i.e. direct current mode. This was done using the set-up depicted in figure 5.23 (left). The pulser generated $6.8\,\mathrm{V}$ amplitude rectangular pulses at $1\,\mathrm{kHz}$ repetition rate. The photodiode current was measured with Keithley 602 Electrometer at each duty cycle value in the range $\sim 1\%$ to $\sim 50\%$. The peak current I_{peak} flowing through the LED was measured at the resistor R using a digital oscilloscope and was $30\,\mathrm{mA}$. In DC mode ($\sim 100\%$ duty cycle) a programmable power supply HP 6642A was set to $6.8\,\mathrm{V}$. The results shown in figure 5.23 (right) exhibit an excellent linearity of the photodiode with the duty cycle up to DC operation and therefore it was concluded that the calibration presented in the previous section is also

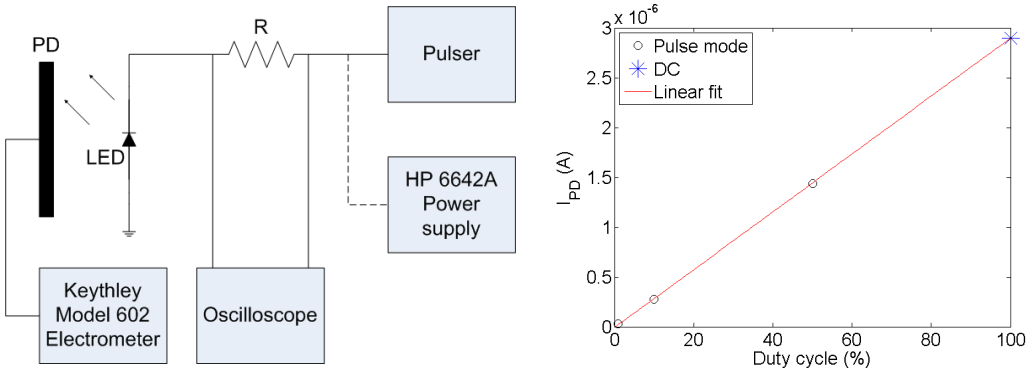

FIGURE 5.23: Left: Experimental system. Right: Photodiode current (I_{PD}) vs pulsed light duty cycle.

valid for pulse mode operation.

The cross calibration of PMT4 was done in the workbench with one of the outer PMTs replaced by the photodiode. A custom-made photodiode holder, tightly fitting the PMT slots, allowed the sensitive surface of the PD to be positioned on the same plane of the PMT window. The light source was operated in pulse mode in steady state conditions at $10\,\mathrm{kHz}$ repetition rate with $1.5\,\mu\mathrm{s}$ pulse width. The system allowed the light source to be moved in the XY plane and record the signal of the PMT and the photodiode along the axis of both devices at each distance Z. The number of emitted photons per pulse was firstly determined by the photodiode current using the following relation

$$N_{Photons} = \frac{I_{PD}}{R_{470\,\mathrm{nm}} \cdot E_{ph_{470\,\mathrm{nm}}} \cdot f_{\Omega_{PD}} \cdot RR} \tag{5.7}$$

with $R_{470\,\mathrm{nm}}$ being the spectral responsivity of the PD at $470\,\mathrm{nm}$ wavelength, $Eph_{470\,\mathrm{nm}}$ the energy of the emitted photons, $f_{\Omega_{PD}}$ the fractional solid angle subtended by the PD window at the light source position and RR the repetition rate of the light source pulser. The cross-calibration of the PMT can be done noting that the number of emitted photons can also be calculated from a PMT charge signal distribution characterized by the mean μ and standard deviation σ using equation 2.10,

$$N_{Photons} = \left(\frac{\mu}{\sigma}\right)^2 \cdot \frac{C}{f_{\Omega_{PMT}}} \tag{5.8}$$

where $f_{\Omega_{PMT}}$ is the fractional solid angle subtended by the PMT window at the light source position and C a constant depending only on the electronic properties of the PMT. To determine the constant C, the PD and $PMT4$ signals were measured at $Z = 50\,\mathrm{mm}$ along the axis of both devices. In figure 5.24 a histogram is depicted of both the ADC pedestal and PMT fitted with

Gaussian curves. The parameters of the fit were used to calculate the $(\mu/\sigma)^2$

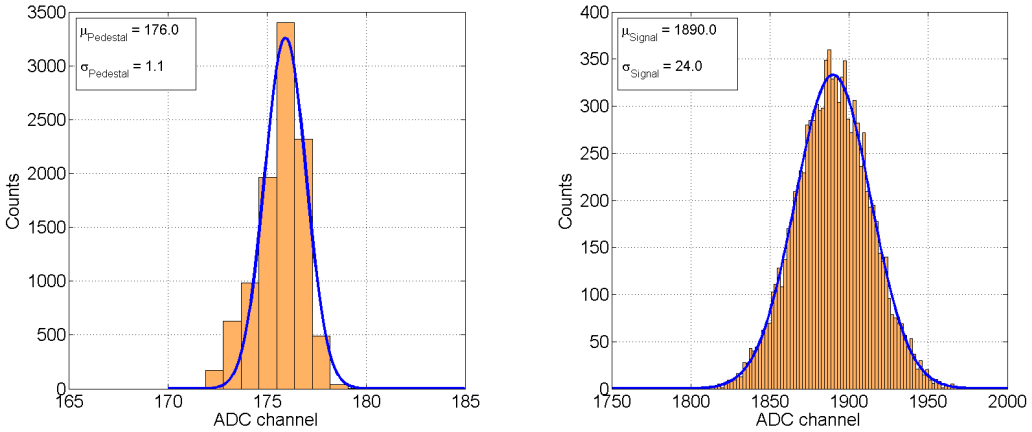

FIGURE 5.24: Left: Pedestal. Right: PMT signal.

in equation 5.8 as follows

$$\mu_{Eff} = \mu_{Signal} - \mu_{Pedestal} \tag{5.9}$$

were the μ_{Eff} is the PMT effective signal, μ_{Signal} the measured PMT signal and $\mu_{Pedestal}$ is the mean pedestal. Likewise the effective PMT signal standard deviation σ_{eff} was calculated combining the standard deviations of the two distributions as follows

$$\sigma_{Eff} = \sqrt{\sigma^2_{Signal} - \sigma^2_{Pedestal}} \tag{5.10}$$

In order to calculate the value for C first, the number of emitted photons was determined using equation 5.7 and then C was calculated from equation 5.8 using the values μ_{Eff} and σ_{Eff}. After this process it was found that $C = 6.7 \pm 0.3$, where the $\sim 5\%$ uncertainty was determined based on the expected uncertainty of the photodiode responsivity ($\sim 5\%$). Therefore, the number of emitted photons per pulse can be now obtained from the PMT 4 charge histograms using the following relation

$$N_{Photons} = \left(\frac{\mu}{\sigma}\right)^2 \cdot \frac{6.7}{f_{\Omega_{PMT}}} \tag{5.11}$$

In equation 5.11 it is implicit that light emission is isotropic, which is not absolutely true for the light emitted from the source presented in this work. Nevertheless, for easiness of comparison, the number of photons emitted per pulse by the light source, as calculated from equation 5.11, will be given assuming isotropic light emission in 4π.

5.7.3 Detection probability

The detection probability DP can be defined as the ratio between the number of photons hitting the photocathode window $N_{Photons}$ and the number of photoelectrons entering the multiplier chain N_{Phe}, thus

$$DP = \frac{N_{Phe}}{N_{Photons}}. \tag{5.12}$$

The detection probability of each individual PMT is a required parameter when the position reconstruction is done with the maximum likelihood algorithm, as it allows the units of the PMT readout to be convert to photoelectrons (which are the units of the likelihood function as defined in chapter 3). The PMT charge histograms obtained at well defined light source positions can be used to estimate the detection probability of the individual PMTs from equation 5.12, since the calibrated PMT allows $N_{Photons}$ to be calculated. The number of photoelectrons entering the multiplier chain can be calculated from the PMT signal distribution characterized by the mean μ and variance σ^2 as follows

$$N_{Phe} = \left(\frac{\mu}{\sigma}\right)^2 \cdot ENF \tag{5.13}$$

where ENF is the excess noise factor of the PMT (see also chapter 2 and Appendix B). As was seen in chapter 2, the ENF factor can be computed from the PMT single electron response using the formula

$$ENF = 1 + \left(\frac{\sigma_G^2}{< G >^2}\right) \tag{5.14}$$

where $< G >$ is the mean gain of the PMT and σ^2 the associated variance. A method based on the direct calculation of the average charge of the single electron response of the PMT[10] (see [56]) was chosen to determine the gain of the PMTs since this technique was simple to implement in the workbench while providing acceptable results. Let $n(q)$ be the pulse height distribution of PMT anode pulses with charge q, measured when the PMT is operating in single photoelectron conditions i.e. the probability of detecting more than

[10] In fact $< G >$ (and σ_G) can be determined using the single electron response of the PMT, either by direct computation [56] or deconvolution [57]. Direct determination of the average PMT gain (and variance) by measuring the current at the first dynode and comparing it with the current at the anode measured under the same illumination conditions is usually only practical for low gain values ($< 10^4$) because if the anode current exceeds a certain maximum the PMT is no longer operating linearly. For higher gains, a direct current measurement can be done using a well characterized neutral density filter when measuring the anode current [55].

one photon is very low[11]. The average anode charge per photoelectron, $< q >$ is

$$< q >= \frac{\int_0^\infty n(q)qdq}{\int_0^\infty n(q)dq} = e < G > \tag{5.15}$$

from which $< G >$ may be calculated. The single electron response of the PMTs was recorded with steady weak light intensity with the single photon detection probability ranging between $\sim 5\%$ and $\sim 10\%$. The measurements were performed pulsing the light source at 100 kHz with $50\,\mathrm{ns}$ duration pulses. The signal from the PMT was fed first to a Canberra 2005 preamplifier and then to a Canberra 2020 spectroscopy amplifier. The single electron response spectrum of each PMT was recorded using a multichannel analyzer (CANBERRA 35+), gated synchronously with the light source. At each measurement the average current was also measured feeding the PMT anode signal directly to a Keithley 602 electrometer. The noise spectrum (hereafter referred to as pedestal) was recorded without voltage applied to the PMT (see figure 5.25). The pedestal is well described by a Gaussian curve centered at channel 11 with 3 channels FWHM. The PMT background spectrum was recorded with the PMT in full darkness and is shown in figure 5.25 together with the PMT response measured at three different light levels. The background spectrum is very similar to the response measured in very weak light conditions. This fact is likely due to the relative low work function of the multialkali photocathode enabling thermionic emission of photoelectrons at room temperature.

In figure 5.25, the SER of two PMTs of the camera are shown scaled for convenience of presentation. As can be seen, the shape of the SER varies considerably among the PMTs (these two represent the extreme cases), some of them barely resolving single electrons (e.g. PMT 8933).

As already mentioned the shape of the single electron response of the PMTs is practically indistinguishable from the background. This fact means that background subtraction is not required, although this would not have present any practical difficulty. Moreover, as can be seen in figure 5.26 (left), which shows the total number of counts above the pedestal of the single electron response of the PMT SN8928 versus the average background current and three more light levels, the contribution of the background is in fact

[11] These conditions are not strictly defined as the SER will have always a multiphotoelectron component. However, it can be made small in order to comply with the experimental requirements, for example, with if the whole detection probability $\sim 10\%$, the probability of one event originated from more than one photolectron is $\sim 0.5\%$.

negligible. In order to quote gains (and ENF) with an associated experimental uncertainty, the following two limit cases were considered: case a) just the fraction of the SER above the pedestal was considered; case b) the fraction of the SER close to the pedestal was linearly extrapolated towards the pedestal, and the whole events under the extrapolation were considered (a similar procedure is described in [56]). The procedure is exemplified in figure 5.26 (right). Using the results obtained from case a) and b) the gain and the ENF are quoted as the average of the two values and the experimental uncertainty given by the deviation of gains determined in a) and b) to the mean (see table 5.1). The detection probability was calculated for each PMT

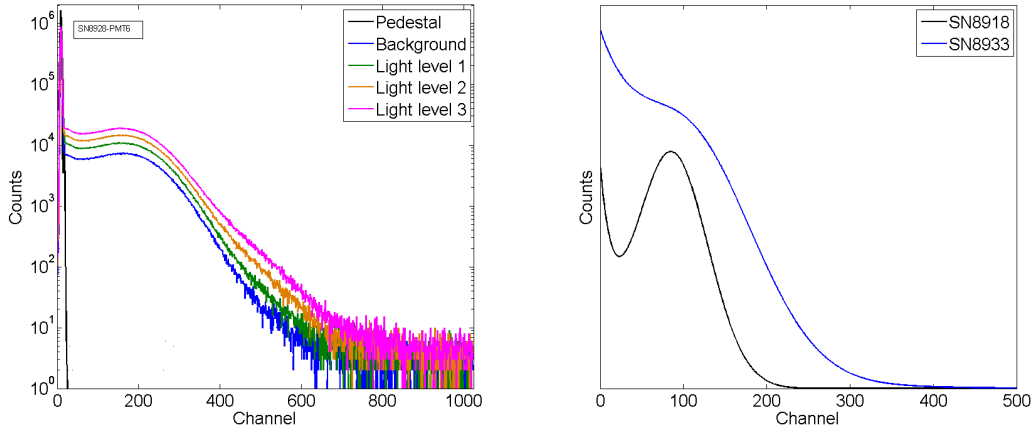

FIGURE 5.25: Left: Pedestal, background and three low light level PMT spectra. Right: Single electron response of two PMTs of the camera exemplifying the differences in single electron resolution capability among the camera photodetectors.

using charge histograms obtained under well known conditions i.e. light source position and number of photons emitted per pulse which allowed the number of photons hitting the window of each PMT to be calculated. From this data the number of photoelectrons was calculated using equation 5.13 and the individual values of the excess noise factor. The results are shown in table 5.1. The consistency of the PMT calibration and the measured values of $< G_{SER} >$ and ENF was checked experimentally noting that the mean gain can also be calculated from the charge histograms obtained in the workbench with high intensity light i.e. multiple photoelectrons are generated per light pulse, thus

$$< G_{Multi-Phe} >= \frac{Q}{N_{Phe} \cdot e} \tag{5.16}$$

where $< G_{Multi} >$ is the mean PMT gain (here with a $Multi - Phe$ subscript to distinguish from the value calculated from the SER), Q is the mean charge

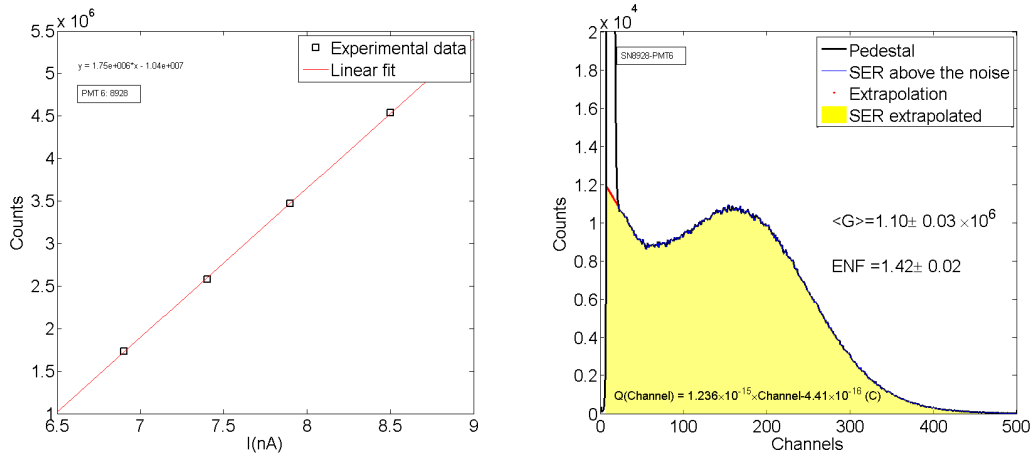

FIGURE 5.26: Left: PMT SN8918 current vs counts above the pedestal for each illumination level (see also 5.25 (left)). Right: Single electron response, integration limits and linear extrapolation used to determine the absolute gain of each PMT. The MCA calibration is given by the linear equation depicted at the bottom of the plot.

TABLE 5.1: Gain, ENF and detection probability of each PMT. The rightmost column shows the value of the conversion factor Phe/ADC_{Count} of each PMT readout channel.

Channel	PMT (SN)	$< G > (\times 10^6)$	$\Delta G\,(\%)$	ENF	$\Delta ENF\,(\%)$	DP	$\Delta DP\,(\%)$	Phe/ADC_{Count}
1	8920	0.79	7	1.45	4	0.15	18	3.9
2	8918	0.65	8	1.41	5	0.14	26	4.1
3	8933	0.82	7	1.51	5	0.21	24	3.7
4	8938	1.11	5	1.47	3	0.22	25	2.9
5	8932	0.57	8	1.50	5	0.19	29	5.3
6	8928	1.10	5	1.42	3	0.19	21	2.8
7	8921	1.18	5	1.43	3	0.14	17	2.8

(in units of Coulomb), N_{Phe} is the mean number of generated photoelectrons (see equation 5.13) and e is the electron charge. The comparison between $< G_{SER} >$ and $G_{Multi-Phe}$ is depicted in figure 5.27 for each PMT. The error bars of the $G_{Multi-Phe}$ data are mostly ruled by the uncertainty from the ENF and from the statistical uncertainty associated with the calculation of the number of photoelectrons from the PMT signal distributions (see equation 5.13). For all PMTs, the agreement between $< G_{SER} >$ and $G_{Multi-Phe}$ is inside the quoted uncertainty, assuring the consistency of the measured values of each quantity. It should be stressed that the calculation of the two values ($< G_{SER} >$ and $G_{Multi-Phe}$) are linked by the ENF and are therefore, not independent.

The detection probability was calculated for each PMT using equation 5.12 and they are shown in table 5.1. The uncertainty in $N_{Photons}$ and N_{Phe}

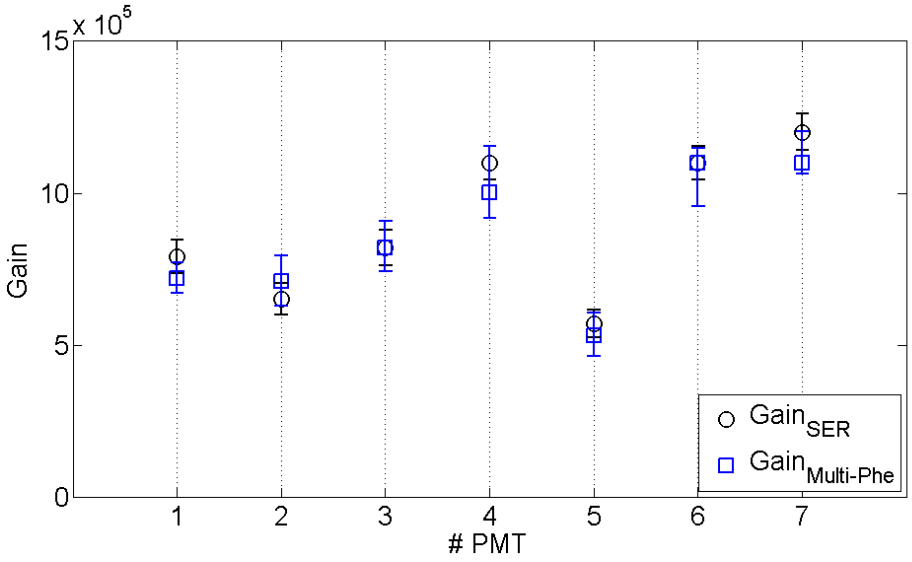

FIGURE 5.27: Consistency test: PMT gains measured under single photoelectron operation ($< G_{SER} >$) and multiple photoelectron operation ($< G_Q >$).

contributes most to the total uncertainty in the DP. The uncertainty in the determination of the number of photons hitting the photocathode is $\sim 5\,\%$ and for each PMT the uncertainty in N_{Phe} depends mostly on the uncertainty in ENF, G and the charge histogram statistics. The values obtained for the detection probability of the PMTs ranged from 0.14 to 0.22 (see table 5.1). The manufacturer quoted $QE(\lambda = 470\,\mathrm{nm}) = 0.16$ and assuming the value of 0.9 for the electron collection efficiency [55] gives an estimated nominal detection probability of 0.14 for this type of PMT, which is in reasonably good agreement with the measured DP and associated uncertainty. The conversion factor Phe/ADC, with units of photoelectron per ADC count, is also shown in table 5.1 for each readout channel. This conversion from ADC counts to photoelectrons is a required scaling e.g. with statistical event reconstruction algorithms that assume particular photoelectron distributions.

Chapter 6

The ANTS2 software

ANTS2 [6] is the successor of the simulation package ANTS (Anger-camera type Neutron detector: Toolkit for Simulation) [58] developed to optimize the design and operation conditions of secondary scintillation Anger-camera type gaseous detectors for thermal neutron imaging. ANTS was successfully applied for optimization of a position sensitive microstrip-based gaseous secondary scintillation detector with an array of PMTs [1]. However, it was limited to that type of detectors and just featured basic photon tracing capabilities. ANTS was superseded by ANTS2, which combined the possibility of simulating photon tracing on complex detector geometries with a set of interactive data processing, visualization and analysis tools in a convenient modular structure. Throughout this work, ANTS2 become the main simulation and data processing tool and for that reason only ANTS2 will be described here with emphasis being placed on those features relevant to this work.

6.1 Framework and implementation

The ANTS2 package is an open-source project implemented in C++ programming language using the multi-platform framework Qt[1]. The simulation module of ANTS2 is based on ROOT package from CERN [2], which is used to store the detector geometry and to perform 3D navigation.

6.2 Detector geometry

The detector geometry is built placing geometrical objects inside a predefined world object. The shape and position and material of each object can

[1] Qt ("cute") is a cross-platform application framework. See also `https://wiki.qt.io/About_Qt`.

[2] ROOT is a modular scientific software framework developed by CERN to deal with big data processing, statistical analysis, visualization and storage. See also `https://root.cern.ch/`.

be defined independently. The characteristics of the materials e.g optical and particle interaction properties can be either imported from an internal library or defined by the user. The photodetectors (PMTs or solid state detectors) are defined by their position, shape, dimensions and surface optical properties. Additional properties may also be defined to characterize the photoelectric conversion process, namely photon detection probability, gain, single photoelectron response and dark current.

6.3 Simulation module

6.3.1 Photon source

The photon source is point-like and isotropic. For wavelength-resolved simulations it is possible to assign a single wavelength to the generated photons or having it randomly selected from an user defined scintillation spectrum. The number of photons emitted during each event may be constant or randomly distributed over a uniform, normal or one distribution defined by the user. The emission of the photons occurs at a given source position (node), with several options available for the locations where the events are generated:

- Single node: all events are generated at a fixed source position;
- Custom nodes: the source positions are defined on an event-by-event basis;
- Node grid: the source positions are generated over a user defined regular grid of positions;
- Flood field: the source positions are randomly generated within predefined boundaries.

It is also possible to configure ANTS2 to perform a simulation run with a given number of events at each source position. In this case, the user can access a set of dedicated tools that provide statistical information about the generated events e.g. spatial or energy resolution.

6.3.2 Photon tracing

Photons are traced according to optical properties assigned to each material including refractive index, bulk absorption coefficient and Rayleigh scattering mean free path. By default ANTS2 uses Snell's law and Fresnell equations

to trace an optical photon at the boundary between two materials. However, photon tracing at certain material interfaces may be better described using a specific light scattering model. For that purpose, ANTS2 features several light scattering models that may be chosen by the user according to the characteristics of the optical interfaces.

A schematic representation of the photon tracing loop implemented in ANTS2 is depicted in figure 6.1. The photon tracing starts with a photon at

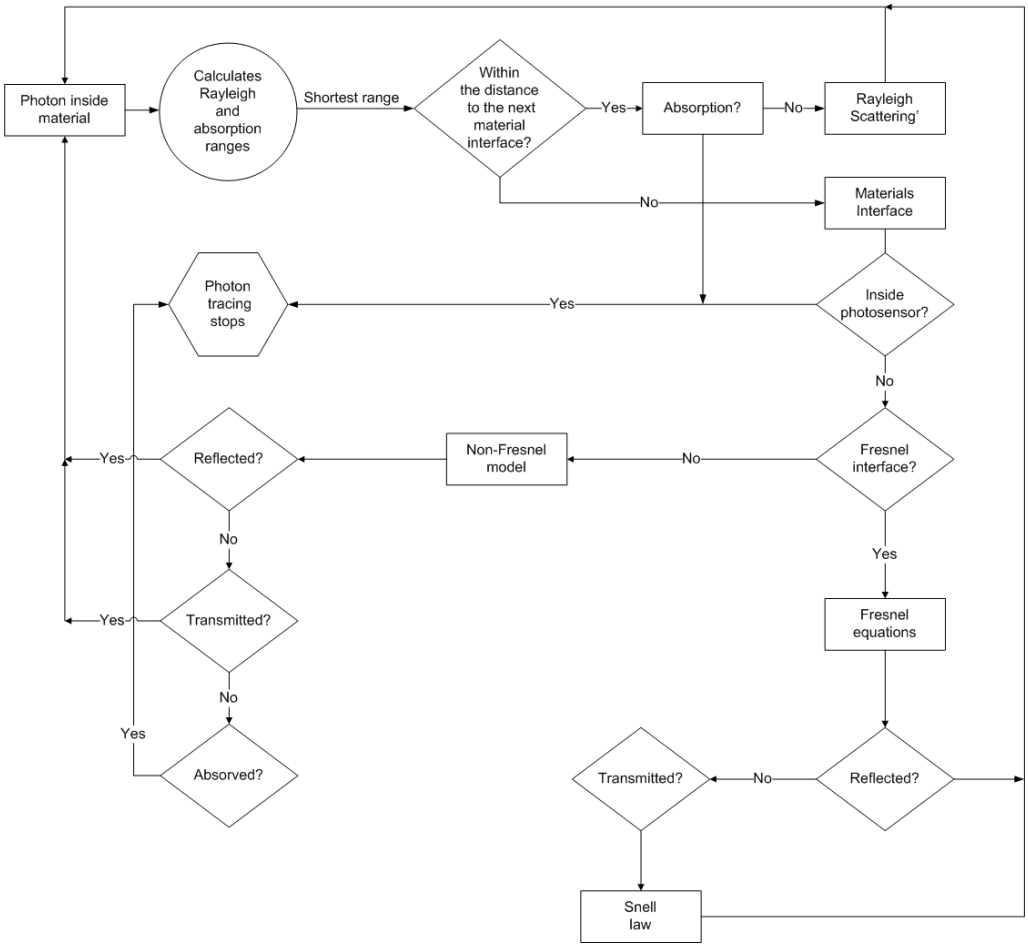

FIGURE 6.1: Flowchart of photon tracing in ANTS2.

some position inside a material of the detector. According to the photon direction and the optical properties of the material, the photon can be either absorbed (in this case the photon tracing stops), Rayleigh scattered or reach the interface boundary between two materials. If it is scattered, a new direction is assign to the photon and the tracing process returns to the starting point. By default, when the photon reaches the interface between two materials, is traced using the Fresnell equations for reflection and Snell law for refraction. However if the photon is inside a photodetector photon tracing stops and the process continues as explained in section 6.3.3. If the user selected

a particular non-Fresnel scattering model[3], the photon tracing proceeds according to that model. If the photon is either scattered or transmitted, the photon tracing returns to the starting point in the respective material. If the photon is absorbed the photon tracing stops. To avoid tracing photons out of the detector indefinitely and to speed up the simulation process, two additional conditions stop photon tracing (these are not shown in the fluxogram depicted in figure 6.1): if the photon leaves the detector geometry and if it reached the maximum number of allowed interactions (user defined).

6.3.3 Photon detection

A detailed model of the light detection by PMTs and semiconductor sensors is implemented in the package. For each sensor, the detection probability is calculated taking into account the following three factors:

- Quantum efficiency at the photon wavelength;
- Angle of incidence of the photon;
- Local photocathode anode sensitivity.

According to the detection probability, it is chosen whether a photon is detected or not using a random generator

6.3.4 Simulation output

After completion of a simulation, the PMT signals as well as positions and number of emitted photons can be saved in a ROOT Tree file or exported to a text file. The photodetector signal information can be accessed using ANTS2's GUI on an event-by-event basis. It is also possible to perform 3D visualization of the photon and particle tracks superimposed on the 3D plot of the detector geometry.

6.4 Reconstruction module

6.4.1 Data processing

In ANTS2, the data to process can either be inherited from the simulation or imported from a text file containing the photodetector signals. A preprocessing tool allows linear corrections to be performed on the imported

[3]Non-Fresnel optical interfaces cannot be described by Fresnel laws. Such surfaces are for example, a rough reflective surface.

data. This feature was used to subtract the pedestal in experimental data and to convert the signal from ADC counts to photoelectrons. It is also possible to reject events containing signals outside a predefined range (e.g. spurious zero ADC counts).

6.4.2 Reconstruction methods

The event reconstruction module calculates the spatial coordinates and energy of individual events using the photodetectors signals, assuming that light emission originates from a point source. This module can perform reconstruction for experimental or simulated data using one of several algorithms, including those already discussed in chapter 3 i.e. center of gravity, statistical methods and artificial neural networks.

6.5 Light response function module

Event reconstruction using statistical methods generally requires a mathematical model of the photodetector response which is represented by a set of light response functions (LRFs)[4]. In ANTS2 the LRFs are parameterized at a specific module using B-splines (the details of this parameterization scheme can be seen in [59]). The LRF module calculates these functions from data sets containing photodetector signals and the corresponding event positions measured or simulated over the detector area or volume.

6.5.1 2D LRFs

For planar position-sensitive detectors such as the one presented in reference [1], when only X and Y coordinates of an event have to be reconstructed it is often possible to ignore Z dependence of the LRFs. This type of parametrization scheme, when the LRF is a function of X and Y is designated in ANTS2 as "XY LRF". In some cases, the LRF has axial symmetry, allowing a reduction of the dependence of the LRF to just one variable - the distance between the event position and the photodetector center in the XY plane. In ANTS2 this parametrization is called "Axial LRF".

[4]The light response functions are described in chapter 3.

6.5.2 3D LRFs

Some detectors may require reconstruction of the light source position in three dimensions. There are two options available in ANTS2. The first option, "Axial+Z LRF", assumes that the LRF has an axial response in XY plane which varies along the Z direction. The second option is "Sliced LRF", in which the LRF is represented by a set of several XY LRFs, each defined on a specific Z plane.

6.6 Event filtering

The reconstruction module features a set of event filters which allow individual events to be filtered out according to several criteria, including signal values of individual sensors, sum signal of all sensors, reconstructed or loaded event energy, chi-squared value of the reconstruction, and the event position (true or reconstructed). These filters can be used to select events that occur at predefined positions or to discard events with large errors (e.g. events with large chi-square or unrealistic reconstructed energy or position).

6.7 Script mode

Although, as stated in the previous section, ANTS2 offers a set of tools to analyze data, often the user requires a way to proceed with a custom or more detailed analysis. In this case there are two available options, to export the data text file for further external processing or to use the ANTS2 script mode. This scripting tool allows to access virtually all variables and to perform custom analysis. Additionally it is possible to write scripts that configure and run iterations of mostly of the operations offered in the graphic user interface which allows to conveniently scan the detector performance through a set of different configurations.

Chapter 7

Experimental data processing and case studies

The performance of a position sensitive gaseous scintillation detector (PSGSD) depends on many parameters, including detector geometry and materials, number and wavelength of the photons emitted per detected event, photodetector properties, configuration and optical readout patterns, optical interfaces and event reconstruction algorithms. Since changing one parameter often requires modification of several others, the optimization process of a PSGSD is, in general, not straightforward and must be made iteratively. For this purpose, the emulation workbench can be of great help, as it is a reconfigurable system capable of providing realistic data at each set of experimental conditions under evaluation.

In this chapter, the results obtained with four different case studies addressing configurations commonly found in PSGSDs are presented. These studies allowed to evaluate the contribution of the characteristics of each particular configuration to the performance of the detector. In the first configuration (see figure 7.1) light scattering is highly suppressed since the walls of the light tight box and camera holder are painted with a low reflective black paint. As such, the majority of the detected photons did not experience any variation in direction between the moment they leave the surface of the light source and hit the window of a PMT. Under these conditions, the amount of light detected by each individual PMT is therefore relatively simple to model as it basically depends on geometrical parameters and the characteristics of the individual PMTs (described in detail in chapter 5). For this reason this minimalist configuration was chosen to check the consistency of results from the emulations workbench against a numerical simulation. The position reconstruction of the events was performed using the center of gravity algorithm (COG), which is the most often used method for detectors involving Anger-type readout due to its computational simplicity and robustness. The

light response functions of the individual PMTs (LRFs) were parameterized from experimental data and used to reconstruct the light source locations with the maximum likelihood algorithm. In some detectors there is the necessity to reconstruct the location of scintillation events in three dimensions. An example of 3D event reconstruction of a set of light source locations is given at the end of the chapter. The positions where estimated using the ML algorithm with light response functions parameterized from experimental data acquired with this minimalist configuration.

In the second configuration, a holder with an aluminized Mylar wall was added to the system. Aluminized Mylar has a strong specular reflectance, as it may occur for example in a detector with metallic inner walls, such as the one in reference [1]. For the third configuration, the aluminized Mylar was replaced by PTFE which is an highly reflective material being a nearly perfect Lambertian emitter. For these reasons PTFE is often used in PSGSDs to increase the performance of the detector by increasing the number of collected photons per detected event (see e.g. [60]). In both these cases (with Mylar and PTFE walls) the events were reconstructed with the maximum likelihood algorithm, as it takes advantage of the experimentally measured data to produce unbiased position and energy estimates. In the fourth configuration, the emulation workbench was fitted with a $10\,\mathrm{mm}$ thick glass window interfacing the PMTs and the light source. This configuration appears, for example, in the Helium-3 based neutron detector with an optical readout from reference [1].

Frequently the optical properties of the materials used to cover the inner non-photosensitive surfaces of detectors are not known in detail and must be independently measured to be used in simulation modeling of those detectors. The data acquired with the workbench can be used to estimate optical parameters of these materials by fitting data from a simulated model to the experimental data retrieved by the workbench. In this chapter two examples of parameter estimation using this technique are presented, namely the refraction index of the glass window and the parameters of a scattering model applied to PTFE.

7.1 Position reconstruction using the center of gravity algorithm

A sketch of the experimental system configuration is depicted in figure 7.1. The trajectories of photons emitted by an isotropic punctual light source lo-

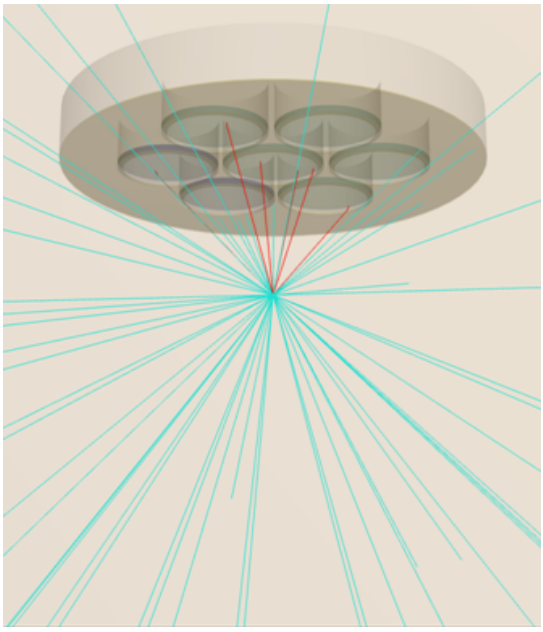

FIGURE 7.1: Sketch of the experimental system. The trajectories of the photons are represented by lines colored in red if the photons reach a PMT and in light blue for all other cases.

cated at (X, Y, Z) = (0 mm, 0 mm, 50 mm) are represented by lines colored in red if the photons reach a PMT and in light blue for all other cases.

The COG reconstruction of experimental data recorded over a circular, 50 mm diameter, regular grid of light source locations with $2.5\,\mathrm{mm} \times 2.5\,\mathrm{mm}$ grid spacing is depicted in figure 7.2 by black crosses. At each grid node, the distance between the light source and the PMT plane was varied between Z = 10 mm and 50 mm in steps of 5 mm and at each position the PMT signals were sampled by recording 500 events. The light source was set to emit an average number of $\sim 100 \times 10^3$ photons per pulse. The relative gains g were evaluated from the signal of each individual PMT recorded at the corresponding PMT axis position (X_{PMT}, Y_{PMT}) during the same acquisition. The average reconstructed light source locations, obtained with simulated data (see simulation details in appendix F), are also represented in figure 7.2 by a red dot and the "true" positions of the light source during the scan by a blue cross. The reconstructed light source locations exhibit the typical COG spatial distortions and are in good agreement with the results obtained using

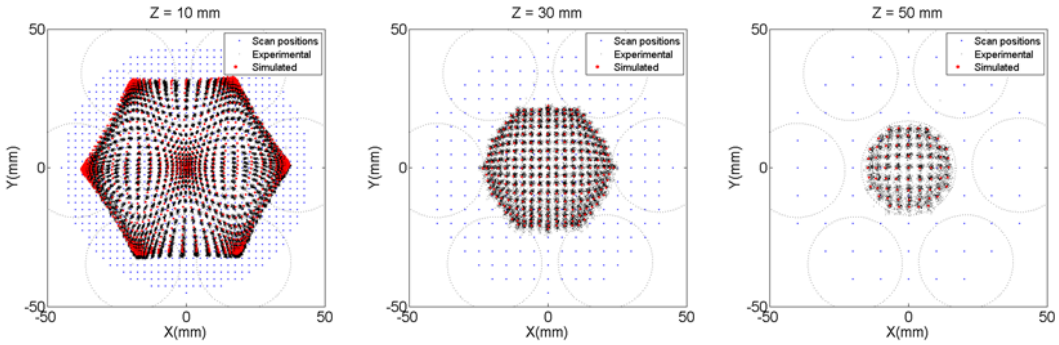

FIGURE 7.2: Simulation vs. experiment. COG reconstruction of events occurring at the nodes of a regular grid of positions at $Z = 10\,\mathrm{mm}, 30\,\mathrm{mm}$ and $50\,\mathrm{mm}$. The red circles correspond to the average reconstructed light source locations from simulated data. The grid step was increased for visualization purposes from $2.5\,\mathrm{mm}$ at $Z = 10\,\mathrm{mm}$ to $5\,\mathrm{mm}$ and $10\,\mathrm{mm}$ for $Z = 30\,\mathrm{mm}$ and $Z = 50\,\mathrm{mm}$ respectively.

simulated data. The good symmetry of the images suggest that both PMT relative gains and positions are well determined and that the light source is a good isotropic emitter. For $Z = 10\,\mathrm{mm}$, there is a relatively large deviation between the event positions reconstructed using simulated and experimental data. The outer locations reconstructed from simulated data tend to be deviated outwards relative to those from experimental data, which most probably occurs due to the individual characteristics of the PMTs such as angular dependence, which were not included in the simulated model. This result can be also seen in figure 7.3 where the X and Y coordinates of the reconstructed light source positions (from experimental and simulated data) are plotted versus the corresponding coordinates of the scanned positions.

The spatial resolution, defined in this work as the FWHM of the distribution of reconstructed positions at a fixed location, provides an estimation of how close the positions of two events can be and still be resolved from its reconstructed positions (see figure 7.4).

The spatial resolution mapped at the reconstructed light source locations is shown in figure 7.5 (X direction) and figure 7.6 (Y direction) along with the corresponding results obtained from simulated data. Along the X direction, the spatial resolution maps obtained from experimental and simulated data are in good agreement (see figure 7.5). However, along the Y direction the simulated model is not capable of fully reproduce the experimental data (see figure 7.5). The discrepancy is attributed to the incompleteness of the model used to simulated the PMTs which assumes e.g. uniform photocathodes and no angular dependence. This result is demonstrative of the capability of the emulation workbench to provide realistic experimental data, allowing this

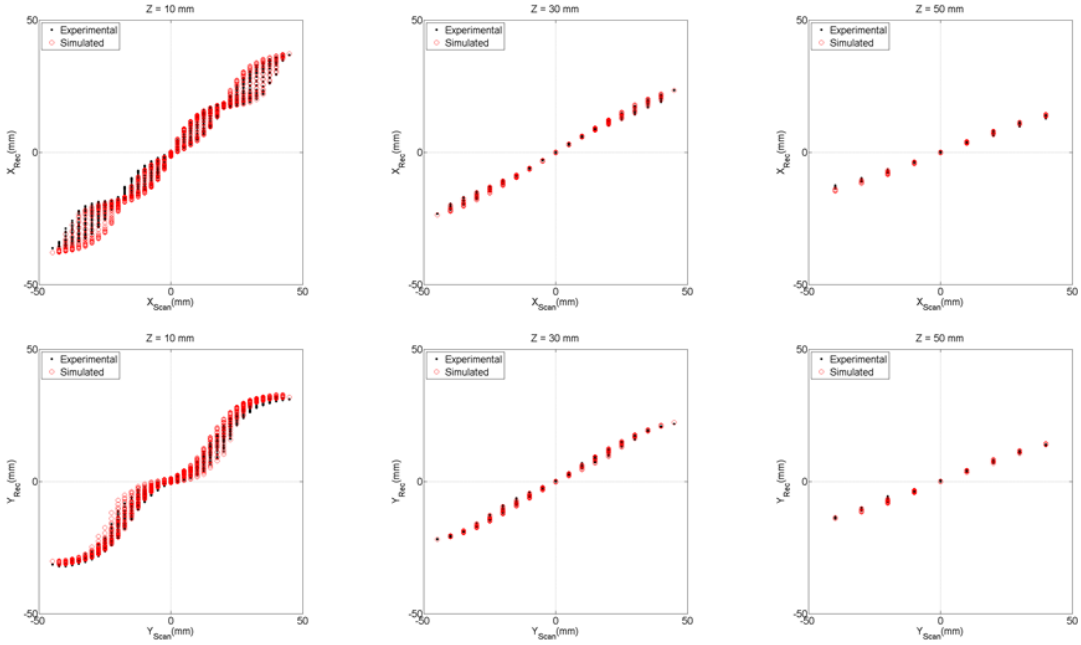

FIGURE 7.3: Reconstructed X and Y coordinates versus scan coordinates (black dots: from experimental data, red dots: from simulated data).

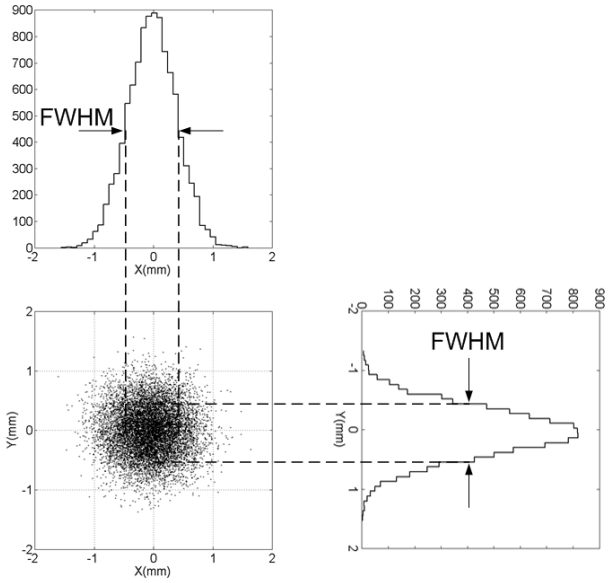

FIGURE 7.4: Distribution of reconstructed positions of events occurring at $(X = 0, Y = 0)$. The spatial resolution along the X and Y directions is given by the FWHM of the distribution of the reconstructed coordinates along that directions.

.

way to reveal features that otherwise would possibly be absent from simulated data relying in an model not including a detailed characterization of the PMTs.

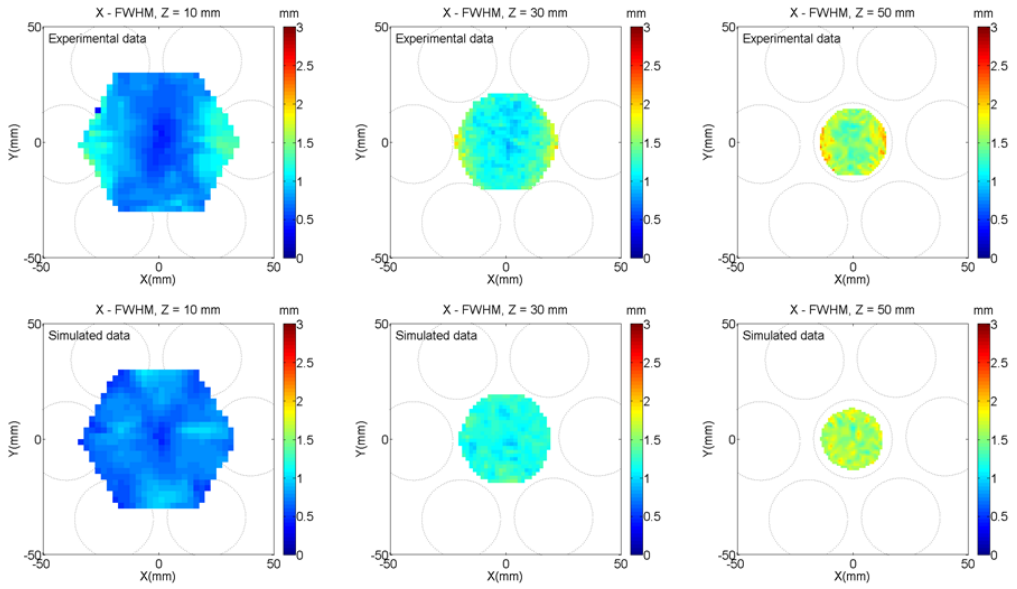

FIGURE 7.5: Spatial resolution along the X direction at the light source locations reconstructed with the COG at Z = 10 mm, 30 mm and 50 mm from experimental (upper row) and simulated data (bottom row).

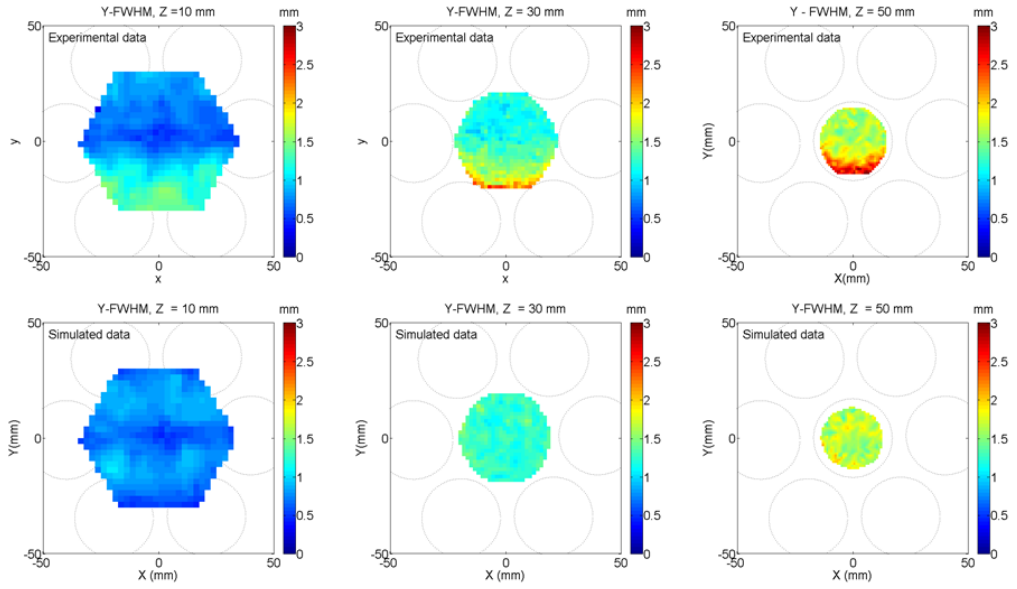

FIGURE 7.6: Spatial resolution along the Y direction at the light source locations reconstructed with the COG at Z = 10 mm, 30 mm and 50 mm from experimental (upper row) and simulated data (bottom row).

7.1.1 Spatial resolution vs. number of emitted photons

The variation of the spatial resolution of the reconstructed positions versus number of emitted photons per pulse in the range from 5×10^3 to 500×10^3 is shown in figure 7.7 measured at three test locations with Z = 30 mm. The experimental results practically match the simulation ones at all test locations.

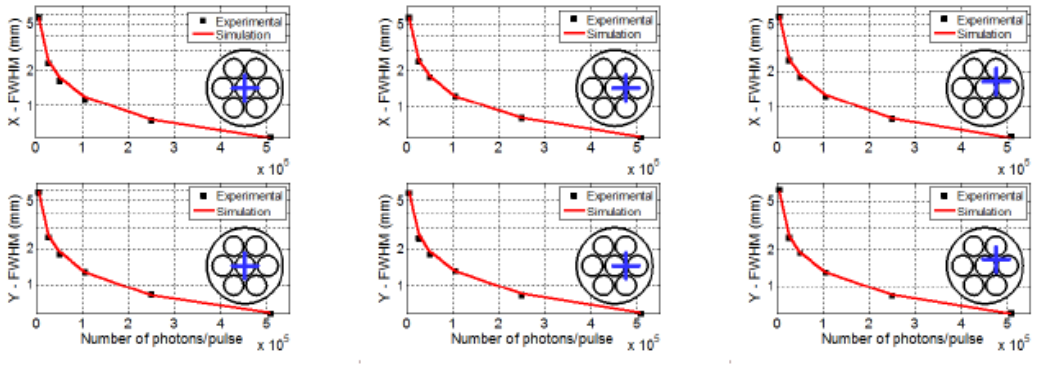

FIGURE 7.7: Simulation vs. experiment. Variation of the spatial resolution with the number of emitted photons per pulse. The position of the light source in the XY plane is shown by the blue cross inside the illustration of the PMT array.

7.1.2 Spatial resolution vs. distance

The variation of the spatial resolution versus the distance between the light source and the PMT plane was measured at three different source positions (using the same number of photons per pulse of $\sim 100 \times 10^3$). The results are shown in figure 7.8, demonstrating very good agreement between the simulation and the experimental data.

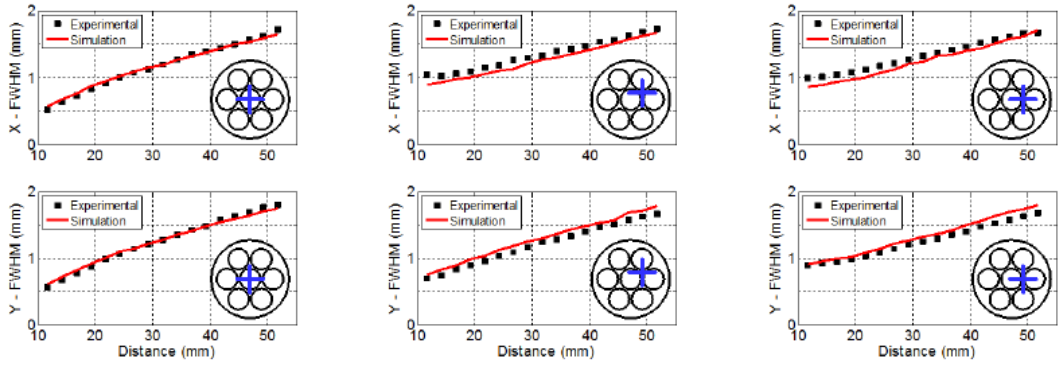

FIGURE 7.8: Simulation vs. experiment. Variation of the spatial resolution with the number of emitted photons per pulse. The position of the light source in the XY plane is shown by the blue cross inside the illustration of the PMT array.

.

7.2 Position reconstruction using the maximum likelihood algorithm

The center of gravity algorithm relies solely on the knowledge of the relative photodetector gains and positions. Assuming a linear dependence between the photodetector signals and the in-plane distance to the event position, it reconstructs the events location with large spatial distortions. This event reconstruction method works reasonably well close to the center of the detector but becomes increasingly biased for events in the periphery. If a mapping between the true event position and the reconstructed position exists, then it may be possible to obtain an unbiased estimate from the biased centroid with some post-processing method such as using a look up table.

Contrary to the COG, which does not take advantage of a detailed detector model (besides the relative gain and position of the photodetectors), the maximum likelihood position reconstruction algorithm takes full advantage of the experimentally measured LRFs. The information about any optical processes that may strongly affect the light collection such as light scattering or refraction are intrinsically contained in the LRFs. This may lead to several advantages of the ML over the COG such as better spatial resolution, potentially smaller distortions, larger useful field of view and better filtering of noise events. At the beginning of this section the results from a set of measurements, obtained under steady illumination conditions and suppressed light scattering are presented. The intention is to establish the experimental methodology developed to allow a fast assessment of the fundamental performance indicators of the camera namely, spatial linearity and resolution as well as intrinsic energy resolution and uniformity. Subsequently, this methodology is used to analyze the results obtained with different configurations namely with high diffuse (PTFE) and high specular (aluminized Mylar) scattering surfaces mounted in the system.

7.2.1 Parameterization of light response functions

To parameterize LRFs in ANTS2, one must define the type of LRF and the number of nodes to be used in the parameterization (following the nomenclature presented in reference [6]), i.e. control points where the B-splines will be anchored during the parametrization. The nodes are defined according to the dimensionality of the LRF, i.e. a radial LRF assumes an axial symmetric

response of the PMTs and the nodes are defined along the radial distance between the PMT position and the event location. In a XY-LRF the nodes are independently defined along the X and Y directions. The LRF parametrization module offers two node distribution schemes: uniform i.e. the distance between two successive nodes is constant or radial compression (available only for axial and polar LRFs) i.e. the density of nodes at smaller radial distances increases (where the variations on the LRF value occurs faster with distance). This compression scheme allows an improvement in the LRF parametrization in these regions, as slow varying sections require less nodes to be well described.

In the following sections several techniques that can be used to improve the quality of the LRF parametrization will be described, namely the acquisition of flood field illumination data and optimization schemes of the LRF B-spline parametrization.

Flood field illumination data

In the emulation workbench, flood field illumination is obtained operating the light source under steady conditions and recording the PMT signals at predefined light source locations. Random and regular light source location distribution schemes were considered. The random distribution of light source locations was made of randomly generated locations within predefined spatial boundaries. In order to minimize acquisition time the trajectory followed by the light source was optimized using the computer code Concorde[1]. Figure 7.9 (left) shows an example of a light source positions distribution made of 1235 random locations generated at constant Z within a radius of $50\,\mathrm{mm}$ from the center of the camera. The solid line connecting the locations indicates the path followed by the light source, including two control acquisitions[2] at the center of the camera i.e. $(X = 0, Y = 0)$. The regular distribution of positions consisted of a regular $2.5\,\mathrm{mm} \times 2.5\,\mathrm{mm}$ spaced grid of locations, centered at the camera with a radius of $50\,\mathrm{mm}$ also comprising 1235 nodes (see 7.9 (right)). It was seen that for the same number of locations used to produce the position resolved flood field, the XY-LRF parameterization obtained with a random distribution scheme was poorer than with a

[1]Concorde is a computer code for the symmetric travelling salesman problem (TSP) and some related network optimization problems. The code is written in the ANSI C programming language and it is available for academic research at http://www.math.uwaterloo.ca/tsp/concorde/index.html

[2]Control acquisitions consisted in acquiring data at the same location during the acquisition time in order to check the operational status of the system.

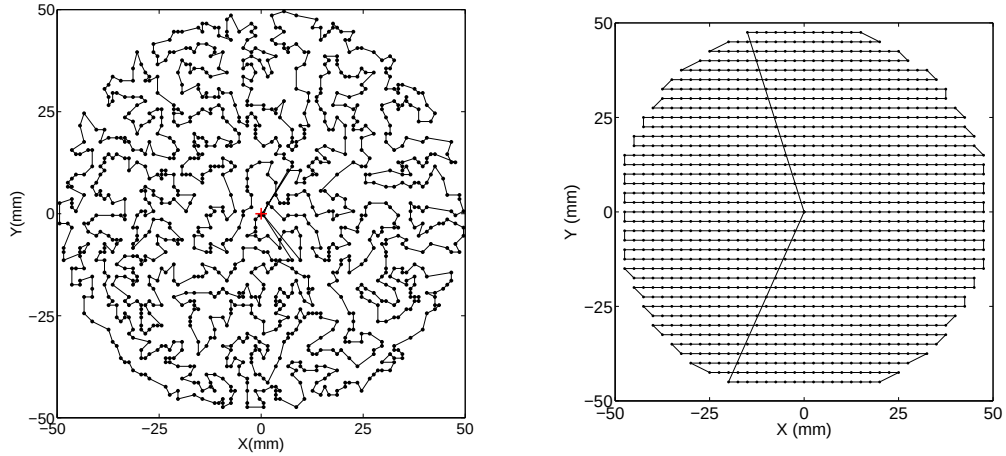

FIGURE 7.9: Left: Randomly generated 1235 light source positions at constant Z within $50\,\mathrm{mm}$ radius from the center of the camera. Right: Regular distribution of 1235 positions consisting of a regularly $2.5\,\mathrm{mm} \times 2.5\,\mathrm{mm}$ spaced grid of locations centered at the camera with a radius of $50\,\mathrm{mm}$.

regularly spaced grid of positions. This could be explained by the relatively large empty spaces occurring in the random distribution. Although it was trivial to increase the number of positions of the random distribution of positions, in practice the small velocity of the XY table ($0.5\,\mathrm{mm/s}$) meant that the required acquisition time would be very large and therefore the position distribution based on a regularly spaced grid of positions was considered as the best option for this work. The disadvantage of using a position re-

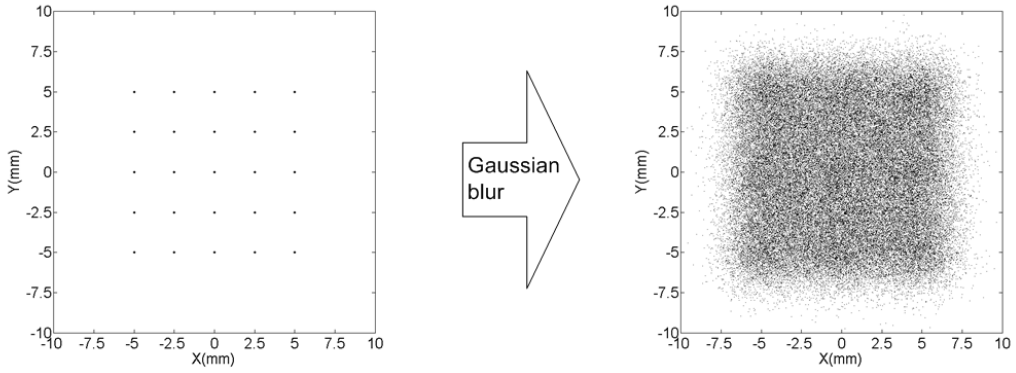

FIGURE 7.10: Effect of Gaussian blur with on the nodes of a regular $2.5\,\mathrm{mm} \times 2.5\,\mathrm{mm}$ spaced grid of locations. The Gaussian blur is centered at each grid node with $1.25\,\mathrm{mm}$ standard deviation.

solved food field measured from a regularly spaced grid of positions is that it may lead the XY-LRF parametrization process to produce inconsistent results within the boundaries of empty grid cells and subsequently the production of artifacts during position reconstruction. This problem can be sometimes

mitigated by blurring the position of each grid node before parametrization. Using this technique, the events are no longer confined to the grid nodes, but occupy also positions inside the empty cells of the regularly spaced grid. Since the LRFs are typically slow changing functions within the empty grid cells ($2.5\,\mathrm{mm} \times 2.5\,\mathrm{mm}$), this procedure does not introduce large errors. It was seen that for a regular grid of positions with $2.5\,\mathrm{mm}$ spacing, the standard deviation of roughly half grid spacing, i.e. $1.25\,\mathrm{mm}$, produced very good results as shown in the following sections where the LRF parameterization optimization procedures are discussed. In figure 7.10 the implementation of this procedure is shown for Gaussian blur centered at each grid position and $1.25\,\mathrm{mm}$ (half grid spacing) standard deviation.

Optimizing the LRF parametrization

The number of nodes n, used to parametrize the LRFs determine to some extent the quality of event reconstruction and therefore should be optimized. On one hand, the inter-nodal distance must be sufficiently small to accurately represent the PMT signal variation with distance; on the other hand, too many nodes may cause over-fitting and the production of artifacts in event reconstruction.

The optimization of the LRFs is done by varying the number of nodes and computing relevant quantities of the reconstructed data, which will act as an estimator of the parameterization quality, e.g. the average deviation from the reconstructed to the actual light source locations. An example is shown in figure 7.11, where the number of nodes of an axial LRF was increased from three up to twenty, while the average deviation of the reconstructed positions from the real positions was computed for each n. The LRFs were calculated from a flood field made from the PMT signals obtained at randomly distributed positions within a radius of $50\,\mathrm{mm}$ centered at the camera and contained in a plane parallel to the PMT's plane at $20\,\mathrm{mm}$ distance. The reconstructed data-set was made of signals obtained at 1860 positions composing the LIP-logo. As can be seen in figure 7.11 (left), for n $>$ 6 the average deviation is practically constant, and therefore n = 6 can be chosen as the optimum number of nodes to be used during the LRF parametrization, since a larger number of nodes adds computational complexity without a significant improvement of the quality of the position reconstruction. In figure 7.11 (right) the LRFs obtained for n = 3 and n = 6 nodes are compared, exhibiting the differences between the LRFs obtained from the same data-set but with different number of nodes. The reconstructed grid of positions is shown in figure 7.12 for the

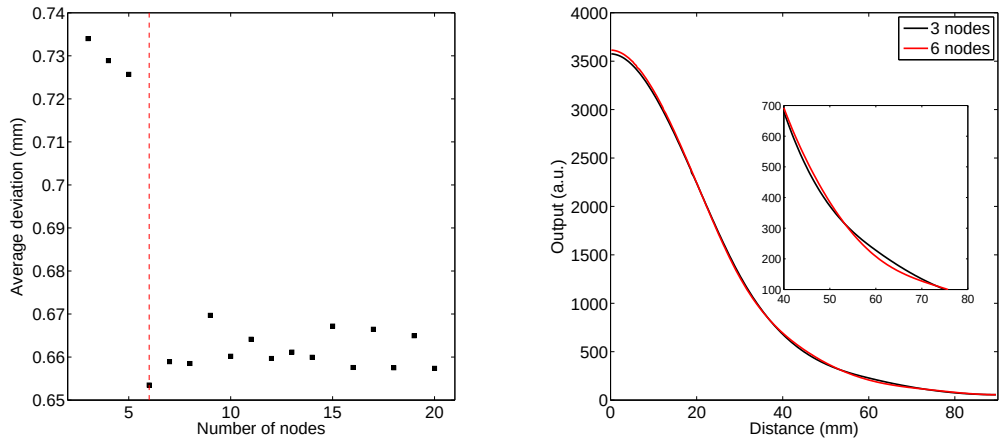

FIGURE 7.11: Left: Average deviation versus number of nodes used to parameterize the axial LRFs. Right: Comparison between the LRF parametrized with three nodes (black) and six nodes (red).

case $n = 3$ (left) and $n = 6$, color coded (right) for the average deviation.

As expected from the results shown in figure 7.11 (left), the quality of the reconstruction is better when made with LRFs parametrized with 6 nodes. As can be seen, from figure 7.12, the reconstruction still has relatively large

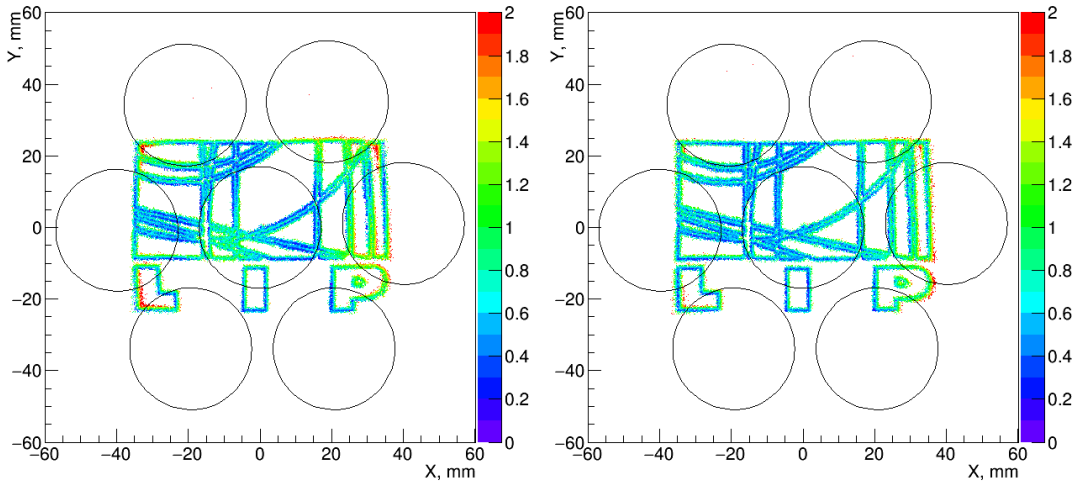

FIGURE 7.12: Reconstructed LIP-logo data with axial-LRFs parametrized with 3 nodes (left) and 6 nodes (right). The reconstructed positions are color coded for the deviation between the reconstructed position and the light source position. The average deviation of the reconstructions is $0.73\,\mathrm{mm}$ (left) and $0.65\,\mathrm{mm}$ (right).

distortions which indicate that axial symmetry may not fully model the detector response and therefore it may be required to use e.g. XY-LRFs. In figure 7.13 (left) the average deviation between the actual and reconstructed

light source locations is shown for a reconstruction made with XY-LRFs parametererized with a number of nodes along X and Y directions in the range between 3 and 20. The parameter used to evaluated the goodness of the parameterized XY-LRFs was the average deviation between the reconstructed and actual light source positions.

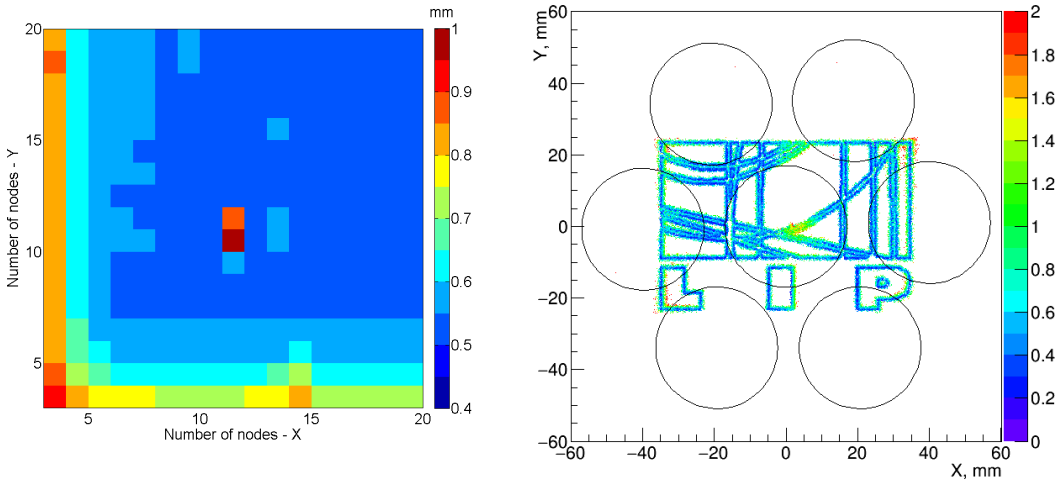

FIGURE 7.13: Left: Average deviation between the reconstructed and actual light source positions versus the number of nodes along X and Y directions used to parametrized the XY-LRFs (LIP-logo data). Right: Reconstructed positions from the LIP-logo data. The XY-LRFs were parametrized with 10 nodes along each direction. The average deviation of the reconstruction is $0.56\,\mathrm{mm}$.

As it can be seen in figure 7.13 (right), XY-LRFs perform significantly better than axial-LRFs (see figure 7.13). This result is expected since axial-LRFs by assuming axial symmetry (1D) may not be capable of providing a description of the spatial response of photodetectors as detailed as XY-LRFs (2D). The two main factors contributing to the absence of an axial symmetric response of the PMTs are the presence of scattered light and individual characteristics of photodetectors such as e.g. photocathode uniformity or angular dependence.

Experimental data processing methods

In the previous sections it was shown that it is possible to use experimental data measured at the nodes of a regularly spaced grid of positions to parametrize XY-LRFs that reliably model the detector. Moreover, as will be shown hereafter, it is possible to use the same experimental data to evaluate the overall performance of the camera, by recording a sufficiently high number of events at each grid position that, after reconstruction, will provide an

estimation of the camera performance at each grid node. It should be noted that using the same set of data, both to produce the LRFs and to evaluate camera performance may reduce the capability of the camera to reconstruct events occurring within the nodes of the cell, due to over-fitted LRFs. This may be avoided by using relatively small grid spacing, a small number of fitting nodes and applying blur to the grid positions. Based on these results, the LRF parametrization protocol was established as follows: first Gaussian blur with σ = 1.25 mm is applied to the grid data with 2.5 mm grid step. Then using an ANTS2 script we search iteratively for the number of LRF nodes that minimizes the average XY deviation between the actual light source positions and the corresponding reconstructed ones. Based on this procedure the LRFs are finally parametrized.

The reconstructed light source locations at the grid nodes are depicted in figure 7.14 (left) with each reconstructed event color coded for the deviation from the true light source position. The spatial resolution (FWHM) along the X direction at the center position i.e. $(X = 0, Y = 0)$ is $\sim$1 mm as it can be seen from the distribution of reconstructed positions at the center of the camera (see figure 7.14 (right)). The reconstruction is quite good, presenting

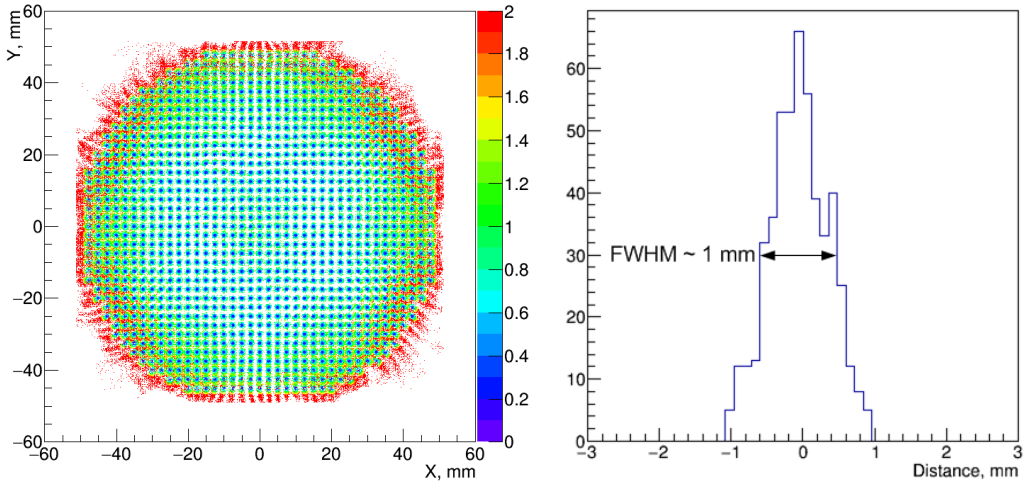

FIGURE 7.14: Left: 1 mm resolution FWHM - X.

very good linearity[3] and uniformity[4] within a radius of $\sim$ 40 mm (about the distance between the PMT centers) with an average deviation from the actual light source positions of $\sim$1 mm. Likewise calculating the resolution of

[3]If the relation between the true and reconstructed locations is linear, the reconstructed image has no distortions (however, depending on the slope of the linear relation it can be an enlarged or reduced version of the true image.

[4]In the present context, *uniformity* means that there are no local variations of spatial resolutions, distortions or unwanted artifacts.

the camera along the X and Y direction it is possible to map the resolution as depicted in figure 7.15. The event energy, i.e. the number of emitted pho-

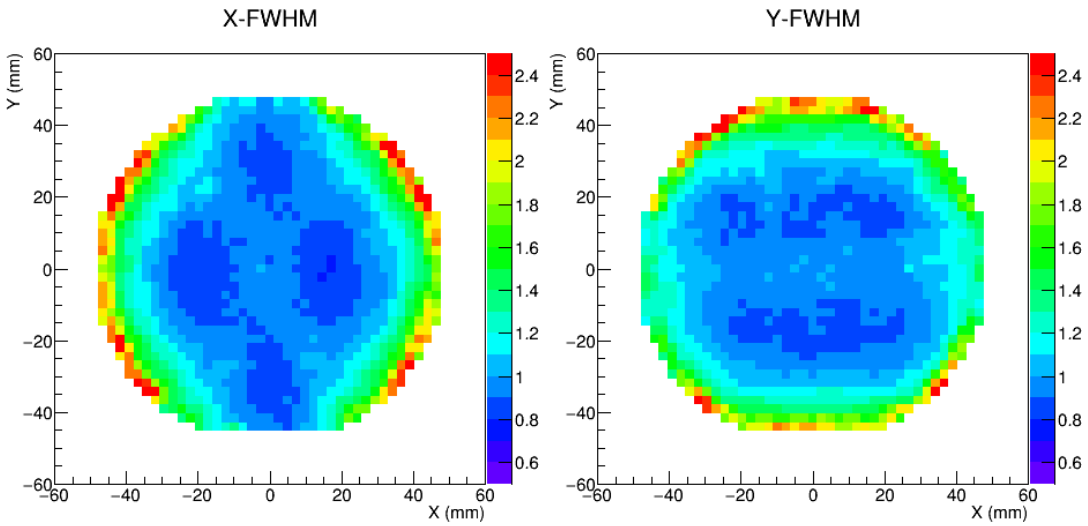

FIGURE 7.15: Spatial resolution (FWHM) at each grid node along the X (left) and Y (right) direction.

tons per event, is given in ANTS2 normalized to the energy value as calculated from the parameterized LRFs and the conversion factors between the measured PMT signals (in ADC counts) and the corresponding number of detected photons[5]. The energy of each event is shown in figure 7.16 where

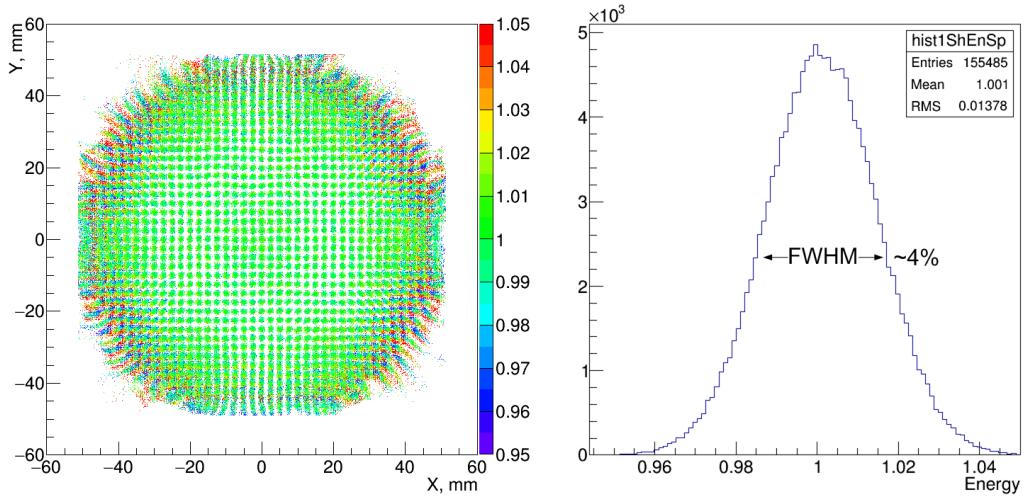

FIGURE 7.16: Left: Reconstructed event positions color coded for the reconstructed energy. Right: Reconstructed average energy distribution with $\sim 4\%$ FWHM.

the reconstructed positions of each event are color coded for the event energy

[5]These calibration factors are given in chapter 5.

exhibiting a good uniformity over an area within about a radius of $\sim 40\,\mathrm{mm}$ from the center of the camera. The energy distribution of all events within a radius of $40\,\mathrm{mm}$ from the center is approximately symmetric around the expectation energy value as can be seen in the histogram depicted in figure 7.16 (right). The FWHM of the energy histogram is about 4% which can be interpreted as the average intrinsic resolution of the camera (for this illumination conditions and within the considered area)[6].

7.2.2 Case study I: suppressed scattering

Under suppressed scattering conditions, the response of the individual PMTs of the camera is defined only by its intrinsic characteristics since scattered light is absent. In figure 7.17, the signal of the seven PMTs of the camera

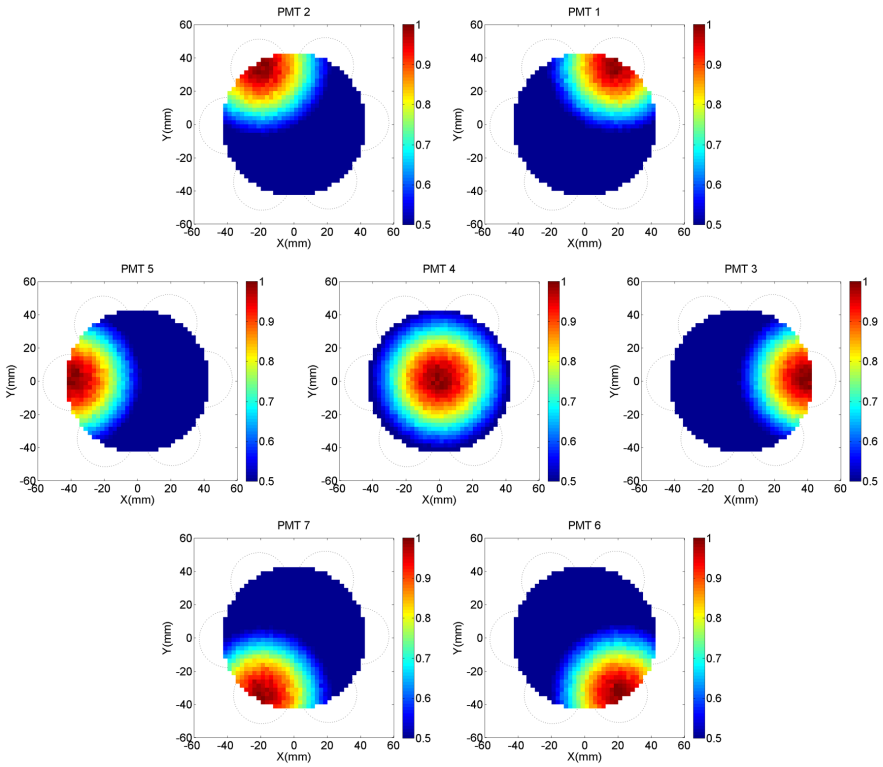

FIGURE 7.17: Effective signal of the PMTs measured over the XY plane at $Z = 50\,\mathrm{mm}$. The plots are arranged in the same hexagonal configuration as the PMTs in the camera.

is shown versus the light source position in the XY plane measured at $Z =$

[6]The light source is based on an LED that typically emits $\sim 10^6$ photons per pulse under these operation conditions. Consequently as the distribution of the number of emitted photons can be described to a very good approximation by a Poisson distribution having a FWHM of just $\sim$0.1% of the mean number of emitted photons [61].

$50\,\mathrm{mm}$. The light source emitted $\sim 250 \times 10^3$ photons per pulse and the measurements were made at the nodes of a regular grid of positions with $2.5\,\mathrm{mm}$ spacing. These results show that the response of all PMTs is approximately axial symmetric, suggesting a negligible contribution of scattered light to the PMT signal. The same symmetrical pattern was confirmed over the whole range of measurements from $Z = 10\,\mathrm{mm}$ to $Z = 50\,\mathrm{mm}$ in $5\,\mathrm{mm}$ steps.

The effective signal of each PMT was binned by the distance between the light source and the PMT axis and the average signal at each bin was calculated and normalized to the value at the center of the PMT. The results obtained at $Z = 10\,\mathrm{mm}$, $30\,\mathrm{mm}$ and $50\,\mathrm{mm}$ distance between the light source and the PMT plane are shown in figure 7.18. Superimposed on each PMT signal is the LRF calculated using just geometrical arguments, i.e. the LRF is a function of the solid angle subtended by the PMT window at the light source position. The overall agreement is good, but the simplistic geometri-

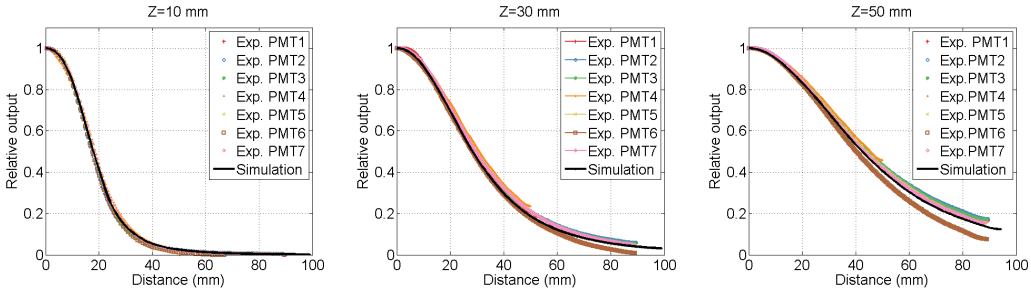

FIGURE 7.18: Light response function of the PMTs calculated from the experimentally measured data assuming axial symmetry. The black line represents the LRF calculated using just geometrical arguments i.e. the LRF is a function of the solid angle subtended by the PMT window at the light source position.

cal LRF calculation do not fully describe each individual PMT. There are signal deviations as large as $\sim 50\,\%$ between the average PMT signals at larger distances (see for example the LRFs calculated for $Z = 50\,\mathrm{mm}$ depicted in figure 7.18). The following three factors may contribute to these relatively large deviations: the intrinsic PMT characteristics, the light source anisotropy and the scattered light. Since the light-tight box has black painted walls and the distance from the PMTs to the box walls is relatively large, a negligible contribution of the scattered light to the signal of the PMTs is expected. This is corroborated by the axial symmetry exhibited by the PMTs depicted in figure 7.17. The light source anisotropy could also contribute to differences in the LRF shapes; however, it is very small and there was no evidence of such effects in other measurements e.g. the reconstructed event energy has high uniformity (see figure 7.16). It is therefore concluded that differences in the

intrinsic characteristics of each individual PMT are most probably responsible for the variation of LRF shapes presented in figure 7.18.

The reconstructed positions of the events are shown in figure 7.19 for Z = 10 mm, 30 mm and 50 mm. The XY LRFs were obtained according to the methodology described in section 7.2.1. For visualization purposes, the grid spacing was increased with increasing Z to avoid superposition of reconstructed positions as spatial resolution worsens. The position of the light

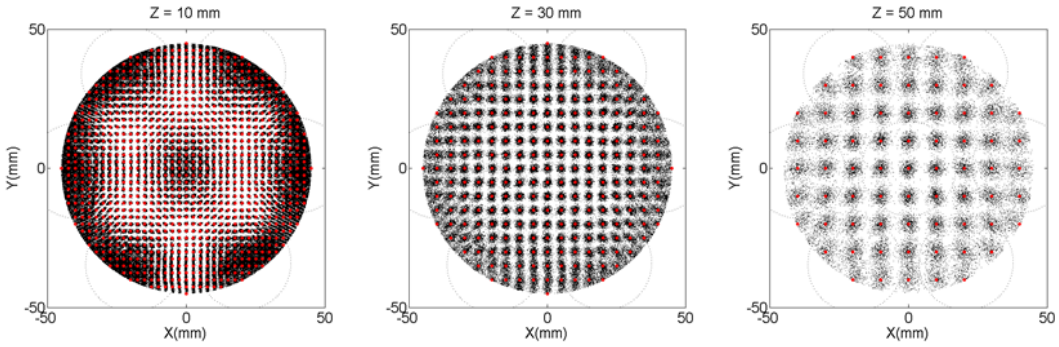

FIGURE 7.19: Reconstructed light source positions in the plane Z = 10 mm, 30 mm and 50 mm. The grid spacing was increased with increasing Z to avoid superposition of reconstructed positions as spatial resolution worsens. The position of the light source is indicated in each plot by the red circle superimposed on the reconstructed locations.

source is indicated in each plot of figure 7.19 by a red circle superimposed to the reconstructed locations. The distortions of the reconstructed image are shown in figure 7.20 depicting a color coded mapping of the deviation between the reconstructed coordinates and the actual light source coordinates Δ_X and Δ_Y with

$$\Delta_X = x_{Rec} - x_{LS}, \qquad \Delta_Y = y_{Rec} - y_{LS} \tag{7.1}$$

where (x_{Rec}, y_{Rec}) and (x_{LS} and y_{LS}) are respectively the reconstructed and actual light source locations. The orientation of the spatial distortion is defined by the sign of Δ_X and Δ_Y and relatively to the origin of the camera coordinate system. Accordingly to this definition, the spatial distortion is outwards if $\Delta_X > 0$ (or $\Delta_Y > 0$) and inwards for $\Delta_X < 0$ (or $\Delta_Y < 0$).

The light source positions are properly reconstructed in the whole range of recorded distances between the light source and the PMT plane (from Z = 10 mm to 50 mm, in steps of 5 mm), with the majority of the reconstructed events within ± 0.5 mm from the actual light source position. The distortion maps reveal non-symmetrical deviations of the reconstruction along X and Y directions e.g. for Z = 10 mm, locations with $X > 0$ show a tendency to

have positive deviation values, whereas for $X < 0$ the tendency is towards negative values, which means that there is an effective shift of the reconstructed locations towards $+X$. This type of bias results mostly from the LRF parametrization of PMTs with smaller gain at larger distances which are approximately flat curves with little information about the variation of the PMT signal with distance. It was seen that spatial distortion symmetry can be somewhat improved by increasing the number of nodes in the LRF parametrization.

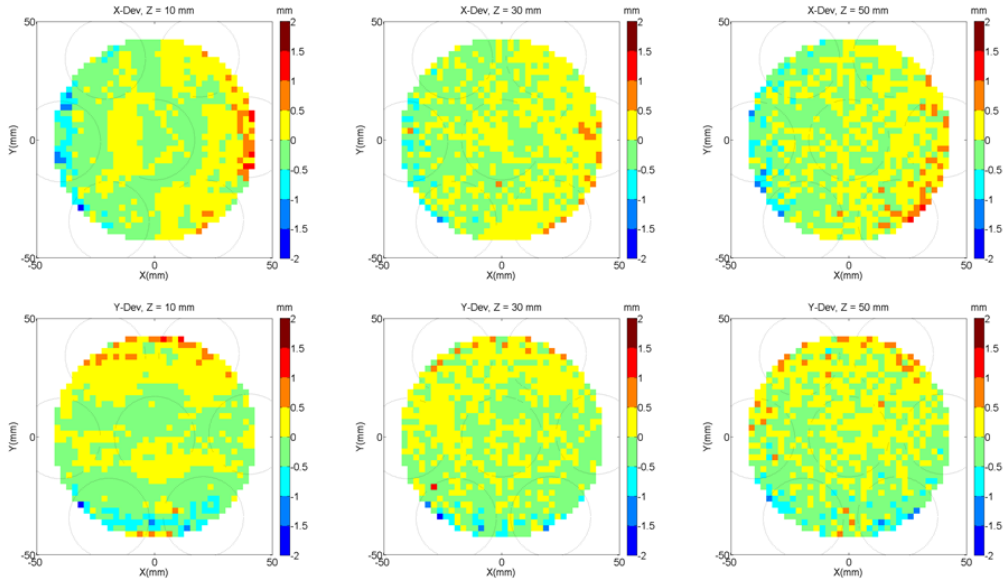

FIGURE 7.20: Average deviation between the actual and reconstructed light source positions measured at Z = 10 mm, 30 mm and 50 mm. The direction of the spatial distortion is relative to the origin of the camera coordinates system and is outwards for positive values and inwards for negative.

Resolution vs. distance

The spatial resolution along X and Y directions is shown in figure 7.21 plotted as a function of the distance between the light source and the PMT plane at three different locations in the plane XY. The results were compared with those obtained from simulations in ANTS2 considering the diameter and detection probability of the individual PMTs as well as the number of emitted photons per pulse ($\sim 100 \times 10^3$). There is an overall good agreement between the results obtained with both experimental and simulate data. However, while along the Y direction both simulation and experimental data have an excellent match over the whole Z range, along the X direction the agreement between the results from the two data sets is worse, particularly at larger Z

distances with the experimentally measured data set having a poorer spatial resolution than the results obtained from simulated data. This discrepancy is mostly explained by the combined effect of the intrinsic characteristics of the PMTs such as angular dependence and photocathode uniformity and the poor signal-to-noise ratio of some PMTs when the light source is at larger distances Z.

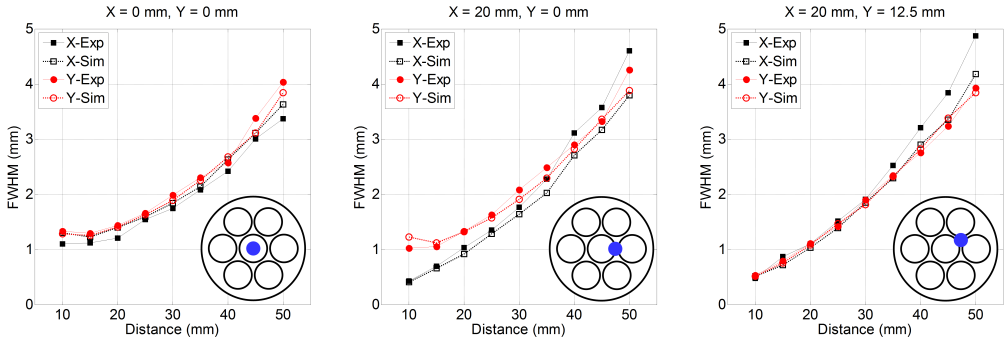

FIGURE 7.21: Simulation vs. experiment. Variation of the spatial resolution on the distance between the light source and the PMT plane. The corresponding light source location in the XY plane is shown by the blue circle inside the illustration of the PMT array.

The spatial resolution mappings along the X and Y directions are show in figure 7.22 for $Z = 10\,\mathrm{mm}$, $30\,\mathrm{mm}$ and $50\,\mathrm{mm}$. Along the whole Z range, the mappings exhibit the expected characteristic symmetry and there is an absence of noticeable artifacts. Both these facts are indicative of the consistency of operation of the system over the whole range of light source locations.

Energy reconstruction

As can be see in figure 7.23 the reconstructed event energy has, in general, good uniformity over the XY plane for $Z = 10\,\mathrm{mm}$, $30\,\mathrm{mm}$ and $50\,\mathrm{mm}$. This fact can also be seen from the event energy distributions shown in figure 7.23 (bottom row) which are, to a very good approximation, symmetric around the mean energy value. The variation of the energy resolution with distance is consistent with the values obtained using simulated data (see figure 7.23 (bottom row)). However, the energy resolution of the simulated data is about 16% better for $Z = 30$ and $50\,\mathrm{mm}$ whereas as for $Z = 10\,\mathrm{mm}$ it is worse by $7\,\%$. These differences, can be attributed to the intrinsic characteristics of the PMTs which are not taken into account in the simulations, in particular the angular dependence, which may explain why at $Z = 10\,\mathrm{mm}$ the energy resolution is better than the simulated model. In fact for small values of Z, the average angle of the photons hitting the PMTs is relatively large and typically the

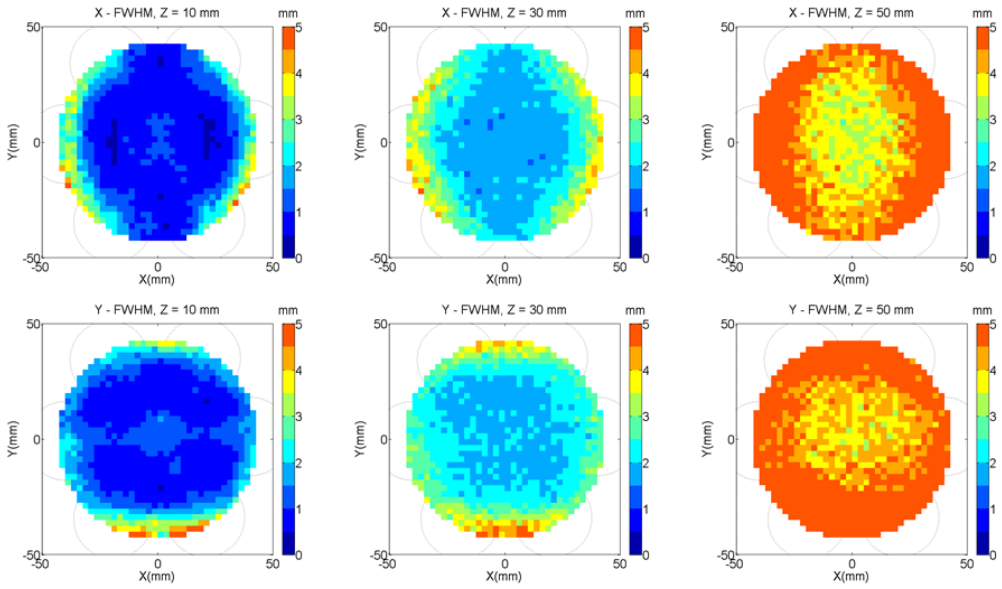

FIGURE 7.22: Spatial resolution mapped along the X (top row) and Y (bottom row) directions mapped at the distances between the light source and the PMT plane $Z = 10\,\mathrm{mm}$, $30\,\mathrm{mm}$ and $50\,\mathrm{mm}$.

PMT response increases somewhat at large angles (see for example figure 2.5 (right)).

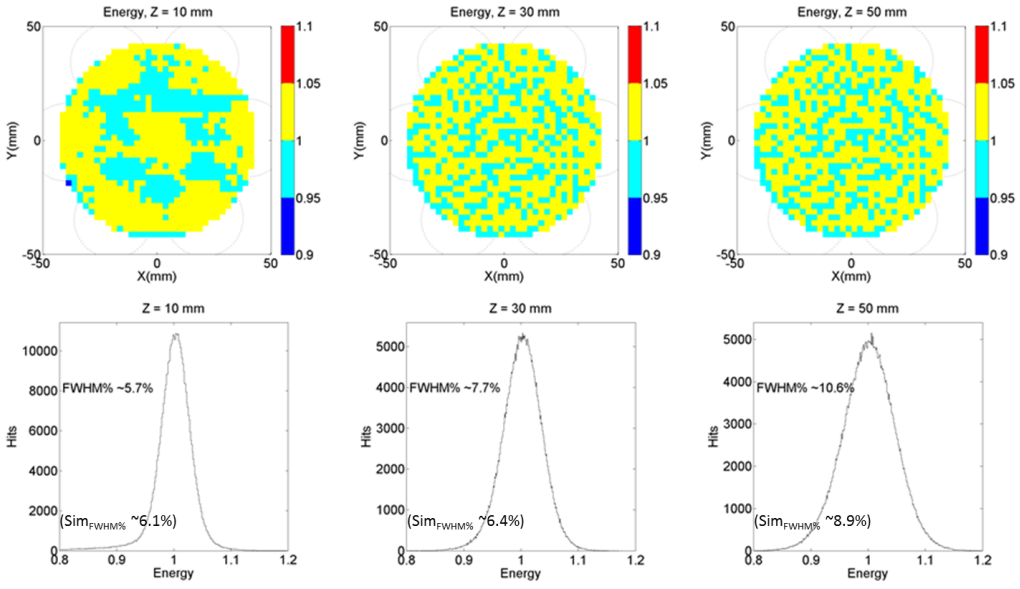

FIGURE 7.23: Reconstructed event energy within a field of view of $45\,\mathrm{mm}$ radius from the center of the camera (mapping (top) and distribution (bottom). The energy resolution is expressed as a percentage of full width at half maximum (FWHM%). In brackets, the values obtained with data from the simulated model.

7.2.3 Case study II: specular scattering

A sketch of the experimental system configuration is depicted in figure 7.24 with the cylindrical aluminized Mylar wall shown in orange. The trajectories

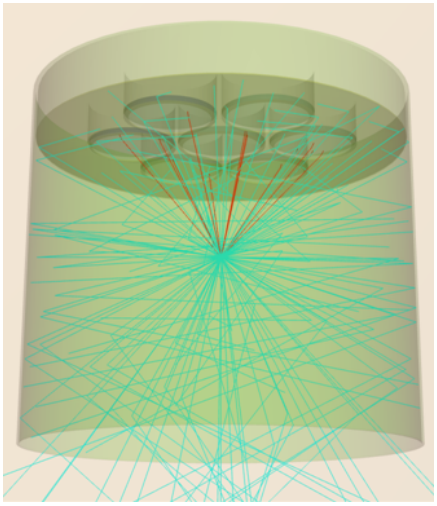

FIGURE 7.24: Sketch of the experimental system with a cylindrical aluminized Mylar wall (represented in orange). Photons emitted reaching the PMTs are depicted in red and in light blue for all other cases.

of photons emitted by the light source at (X, Y, Z) = (0 mm, 0 mm, 50 mm) are represented by straight lines (colored in red if they reach the PMTs and in light blue for all other cases).

The signal of PMT 4 and 3 is shown in figure 7.25 mapped at Z = 10, 30

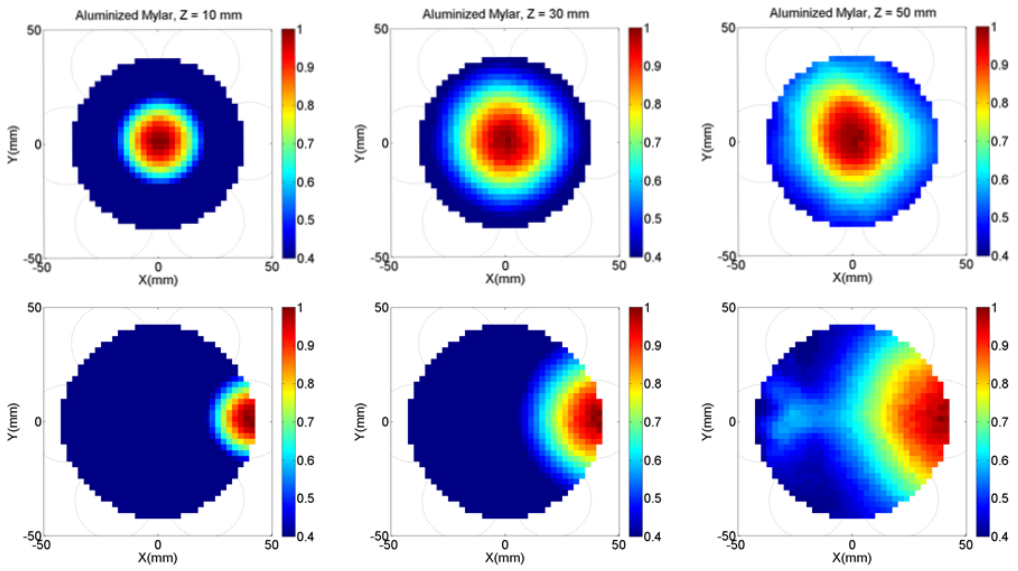

FIGURE 7.25: Mylar wall: Signal of the PMT 4 (top) and PMT 3 (bottom) mapped over a camera field of view with 45 mm radius at Z = 10 mm, 30 mm and 50 mm.

and 50 mm over a camera field of view with 45 mm radius. These results show

that as the distance between the light source and the PMT plane increases, the PMT signal at each location is originated from an increasingly larger portion of scattered light. For PMT 4, at the center of the camera, this results in a non-axial symmetric signal pattern, which is explained by the non-uniform surface of the aluminized Mylar wall (see figure 4.12 (right)). In the case of the peripheral PMTs (see figure 7.25 (bottom)), as the light source is placed farther from the camera plane, the signal mapping exhibits a well defined local maximum close to the corresponding opposing PMT (see e.g. PMT 3 for $Z = 50\,\mathrm{mm}$ in figure 7.25). At this particular geometrical configuration, a large fraction of the signal is generated from photons that are predominantly specularly scattered by the aluminized Mylar wall and consequently the light response functions of these PMTs are *degenerated* i.e. they have a local maximum not coincident with its global maximum.

The reconstructed locations on the planes $Z = 10$, 30 and $50\,\mathrm{mm}$ are shown in figure 7.26.

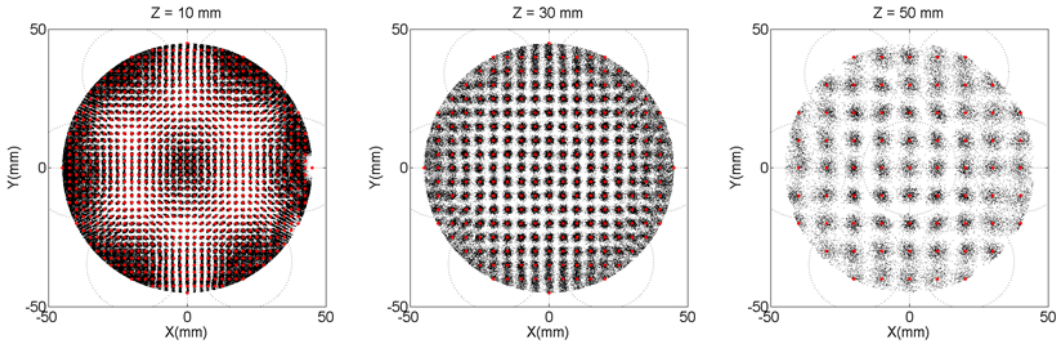

FIGURE 7.26: Mylar wall: Reconstructed light source positions in the plane $Z = 10\,\mathrm{mm}$, $30\,\mathrm{mm}$ and $50\,\mathrm{mm}$. The grid spacing was increased with increasing Z to avoid superposition of reconstructed positions as spatial resolution worsens. The position of the light source is indicated in each plot by the red circle superimposed on the reconstructed locations.

The pattern of light source locations was well reconstructed with no major spatial distortions or artifacts, as can be confirmed by the distortion maps shown in figure 7.27.

The spatial resolution of the reconstructed light source locations, is shown in see figure 7.28 following the same presentation procedure presented in section 7.2.2. Except for the center of the field of view, where the resolution is somewhat poorer, the overall pattern and values are similar to those found with suppressed scattered light conditions.

The average energy of the events calculated at each grid position is shown in figure 7.29 (top) for $Z = 10\,\mathrm{mm}$, $30\,\mathrm{mm}$ and $50\,\mathrm{mm}$. The corresponding energy distributions are shown in figure 7.29 (bottom). Due to the relatively

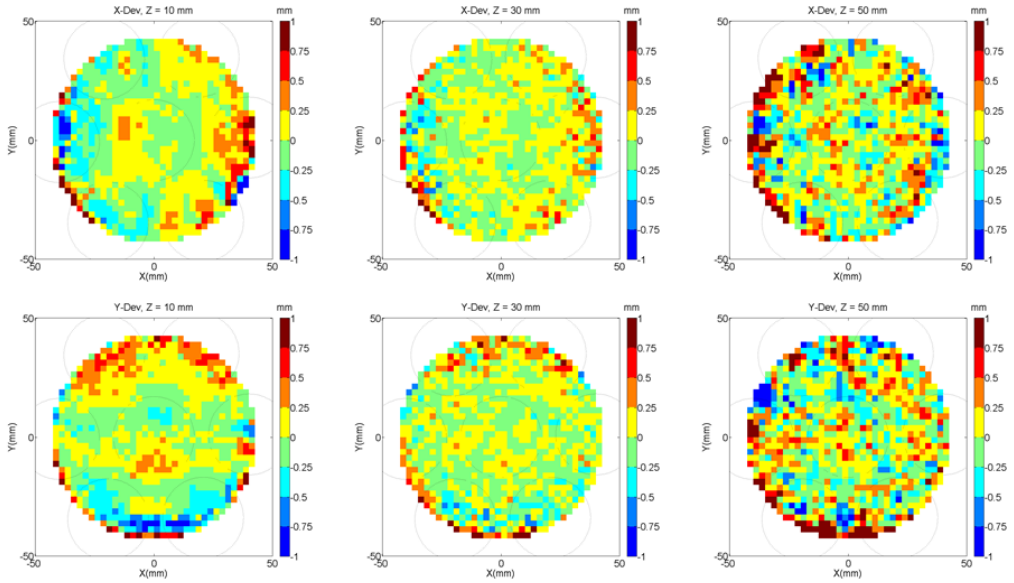

FIGURE 7.27: Mylar wall: Average deviation between the actual and reconstructed light source position measured at $Z = 10\,\mathrm{mm}$, $30\,\mathrm{mm}$ and $50\,\mathrm{mm}$. The direction of the spatial distortion is relative to the center of the axis of coordinates and is outwards for positive values and inwards for negative.

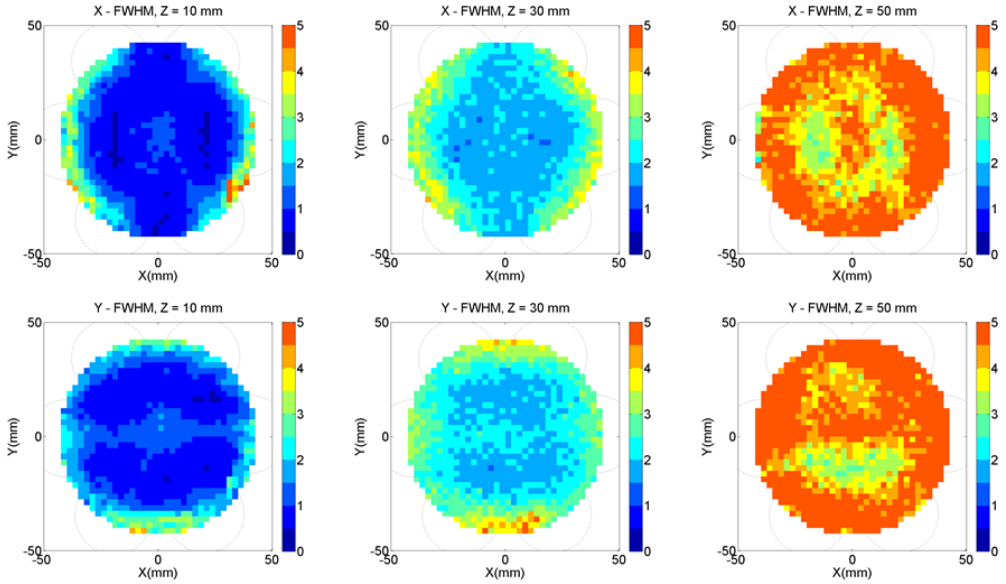

FIGURE 7.28: Mylar wall: Spatial resolution mapped along the X (top row) and Y (bottom row) directions mapped at the distances between the light source and the PMT plane $Z = 10\,\mathrm{mm}$, $30\,\mathrm{mm}$ and $50\,\mathrm{mm}$.

small amount of scattered light collected by the PMTs, when the light source is close to the camera plane (i.e. $Z = 10\,\mathrm{mm}$ and $Z = 30\,\mathrm{mm}$) there is practically no deviation in the energy values relatively to those found with suppressed scattered light. For $Z = 50\,\mathrm{mm}$ however, the energy resolution is $\sim 2\%$ better, which is explained by a larger amount of light being collected by the PMTs

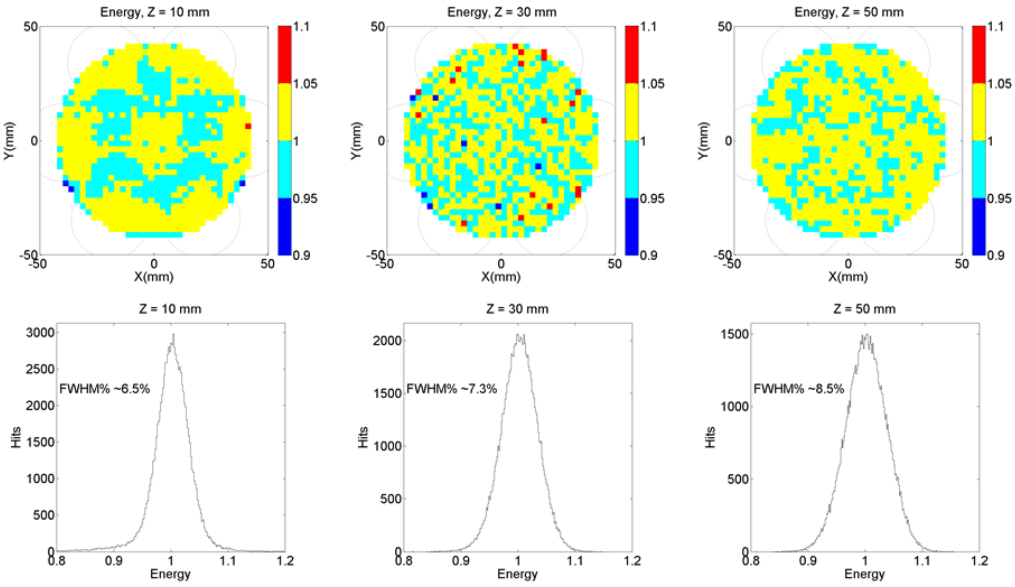

FIGURE 7.29: Mylar wall: Reconstructed energy within a field of view of $45\,\mathrm{mm}$ radius from the center of the camera (mapping (top) and distribution (bottom). The energy resolution is expressed in percent full width at half maximum (FWHM).

due to contribution of the scattered light.

With this example, it was shown that even in the presence of complex, non-uniform reflective surfaces the emulation workbench retrieve the required information to parameterize LRFs capable of correctly reconstruct events occurring inside the enclosure volume. In practice such situation may occur due, for example to the presence of irregular structures in the material of the walls or even due to variations of the reflection properties over the material surface (for example due to oxidation).

7.2.4 Case study III: diffuse scattering

A sketch of the experimental system configuration is depicted in figure 7.30 where the PTFE wall is shown colored in green. The photons from a scintillation event occurring at $(X, Y, Z) = (0\,\mathrm{mm}, 0\,\mathrm{mm}, 50\,\mathrm{mm})$ are represented by straight lines (colored in red if they reach the PMTs and in light blue for all other cases).

The signal of the central PMT mapped at the same experimental conditions of section 7.2.3 is approximately radial symmetric at all distances between the light source and the camera plane (see figure 7.31). The contribution of the scattered light to the signal of the PMTs is revealed in figure 7.31 by the relatively large signal of the central PMT over the whole mapping (in

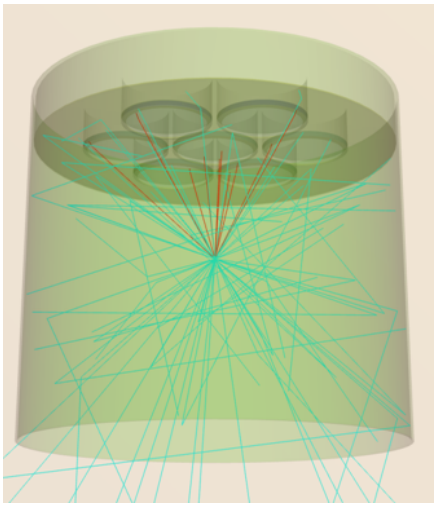

FIGURE 7.30: Sketch of the experimental system with a PTFE wall (represented in green). Photons emitted at $(X, Y, Z) = (10\,\mathrm{mm}, 30\,\mathrm{mm}$ and $50\,\mathrm{mm}$ are represented by straight lines (red if they reach they reach a PMT and light blue for all other cases.)

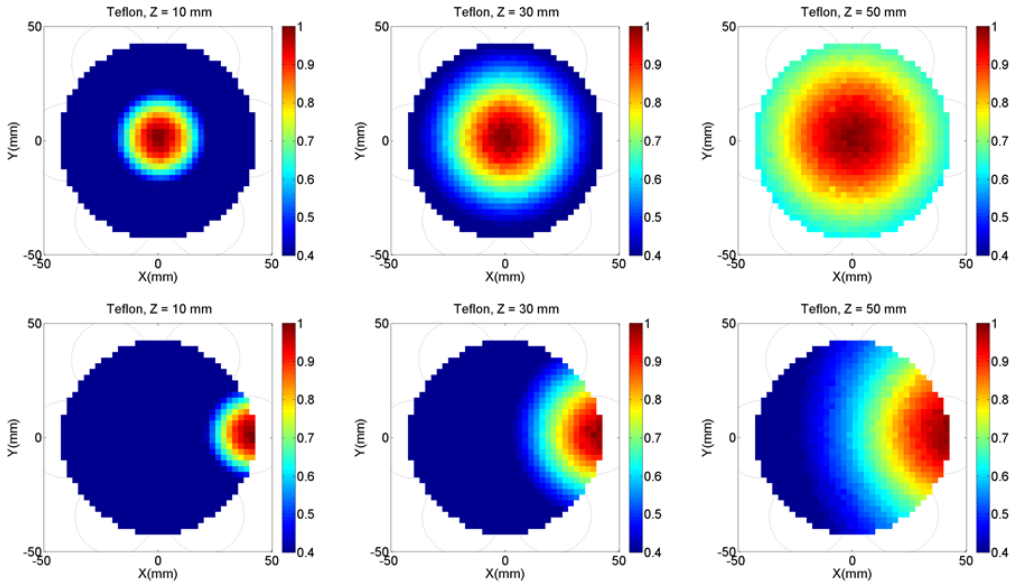

FIGURE 7.31: PTFE wall: Signal of the PMT 4 (top) and PMT 3 (bottom) mapped over a camera field of view with $45\,\mathrm{mm}$ radius at $Z = 10$, 30 and $50\,\mathrm{mm}$.

comparison with the suppressed scattering conditions) and by the slightly lack of radial symmetry of the peripheral PMT near to the PTFE wall (better seen for $Z = 50\,\mathrm{mm}$).

The light source locations were reconstructed very accurately (see figure 7.32), with no major distortions or artifacts as it can be confirmed from the corresponding average deviation mappings depicted in figure 7.33.

The spatial resolution of the reconstructed locations exhibited a similar pattern as in the previous cases and, as happened with the aluminized mylar

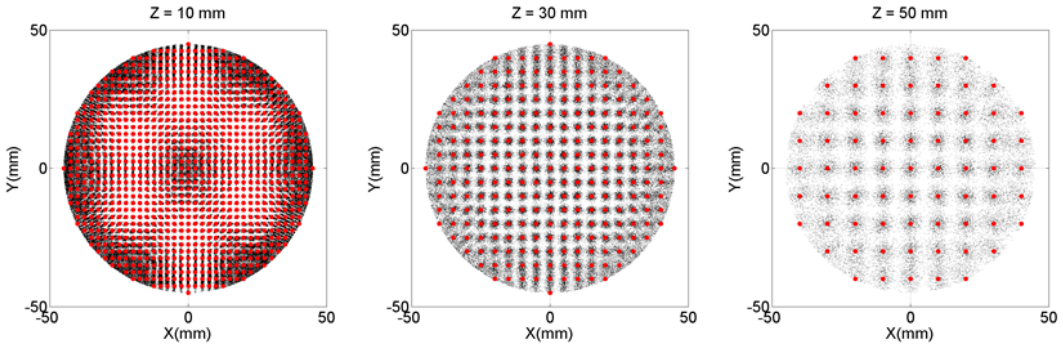

FIGURE 7.32: PTFE wall: Reconstructed light source positions in the plane Z = 10 mm, 30 mm and 50 mm. The grid spacing was increased with increasing Z to avoid superposition of reconstructed positions as spatial resolution worsens. The position of the light source is indicated in each plot by the red circle superimposed on the reconstructed locations.

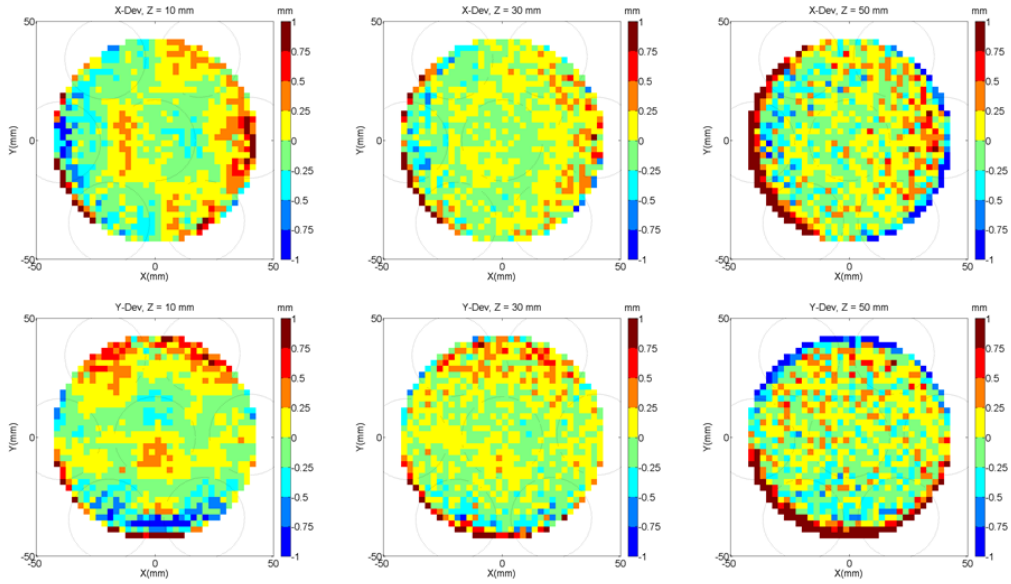

FIGURE 7.33: PTFE wall: Average deviation between the actual and reconstructed light source position measured at Z = 10 mm, 30 mm and 50 mm. The direction of the spatial distortion is relative to the center of the axis of coordinates and is outwards for positive values and inwards for negative.

walls, it is slightly degraded at the center of the camera field of view, when compared with the results obtained with suppressed scattering (see figure 7.34) .

For small Z, the mapping of the reconstructed energy (see figure 7.35) has a similar pattern as with suppressed scattering and aluminized Mylar wall and the overall uniformity is also very good. This is expected due to the relatively small fraction of collected light originated from photons scattered on the PTFE wall. As the distance between the light source and the camera increases the fraction of the signal due to scattered photons also increases

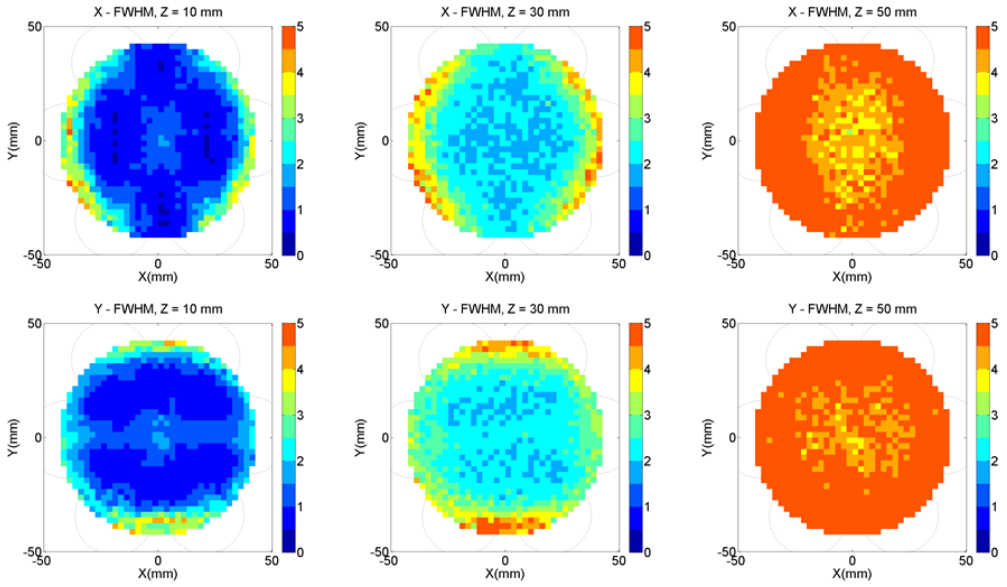

FIGURE 7.34: PTFE wall: Spatial resolution mapped along the X (top row) and Y (bottom row) directions mapped at the distances between the light source and the PMT plane Z = 10 mm, 30 mm and 50 mm.

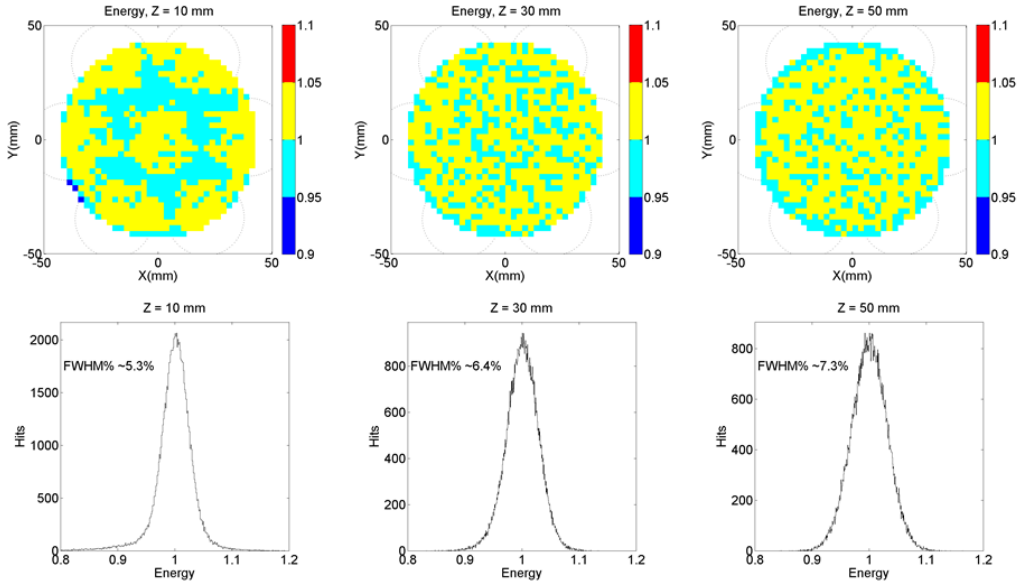

FIGURE 7.35: PTFE wall: Reconstructed energy within a field of view of 45 mm radius from the center of the camera (mapping (top) and distribution (bottom). The energy resolution is expressed as a percent full width at half maximum (FWHM%).

which can be seen comparing the FWHM% obtained with the PTFE wall at 50 mm (FWHM% = 7.3 %) with the FWHM% obtained with suppressed scattering (FWHM% = 10.6%). From the three cases presented above, the amount of light collected by the camera is the largest with the PTFE wall. This fact, is not unexpected since PTFE has very high diffuse reflectance resulting in a

larger amount of light being collected by the PMT array.

Parameterizing a light scattering model

In some scintillation detectors, high reflective materials such as PTFE are used to cover inner non-photosensitive surfaces in order to improve the detector performance by increasing the amount of collected scintillation light (see e.g. reference [60]). Frequently, the optical properties of these surfaces are not known in detail and must be measured to be included in e.g. Monte-Carlo simulations of the detector or experimental data analysis. In this section, a scattering model[7] is parametrized using the experimental data acquired with PTFE walls at a fixed distance Z = $50\,\mathrm{mm}$. The model assumes unpolarized light and that reflections are either specular or Lambertian, each weighted by the respective probability. The probability of specular reflection at the angle θ_i of incidence R_{Spec} is given by

$$R_{Spec}(\theta_i) = \frac{1}{2}\left(R_p(\theta_i) + R_s(\theta_i)\right) \tag{7.2}$$

where $R_p(\theta_i)$ and $R_s(\theta_i)$ represent, respectively, the probability of reflection for parallel (*p*) and perpendicular (*s*) polarized light as given by the Fresnel equations:

$$R_p(\theta_i) = \left(\frac{n^2 cos(\theta_i) - \sqrt{n^2 - sin^2\theta_i}}{n^2 cos(\theta_i) + \sqrt{n^2 - sin^2\theta_i}}\right)^2 \tag{7.3}$$

and

$$R_p(\theta_i) = \left(\frac{cos(\theta_i) - \sqrt{n^2 - sin^2\theta_i)}}{cos(\theta_i) + \sqrt{n^2 - sin^2\theta_i}}\right)^2 \tag{7.4}$$

with $n = n_{PTFE}/n_{Air}$ where n_{PTFE} and n_{Air} are respectively the refractive index of PTFE and air. The probability of light being backscattered from the surface (PTFE wall to air) will be referred here as the *albedo* and represented by A. If a photon enters the bulk, the probability of being scattered diffusely $R_{Diff}(\theta_i)$ is thus given by

$$R_{Diff}(\theta_i) = A\left[1 - R_{Spec(\theta_i)}\right] \tag{7.5}$$

where the albedo A represents the integral probability of the light being reflected at the PTFE. The quantity $1 - R_{Spec}\theta_i$ is the probability of light being refracted into the PTFE bulk volume. It is assumed that the direction of the

[7] An application of this scattering model is described in [62], where it was used to model the scattering of the scintillation light of liquid Xenon (emission peak at $178\,\mathrm{nm}$ wavelength) in PTFE in the context of the LZ experiment [2].

diffuse scattered light when exiting the surface of the material follows the Lambert cosine law, and therefore

$$dR_{Diff}(\theta_r|\theta_i) = R_{Diff}(\theta_i)\ cos(\theta_r)\ d\theta \tag{7.6}$$

where θ_r is the angle of reflection relative to the normal to the surface of the material.

The parametrization process is depicted schematically in figure 7.36. Flood-field experimental data (Exp data) is loaded in ANTS2 and the LRFs ($\mathrm{LRF_{Exp}}$) are parametrized. A program written using the scripting mode capabilities of ANTS2, runs a simulation of the camera (see simulation details in appendix F) with a set of initial values of the parameters to be optimized (in this case the refraction index of n and the albedo A). The program parametrizes the LRFs using the simulated flood field ($\mathrm{LRF_{Sim}}$) and iteratively looks for the set of values n_{PTFE} and A_{PTFE} that minimize the average deviation average deviation between $\mathrm{LRF_{Exp}}$ and $\mathrm{LRF_{Sim}}$. In the visible range, PTFE is to a very

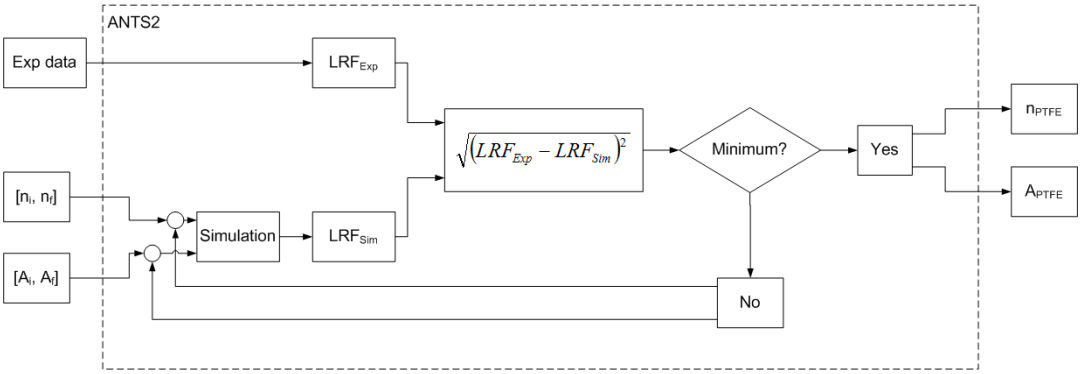

FIGURE 7.36: Schematic representation of the iterative parametrization of a scattering model.

good approximation a Lambertian reflector [63], with reflection coefficients as high as 99% [63] and refractive index around 1.3 [64]. Therefore, in order to reduce computing time the parameter A was bounded between to the interval [0.5, 1] and the refraction index of PTFE to the interval [1,1.5]. The XY-LRFs were calculated from a $45\,\mathrm{mm}$ radius flood field centered with the camera, and containing 10000 positions at Z = $50\,\mathrm{mm}$. The reason for using data measured at Z = $50\,\mathrm{mm}$ (the largest possible value for Z in the emulation workbench) is related to the fact that, on average, light detected from events occurring at this distance have the largest fraction of detected photons that were scattered in the PTFE walls. This fact can be seen in figure

7.37, depicting the average number of transitions[8] vs. distance Z. The LRFs

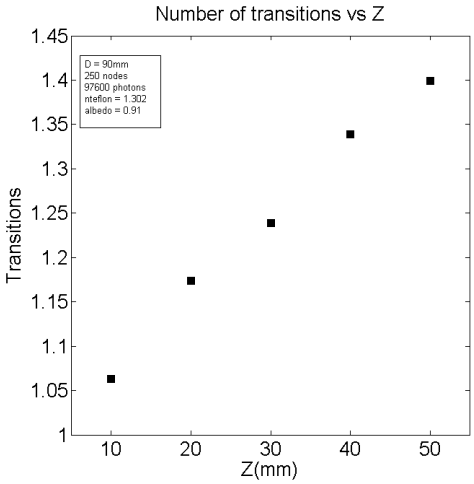

FIGURE 7.37: Average number of transitions vs Z.

were calculated considering 10 nodes along X and Y directions. The pair of values that minimized the mean square deviation were $A = 0.91$ and $n = 1.3$, which are close to the values found in literature for several grades of PTFE [64]. It should be noted however, that the thickness of the PTFE sheet was $\sim 2\,\mathrm{mm}$ and therefore some light is transmitted, probably contributing to a somewhat smaller value of A than those found in references [63] and [65]. In figure 7.38 (left), light source locations at Z=$50\,\mathrm{mm}$ are shown reconstructed using LRFs calculated from simulated data using the values found for n_{PTFE} and A. The reconstruction is reasonably good; nevertheless, some distortions are expected, as simulations do not account for differences in the response of individual PMTs, geometric irregularities of the PTFE walls and other details of the system not included in the simulation model (see simulation details in appendix F). To test the predicting power of the model using the values obtained for n_{PTFE} and A, the light emission plane on the simulation was changed from $Z = 50\,\mathrm{mm}$ to $Z = 30\,\mathrm{mm}$ and the light response functions of the detector were obtained from simulated data at $Z = 30\,\mathrm{mm}$. The results are shown in figure 7.38 (right). At $Z = 30\,\mathrm{mm}$ the light source locations are also reasonably well reconstructed, which contributes to the confidence on the robustness of the model.

[8]Transition is the number of interactions a photon undergo with some optical interface between emission and detection.

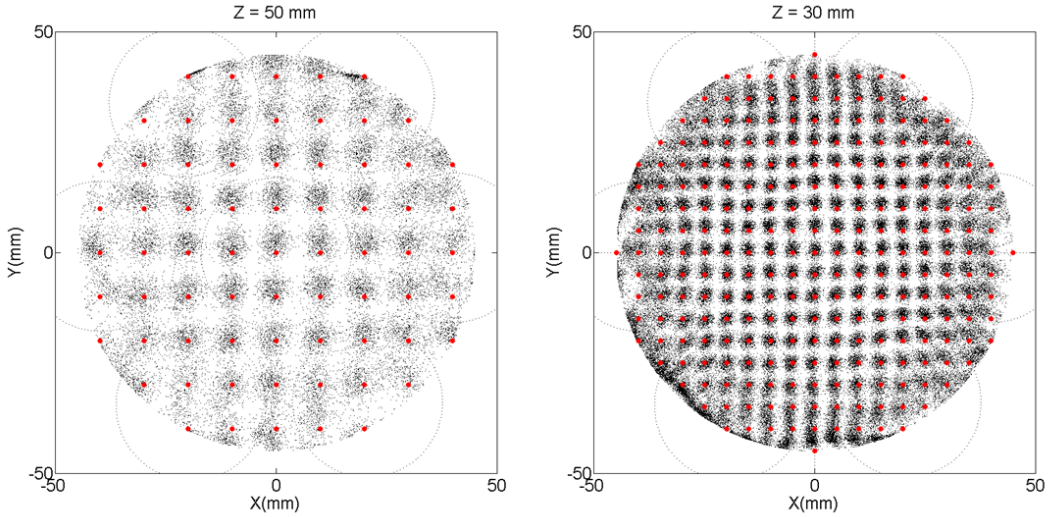

FIGURE 7.38: Left: Reconstructed light source locations without considering the PTFE wall. Right: Reconstructed light source locations using LRF calculated considering the PTFE walls and scattering.

7.2.5 Case study IV: Glass window

In PSGSDs, it is often convenient to place the photodetectors outside the gaseous scintillator and do the optical reading through a transparent (for the relevant wavelengths) *coupling window*. This is often the case with detectors with an optical readout based on PMTs since the glass envelopes may not withstand the gas pressure inside the detector. Furthermore, as gaseous helium permeates through glass, PMTs may become permanently damaged if placed inside an environment where helium is present (see e.g. reference [1]).

In general, the optical properties of the coupling window, such as light transmission coefficient and refractive index may contribute differently to the performance of a PSGSD. A light transmission coefficient different from 100% means that a fraction of the scintillation light will not be detected, whereas the relatively large refractive index of the window[9] means that light that otherwise would be not be detected will be refracted towards the photodetectors.

A sketch of the emulation workbench configured to investigate the effect of a glass window interfacing the gaseous scintillator and the optical readout is depicted in figure 7.39. The photons from an event occurring at (X, Y, Z) = ($0\,\mathrm{mm}$, $0\,\mathrm{mm}$, $50\,\mathrm{mm}$) are represented by straight lines (coloured in red if they reach the PMTs and in light blue for all other cases). A $10\,\mathrm{mm}$ thick, $80\,\mathrm{mm}$ diameter glass window was placed in contact with the holding mask

[9]The refractive index of gases is close to 1 whereas the refractive index of glass is typically around 1.5.

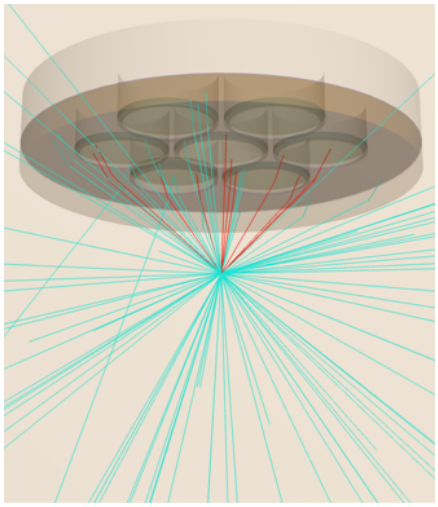

FIGURE 7.39: Sketch of the experimental system with a $10\,\mathrm{mm}$, $30\,\mathrm{mm}$ thick glass window (represented in green). Photons emitted at (X, Y, Z) = ($10\,\mathrm{mm}$, $30\,\mathrm{mm}$, $50\,\mathrm{mm}$) are represented by straight lines (red if they reach they reach a PMT and light blue for all other cases.)

of the camera. The air gap between the glass window and the PMT windows was $\sim 0.5\,\mathrm{mm}$. The thickness of the glass window and the distance between the light source and the PMT plane were chosen to enhance the effects of refraction on light collection. Operating the light source under the same conditions as in the previous examples, the signals of the PMTs were recorded at $Z = 20\,\mathrm{mm}$ along the same scanning track. The results are shown in figure 7.40 and 7.41. The overall spatial resolution of the reconstructed light source

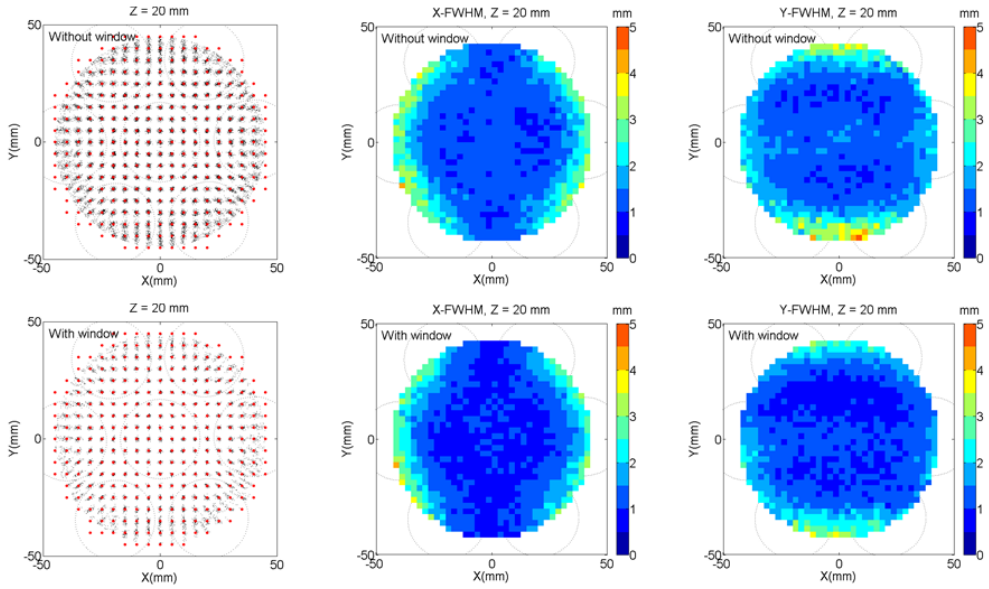

FIGURE 7.40: Reconstructed locations and spatial resolution maps along the X and Y direction without glass window (top) and with glass window (bottom).

locations is somewhat better when the glass window is on the system (see figure7.40). This is an expected result, since the glass window refracts light towards the PMTs that otherwise would not be detected. The energy resolution, which can be seen in figure 7.41, is approximately the same for both cases. This experimental data was used to estimate the refractive index of the

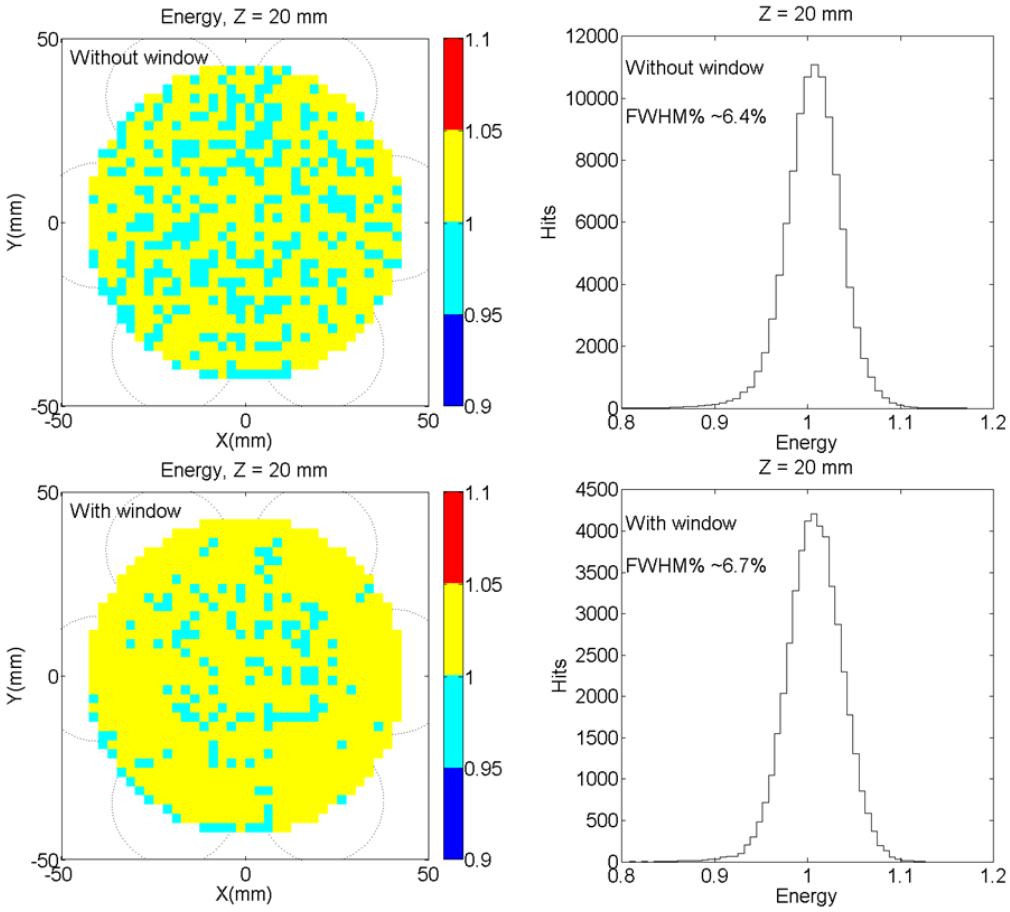

FIGURE 7.41: Reconstructed energy and energy resolution without glass window (top) and with glass window (bottom).

glass window through the same minimization procedure referred at the previous section, but in this case with the free parameter being the value of the refractive index of the glass. A value of $n_{Glass,Opt} = 1.48$ was found, which is in the range of the experimentally measured value of $n_{Glass,Exp} = 1.50 \pm 0.02$.

7.2.6 3D event reconstruction

In this example, light source locations are reconstructed in the three dimensions X, Y and Z. The 3D LRFs were obtained using a parametrization scheme available in ANTS2 under the designation "Axial + Z LRF", which assumes that the LRFs have axial response in the XY plane and an independent

variation along the Z direction. The experimental data set used in the LRF

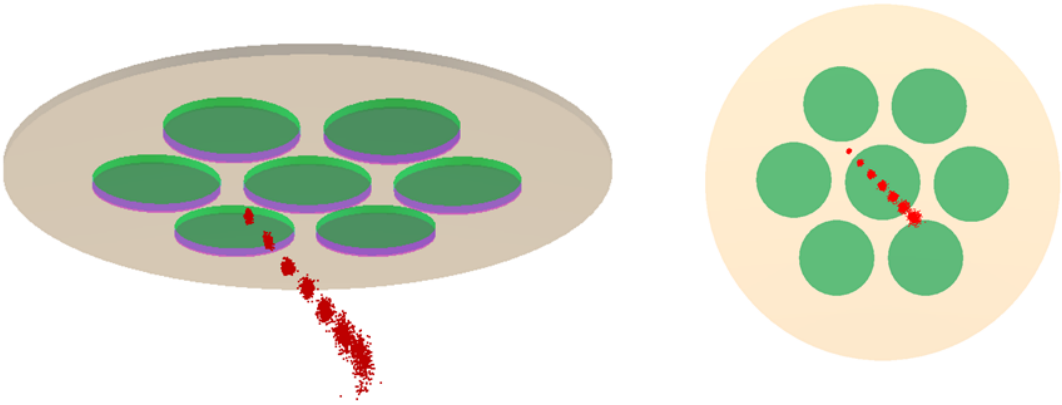

FIGURE 7.42: Reconstructed set of light source positions (left: perspective, right: bottom view).

parametrization consisted of a three dimensional regular grid of locations with $2.5\,\mathrm{mm}$ grid spacing along X and Y directions and $5\,\mathrm{mm}$ grid spacing along the Z direction. The pre-processing of the experimental data was done with the application of Gaussian blur to the light source positions, with standard deviation of $1.25\,\mathrm{mm}$ along X and Y and $2.5\,\mathrm{mm}$ along the Z direction. The light source locations shown reconstructed in figure 7.42 consisted of

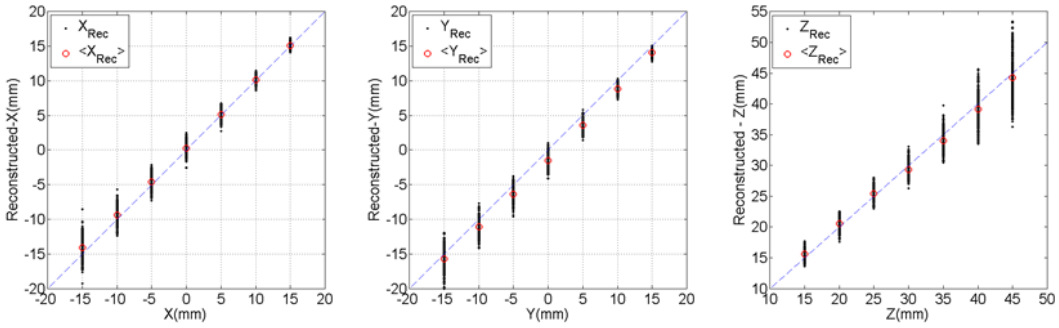

FIGURE 7.43: Reconstructed light source coordinates $(X_{Rec}, Y_{Rec}, Z_{Rec})$ versus the actual light source locations.

seven locations, in steps of $5\,\mathrm{mm}$ along (X, Y, Z), from a diagonal line with extremities at (X, Y, Z) = (-15, 15, 15) and and (X, Y, Z) = (15, -15, 45). For visualization purposes the reconstructed light source coordinates versus the actual light source locations are shown in figure 7.43. While the Z coordinate was reasonably well reconstructed, the locations in the XY plane are reconstructed with a bias along the Y direction by approximately $-1.5\,\mathrm{mm}$. Such spatial distortion is attributed to the over simplified description of the camera response, which is obtained by assuming PMTs with axial symmetric light response functions.

Conclusions

An experimental workbench for emulation of position sensitive gaseous scintillation proportional counters with Anger type readout has been developed and successfully tested under validation conditions with strongly suppressed scattered light. With this tool, point-like primary and secondary scintillation can be emulated with precise control of position, timing and intensity over a wide range of light intensities. Moreover, the system is configurable, allowing easy modification of geometry and materials of the walls, as well as type and arrangement of the photodetectors.
The results obtained in case studies covering several different detector geometries, with cylindrical walls built using materials with different light scattering properties, showed that this emulation workbench can be used to study and optimize the operation of detectors with different light scattering conditions. As scintillation light is physically emulated, intrinsic practical parameters such as spatial and energy resolution can be studied from the analysis of the detector output signals. As such, this method has the capability to produce realistic experimental data without a detailed characterization of the detector as often is the case with numerical simulations.

It was shown that optical properties of the detector surfaces (e.g. refractive index) can be estimated by fitting results from simulated photon tracing models to the detailed experimental data retrieved by this workbench. As scintillation can be emulated with precise control in position the validity of a such fitted model can be evaluated for a wide range of conditions.

Moreover, this concept can be used as a validation tool for simulations, to provide emulated realistic data to test readout electronics, to study the performance of event reconstruction algorithms or to develop adaptive techniques of the detector response such as those referred in reference [66]. It is envisaged that a similar system may be installed in some detectors for calibration or a performance evaluation purposes. The same concept can be further developed targeting applications requiring adjustable wavelength and precisely controlled time emission properties of the light source. This approach may eventually be extended to emulate light emission in liquid and solid scintillators by operating the light source in a volume filled with

a liquid with optical properties (e.g. refractive index) matching those of the scintillator in study.

Appendix A

PMT Hamamatsu R1387 datasheet

HAMAMATSU

PHOTOMULTIPLIER TUBE
R1387

300 to 850nm Response (S–20)
38mm(1–1/2 Inch) Diameter, 10–stage, Head–On Type

The configuration and basing diagram of the R1387 are identical with 6199 Photomultiplier tubes.

GENERAL

Parameter		Description/Value	Unit
Spectral Response		300 to 850	nm
Wavelength of Maximum Response		420	nm
Photocathode	Material	Multialkali	–
	Minimum Effective Area	34	mm dia.
Window Material		Borosilicate glass	–
Dynode	Structure	Circular–cage	–
	Number of Stages	10	–
Direct Interelectrode Capacitances	Anode to Last Dynode	3.0	pF
	Anode to All Other Electrodes	4.0	pF
Base		12–pin base JEDEC No.B12–43	–
Suitable Socket		E678–12A(supplied)	–
Weight		81	g

MAXIMUM RATINGS (Absolute Maximum Values)

Parameter		Value	Unit
Supply Voltage	Between Anode and Cathode	1250	Vdc
	Between Anode and Last Dynode	250	Vdc
Avarage Anode Current		0.2	mA
Ambient Temperature		-30 to +50	°C

CHARACTERISTICS (at 25°C)

Parameter		Min.	Typ.	Max.	Unit
Cathode Sensitivity	Luminous (2856K)	80	150	–	μA/lm
	Radiant at 420nm	–	64	–	mA/W
	Red/White Ratio (R–68)	–	0.2	–	–
Anode Sensitivity	Luminous (2856K)	10	50	–	A/lm
	Radiant at 420nm	–	2.1×10^{4}	–	A/W
Gain		–	3.3×10^{5}	–	–
Anode Dark Current (after 30min. storage in darkness)		–	4	25	nA
Time Response	Anode Pulse Rise Time	–	2.8	–	ns
	Electron Transit Time	–	40	–	ns

NOTE: Anode characteristics are measured with the voltage distribution ratio shown below.

VOLTAGE DISTRIBUTION RATIO AND SUPPLY VOLTAGE

Electrodes	K	Dy1	Dy2	Dy3	Dy4	Dy5	Dy6	Dy7	Dy8	Dy9	Dy10	P
Ratio	2	1	1	1	1	1	1	1	1	1	1	

Supply Voltage : 1000Vdc, K : Cathode, Dy : Dynode, P : Anode

PHOTOMULTIPLIER TUBE R1387

Figure 1: Typical Spectral Response

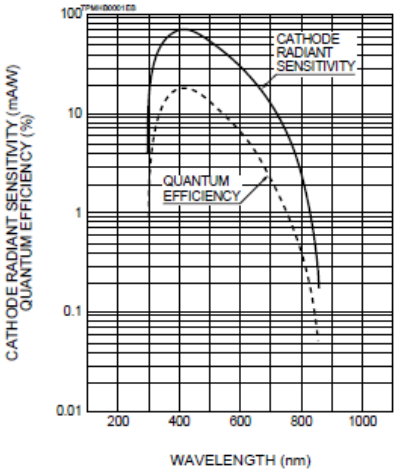

Figure 2: Typical Gain

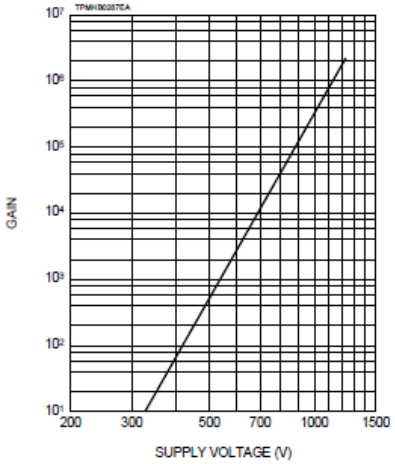

Figure 3: Dimensional Outline and Basing Diagram (Unit: mm)

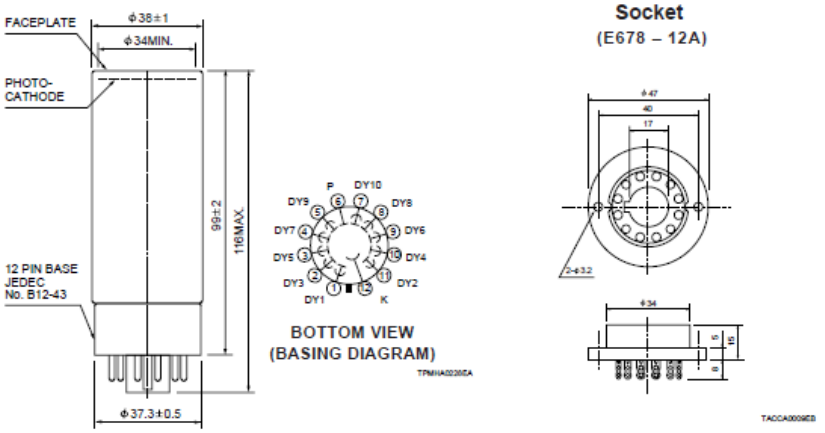

HAMAMATSU HOMEPAGE URL http://www.hamamatsu.com
HAMAMATSU PHOTONICS K.K., Electron Tube Center
314-5, Shimokanzo, Toyooka-village, Iwata-gun, Shizuoka-ken, 438-0193, Japan, Telephone: (81)539/62-5248, Fax: (81)539/62-2205
U.S.A.: Hamamatsu Corporation: 360 Foothill Road, P. O. Box 6910, Bridgewater, N.J. 08807-0910, U.S.A., Telephone: (1)908-231-0960, Fax: (1)908-231-1218
Germany: Hamamatsu Photonics Deutschland GmbH: Arzbergerstr. 10, D-82211 Herrsching am Ammersee, Germany, Telephone: (49)8152-375-0, Fax: (49)8152-2658
France: Hamamatsu Photonics France S.A.R.L.: 8, Rue du Saule Trapu, Parc du Moulin de Massy, 91882 Massy Cedex, France, Telephone: (33)1 69 53 71 00, Fax: (33)1 69 53 71 10
United Kingdom: Hamamatsu Photonics UK Limited: Lough Point, 2 Gladbeck Way, Windmill Hill, Enfield, Middlesex EN2 7JA, United Kingdom, Telephone: 44(20)8-367-3560, Fax: 44(20)8-367-6384
North Europe: Hamamatsu Photonics Norden AB: Smidesvägen 12, SE-171-41 SOLNA, Sweden, Telephone: (46)8-509-031-00, Fax: (46)8-509-031-01
Italy: Hamamatsu Photonics Italia: S.R.L.: Strada della Moia, 1/E, 20020 Arese, (Milano), Italy, Telephone: (39)02-935 81 733, Fax: (39)02-935 81 741

TPMH1117E02
DEC. 1999

Appendix B

Excess Noise Factor

The excess noise factor (ENF) is a useful quantity which allows a quantitative prediction of the performance of a photomultiplier (PMT) to be made. It arises from the statistical nature of the electron multiplication process and provides an estimation of the contribution of the dynodes to the output signal variance. When n_{Phe} photoelectrons emerge from the photocathode they are multiplied in the dynode chain and a signal builds up at the PMT anode. In an hypothetical dynode chain with a constant multiplication factor M the output signal generated by n_{Phe} photoelectrons would be formed by $n_{Phe} \times M$ electrons. However, in a real PMT the number of electrons emitted by each dynode fluctuates, and the resulting output signal is instead distributed around its mean value $\overline{S}_{out} = n_{Phe} \times \overline{M}$, where $\overline{M}$ is the mean value of the distribution that characterizes the multiplication process. The relative variance of the output signal distribution $\left(\sigma_{S_out}/\overline{S}_{out}\right)^2$, characterized by the mean output signal $\overline{S}_{out}$ and variance $\sigma_{S_{out}}$ is given by

$$\left(\frac{\sigma_{S_{out}}}{\overline{S}_{out}}\right)^2 = \left(\frac{\sigma_{n_{Phe}}}{\overline{n}_{Phe}}\right)^2 + \left(\frac{\sigma_M}{\overline{M}}\right)^2 \tag{B.1}$$

where the term $(\sigma_{nPhe}/\overline{n}_{Phe})^2$ is the relative variance of the generated photoelectrons characterized by the mean number of photoelectrons $\overline{n}_{Phe}$ and variance σ_{nPhe}. The term $\left(\frac{\sigma_M}{\overline{M}}\right)^2$ is the relative variance of the multiplication process characterized by the mean multiplication factor $\overline{M}$ and the multiplication process variance σ_M^2. The mean multiplication $\overline{M}$ is assumed to be made up of the contribution of n_{Phe} independent avalanches with gain m_i, each triggered by a single electron and therefore

$$\overline{M} = \frac{1}{n_{Phe}\sum_{i=1}^{n_{Phe}} m_i} = G_{SER} \tag{B.2}$$

where G_{SER} is the photomultiplier single electron response gain. Analogously, the multiplication process variance $\sigma_{\overline{M}}$ can be written as follows

$$\sigma_M^2 = \sum_{i=1}^{n_{Phe}} \left(\frac{\partial \overline{M}}{\partial m_i} \right)^2 \sigma_{m_i}^2 = \frac{1}{n_{Phe}} \sum_{i=1}^{n_{Phe}} \sigma_{m_i}^2 = \frac{1}{n_{Phe} \sigma_{G_{SER}}^2} \tag{B.3}$$

where

$$\sum_{i=1}^{n_{Phe}} \sigma_{mi}^2 = \sigma_{G_{SER}}^2 \tag{B.4}$$

and σ_{GSER}^2 is the single electron response variance. Assuming that the fluctuations in n_{Phe} follow a Poisson distribution, then

$$\sigma_{n_{Phe}}^2 = \overline{n}_{Phe} \tag{B.5}$$

and therefore equation B.1 can be written as follows

$$\left(\frac{\sigma_{S_{out}}}{\overline{S}_{out}} \right)^2 = \frac{1}{\overline{n}_{Phe}} \left(1 + \left(\frac{\sigma_{G_{SER}}}{G_{SER}^2} \right)^2 \right) \tag{B.6}$$

and

$$\left(\frac{\sigma_{S_{out}}}{\overline{S}_{out}} \right)^2 = \frac{ENF}{\overline{n}_{Phe}} \tag{B.7}$$

where the excess noise factor (ENF) was defined as follows

$$ENF = 1 + \left(\frac{\sigma_{G_{SER}}}{G_{SER}} \right)^2 \tag{B.8}$$

The excess noise factor reflects the variability degree in the multiplication processes. If the multiplications occurring at the dynodes were all equal them $\sigma_M = 0$ and $ENF = 1$ and the fluctuation in the output signal of the PMT would just reflect the variation of the generated photoelectrons at the photocathode. The ENF can be estimated from the single photoelectron response spectrum of a PMT by direct calculation of G_{SER} and $\sigma_{G_{SER}}$. If the absolute gain of the PMT is known the ENF can also be experimentally determined by the output signal distribution originated from a known number of photoelectrons n_{Phe} using equation B.7

Appendix C

Equivalent Noise Charge

The relative variance of the output signal distribution of a PMT characterized by the mean μ_{out} and variance σ_{out} can be written as

$$\left(\frac{\sigma_{out}}{\mu_{out}}\right)^2 = \left(\frac{\sigma_s}{\mu_s}\right)^2 + \left(\frac{\sigma_n}{\mu_n}\right)^2 \tag{C.1}$$

where μ_s and σ_s are the mean and the standard deviation of the PMT signal component of the output signal and μ_n and σ_n are the mean and the standard deviation of the readout noise component. Assuming that the noise is distributed around the value $\mu_n = 0$ (this assumption is equivalent to subtracting the mean noise value from the output signal), then we may write

$$\left(\frac{\sigma_{out}}{\mu_{out}}\right)^2 = \left(\frac{\sigma_s}{\mu_{out}}\right)^2 + \left(\frac{\sigma_n}{\mu_{out}}\right)^2 \tag{C.2}$$

As was seen in appendix B, the first term is related with the excess noise factor (ENF) and the photoelectron distribution characterized by the mean number of photoelectrons ejected from the photocathode μ_{Phe} with variance σ^2_{Phe} as follows

$$\left(\frac{\sigma_s}{\mu_{out}}\right)^2 = \left(\frac{\sigma_{Phe}}{\mu_{Phe}}\right)^2 ENF \tag{C.3}$$

The readout noise variance σ_n^2 is typically expressed in terms of the *equivalent noise charge* (ENC), which is defined as the amount of charge that, if applied suddenly to the input terminal of the system, would give rise to an output voltage equal to the RMS level of the output due only to noise [7]. The output signal mean μ_{out} can be written as

$$\mu_{out} = N_{Ph} \cdot QE \cdot CE \cdot G \tag{C.4}$$

where N_{Ph} is the number of photons striking the photocathode with quantum efficiency QE. CE and G are respectively the collection efficiency and

the gain of the PMT. Using equations C.3 and C.4 we may write equation C.1 as follows

$$\left(\frac{\sigma_{out}}{\mu_{out}}\right)^2 = \left(\frac{\sigma_{Phe}}{\mu_{Phe}}\right)^2 ENF + \left(\frac{ENC}{N_{Ph} \cdot QE \cdot CE \cdot G}\right)^2 \tag{C.5}$$

Appendix D

The center of gravity algorithm

An example of a typical hexagonal arrangement of photodetectors in a scintillation camera is schematically depicted in figure D.1 showing the coordinate system commonly used with the center of gravity algorithm. Consider-

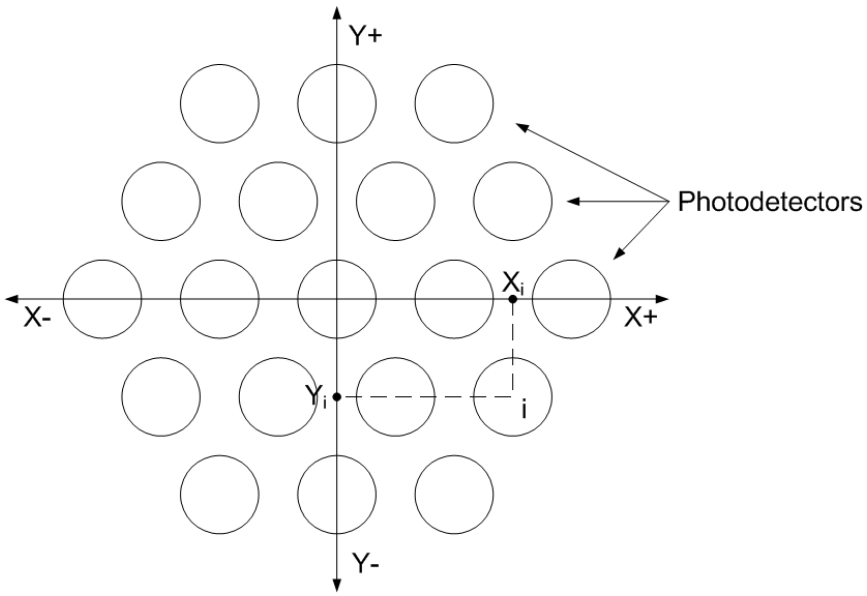

FIGURE D.1: Typical hexagonal arrangement of photodetectors in a scintillation camera.

ing a generic array of n photodetectors, each photodetector i is characterized by its position (X_i, Y_i) and its characteristic weight w_i [1], where $i = 1, ..., n$ is the number of the corresponding photodetector (see figure D.1). A scintillation event will give rise to a set of n output signals s_i, $(i = 1, 2, ..., n)$ characteristic of the location where the scintillation event occurred. In the coordinate system defined in figure D.1, the position estimate of an event $(\hat{x}, \hat{y})$

[1]The weight of each individual PMT is related to the differences in the magnitude of the signal between the photodetectors when measured under the same illumination conditions.

is given by the center of gravity algorithm as follows

$$\hat{x} = \frac{\sum\limits_i w_i s_i X_i}{\sum\limits_i w_i s_i}, \qquad \hat{y} = \frac{\sum\limits_i w_i s_i Y_i}{\sum\limits_i w_i s_i} \tag{D.1}$$

The statistical fluctuations of s_i, imply a corresponding uncertainty in the reconstructed locations $\delta_{\hat{x}}$ and $\delta_{\hat{y}}$. Given that the center of gravity localization algorithm is independent along the X and Y directions, it is suffice to consider the one dimensional case (i.e. the results for $\hat{x}$ are analogous for $\hat{y}$). The uncertainty in $\hat{x}$, $\delta_{\hat{x}}$ can be straightforward calculated using the error propagation as follows

$$\delta_{\hat{x}}^2 = \sum_i (\frac{\partial \hat{x}}{\partial s_i})^2 (\delta s_i)^2 \tag{D.2}$$

Differentiating equation D.1 gives

$$\frac{\partial \hat{x}}{\partial s_i} = w_i (\frac{x_i - \hat{x}}{\sum_i s_i}) \tag{D.3}$$

and therefore

$$\delta_{\hat{x}}^2 = \frac{1}{\sum_i w_i s_i} \frac{\sum_i w_i (x_i - \hat{x})^2 \delta {s_i}^2}{\sum_i w_i s_i}. \tag{D.4}$$

Assuming that the fluctuations of the photodetector signals s_i follows a Poisson distribution i.e $\delta_{s_i} = \sqrt{s_i}$ equation D.4 becomes

$$\delta_{\hat{x}} = \frac{1}{\sqrt{\sum_i w_i s_i}} \sqrt{\frac{\sum_i (x_i - \hat{x})^2 w_i^2 s_i}{\sum_i w_i s_i}} = \frac{\sigma}{\sqrt{S}} \tag{D.5}$$

with σ being the standard deviation of the input distribution i.e. $\hat{x}$ and $S = \sum_i s_i$ the total signal. The quantity σ is a measure of the dispersion of the photodetector signals s_i and therefore $\delta_{\hat{x}}$ decreases as the signals distribution narrows. Additionally, $\delta_{\hat{x}}$ is also proportional to the inverse of the square root of the total signal S (i.e. the total amount of charge produced by the incoming scintillation light photons). Therefore, a better position estimate $\hat{x}$ and $\hat{y}$ is expected from the center of gravity algorithm when the light yield is high and and narrowly distributed.

Appendix E

Photodiode AXUV100G datasheet

ELECTRON DETECTION 100 mm² **AXUV100G**

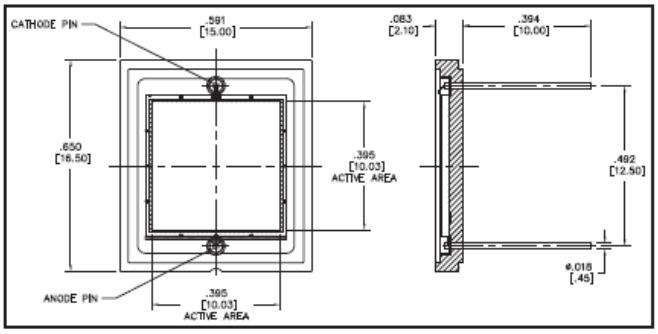

FEATURES

- Ideal for electron detection
- Large detection area
- 100% internal QE

Dimensions are in inch [metric] units.

ELECTRO-OPTICAL CHARACTERISTICS AT 25°C

PARAMETERS	TEST CONDITIONS	MIN	TYP	MAX	UNITS
Active Area	10mm x 10mm		100		mm^2
Responsivity, $\mathcal{R}$	@ 254nm, V_R = 0V	0.07	0.08	0.09	A/W
Shunt Resistance, Rsh	V_B = ±10mV	20			M-ohm
Reverse Breakdown Voltage, V_R	I_R = 1μA		10		Volts
Capacitance, C	V_R = 0V		10	44	nF
Rise Time	V_R = 0V, R_L = 50□			10	usec

THERMAL PARAMETERS

STORAGE AND OPERATING TEMPERATURE RANGE	
Ambient[2]	-10° TO 40°C[2]
Nitrogen or Vacuum	-20°C TO 80°C
Maximum Junction Temperature	70°C
Lead Soldering Temperature[1]	260°C

[1]0.08" from case for 10 seconds.

[2]Temperatures exceeding these parameters may create Oxide growth on the active area.
Over time Responsivity to Low energy radiation and wavelengths below 150nm will Be Compromised.

Shipped with temporary cover to protect photodiode and wire bond. Review Opto Diode "Handling Precautions for IRD Detectors" prior to removing cover.

OPTO DIODE CORP.
750 Mitchell Road, Newbury Park, California 91320
Phone: (805) 499-0335, Fax: (805) 499-8108
Email: sales@optodiode.com, Website: www.optodiode.com

Revision February 26, 2013

ELECTRON DETECTION 100 mm² **AXUV100G**

ELECTRON RESPONSE

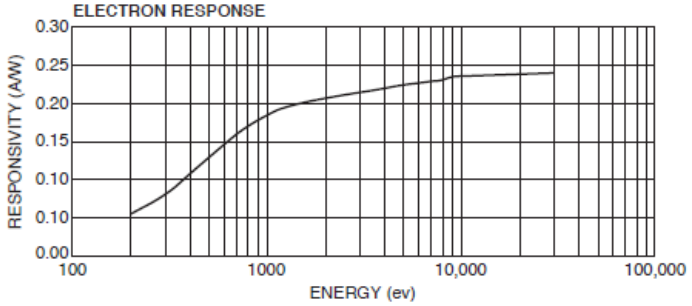

EUV-UV PHOTON RESPONSE

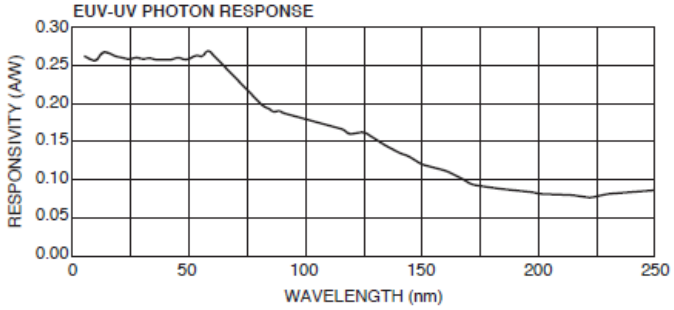

UV-VIS-NIR PHOTON RESPONSIVITY

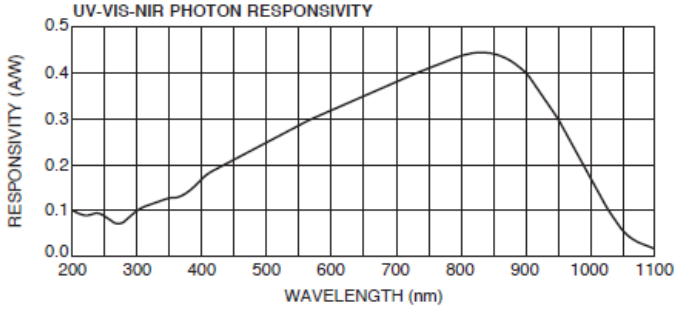

OPTO DIODE CORP.
750 Mitchell Road, Newbury Park, California 91320
Phone: (805) 499-0335, Fax: (805) 499-8108
Email: sales@optodiode.com, Website: www.optodiode.com

Revision February 26, 2013

Appendix F

ANTS2 simulation details

The details of the ANTS2 models used to simulate the camera are described here. The *base configuration* (see figure F.1) is common to all models. The details of other features added according to the simulation requirements, such as scattering surfaces and a glass window, are also given.

F.1 Base configuration

See figure F.1 (a).

- Light-tight box: Dimensions: $500\,\mathrm{mm} \times 500\,\mathrm{mm} \times 500\,\mathrm{mm}$. Material: Cardboard with 100% light absorption coefficient.
- PMTs holder: dimensions: Radius = $80\,\mathrm{mm}$; thickness = $20\,\mathrm{mm}$. Material: Black plastic with 100% light absorption coefficient.
- PMTs mask: dimensions: Radius = $80\,\mathrm{mm}$; thickness = $0.5\,\mathrm{mm}$. PMT window radius = $34\,\mathrm{mm}$. Material: Black plastic with 100% light absorption coefficient.
- PMT geometry: circular, $38\,\mathrm{mm}$ diameter. Glass windows with $2.2\,\mathrm{mm}$ thickness and 1.5 refraction index.
- PMT position: the positions of each PMT was defined accordingly to the experimentally measured positions.
- PMT electronics: the signal of each PMT is generated according to the experimentally measured SER.
- PMT detection probability: the corresponding experimentally measured detection probability is assign to each PMT.
- PMT relative gain: the relative gain of each PMT was assigned according to the experimentally measured values.

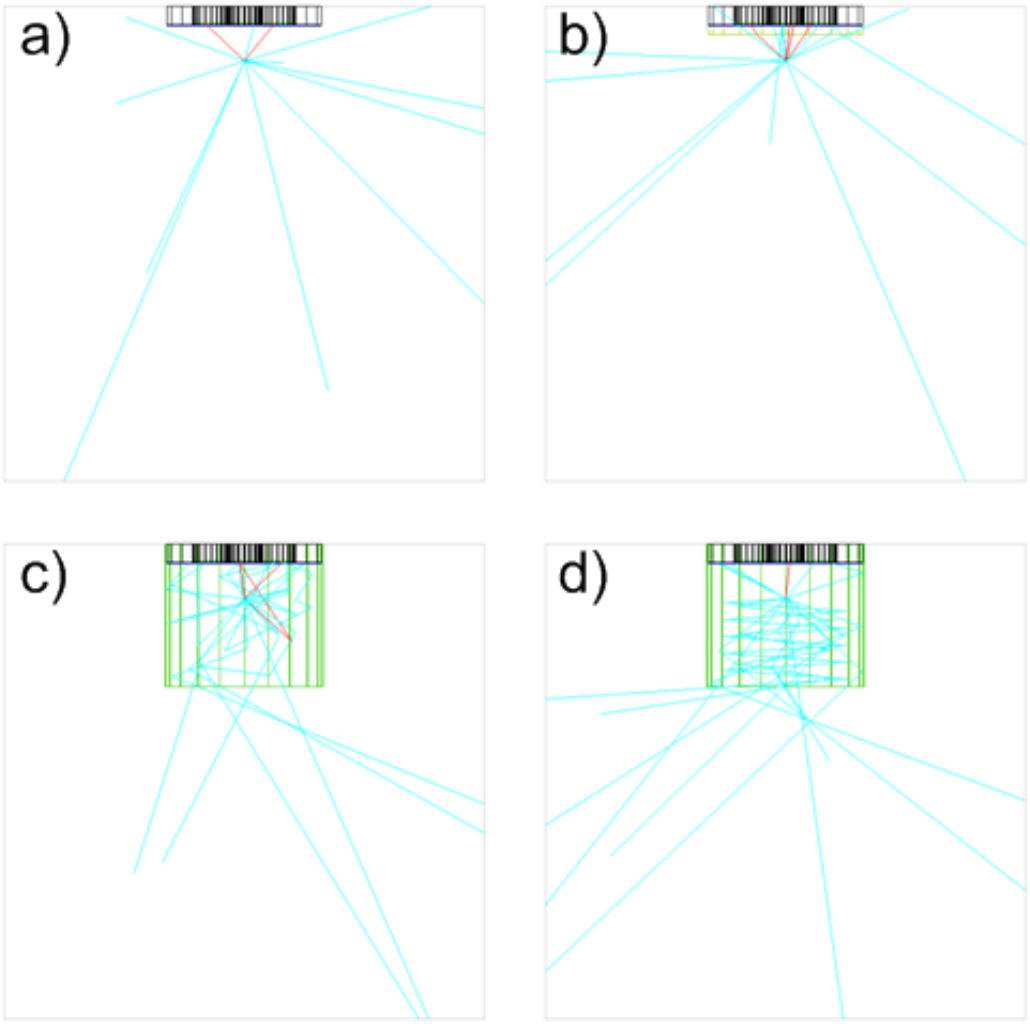

FIGURE F.1: Detector models simulated in ANTS2: a) base configuration; b) with a glass window added; c) with a PTFE wall; d) with an aluminized mylar wall.

- General reflection model: accordingly to the Snell and Fresnel laws.
- Light source: Punctual and isotropic.

F.2 Base configuration + Glass window

See figure F.1 (b).

- Material: common glass.
- Dimensions: internal radius = $81\,\mathrm{mm}$; thickness = $2\,\mathrm{mm}$.

F.3 Base configuration + Scattering surface

See figure F.1 (c) and (d).

- Material: PTFE or aluminized.
- Dimensions: radius = $80\,\mathrm{mm}$; thickness = $10\,\mathrm{mm}$.
- Scattering model: F. Neves (material albedo and refractive index).

Bibliography

[1] A. Morozov, I. Defendi, R. Engels, F.A.F. Fraga, B. Guerard, M. Jurkovic, G. Kemmerling, G. Manzin, L.M.S. Margato, H. Niko, L. Pereira, D. Raspino, N.J. Rhodes, F. Sacchetti, E.M. Schooneveld, P. Van Esch and K. Zeitelhack. "A 2D position sensitive gas scintillation detector for thermal neutrons". In: *Symposium and Medical Imaging Conference (NSS/MIC), IEEE* (2012).

[2] D.N. McKinsey. "The LZ dark matter experiment". In: *Journal of Physics: Conference Series* 718.042039 (2016).

[3] N. Lopez-March. "Sensitivity of the NEXT-100 detector to neutrinoless double beta decay". In: *arXiv:1701.02697v1 [physics.ins-det]* (2017).

[4] A. Morozov, F. Alves, J. Marcos, R. Martins, L. Pereira, V. Solovov, V. Chepel. "Iterative reconstruction of SiPM light response functions in a square-shaped compact gamma camera". In: *Physics in Medicine and Biology* 62.9 (2012), p. 3619.

[5] F.A.F. Fraga, L.M.S.Margato, S.T.G. Fetal, I. Ivaniouchenkov, R. Ferreira Marques and A.J.P.L. Policarpo. "Luminescence and imaging with gas electron multipliers". In: *Nuclear Instruments and Methods in Physics Research A* 513 (2003), pp. 379–387.

[6] A. Morozov et al. "ANTS2 package: simulation and experimental data processing for Anger camera type detectors". In: *JINST* 11.P04022 (2012).

[7] Glenn F. Knoll. "Radiation detection and measurements, 4th. edition". In: (2010).

[8] William R. Leo. "Techniques for Nuclear and Particle Physics Experiments: A How-to Approach, 1st. edition". In: *Springer-Verlag* (1987).

[9] R.D. Evans. *The Atomic Nucleus*. McGraw-Hill Book Company, 1955. Chap. 23, p. 672.

[10] F. N. Flakus. "Detecting and measuring ionizing radiation - a short history". In: *IAEA bulletin* 23.4 (1981).

[11] J. B. Birks et al. "The Theory and Practice of Scintillation Counting". In: *Pergamon Press, Oxford* (1964).

[12] Otto Glasser. "Wilhelm Conrad Roentgen and the Early History of the Roentgen Rays". In: *Norman publishing, San Francisco* (1993).

[13] G. E. Chikovani, V. A. Mikhailov, and V. N. Roinishvili. In: *Phys. Lett.* 6 (1963), p. 254.

[14] B. A. Dolgoshein, B. U. Rodionox and B. I. Luchkov. "Streamer chamber". In: *Nucl. Instrum. Meth.* 29 (1964), p. 270.

[15] J. Curran S. C., Angus and Cockcroft. "Beta Spectrum of Tritium". In: *Nature* 162 (1948), p. 302.

[16] C. A. N. Conde and A. J. P. L. Policarpo. "A gas proportional scintillation counter". In: *Nucl. Instrum. Meth.* 53 (1967), p. 7.

[17] G. Charpak, S. Majewski and F. Sauli. "The scintillating drift chamber: A new tool for high-accuracy, very-high-rate particle localization". In: *Nucl. Instrum. Meth.* 126 (Mar. 1975), pp. 381–389.

[18] A.J.P.L. Policarpo, M.A.F. Alves, M.C.M. Dos Santos and M.J.T. Carvalho. "Improved resolution for low energies with gas proportional scintillation counters". In: *Nucl. Instrum. Meth.* 102 (Feb. 1972), pp. 337–348.

[19] H. N. Ngoc G. Charpak and A. Policarpo. "Neutral radiation detection and localization". In: *United States Patent 4,286,158* (1981).

[20] C. A. N. Conde, M. C. M.Santos, M. Fatima A. Ferreira and Celia A. Sousa. "An argon scintillation counter with uniform electric field". In: *IEEE Transactions on Nuclear Science* 22 (1975).

[21] H.O. Anger. "Scintillation Camera". In: *Rev. Sci. Instrum.* 29 (1958), pp. 27–33.

[22] F. Sauli. "GEM: A new concept for electron amplification in gas detectors". In: *Nuclear Instruments and Methods in Physics Research Section A: Accelerators, Spectrometers, Detectors and Associated Equipment* 386, Issue 2-3 (1997), pp. 531–534.

[23] A. Oed. "Properties of micro-strip gas chambers (MSGC) and recent developments". In: *Nuclear Instruments and Methods in Physics Research Section A: Accelerators, Spectrometers, Detectors and Associated Equipment* 367 (1995), pp. 34–40.

[24] F.A.F. Fraga, L.M.S. Margato, S.T.G. Fetal, I. Ivaniouchenkov, R. Ferreira Marques and A.J.P.L. Policarpo. "Imaging detectors based on the gas electron scintillation light". In: *Nuclear Science Symposium Conference Record 2000 IEEE* (2000).

[25] F.A.F. Fraga, L.M.S. Margato, S.T.G. Fetal, M.M.F.R. Fraga, R. Ferreira Marques, A.J.P.L. Policarpo, B. Guerard, A. Oed, G. Manzini and T. van Vuure. "CCD readout of GEM-based neutron detectors". In: *Nuclear Instruments and Methods in Physics Research A* 478 (2002), pp. 357–361.

[26] G. Manzini, B. Guerard, F.A.F. Fraga and L.M.S. Margato. "A gas proportional scintillaton counter for thermal neutrons instrumentation". In: *Nuclear Instruments and Methods in Physics Research A* 535 (2004), pp. 102–107.

[27] A. E. Grün and E. Schopper. "Über die Fluoreszenz von Gasen beim Anregung durch α Teichen". In: *Z. Naturfoschg.* 6a (1951), pp. 698–700.

[28] S. R. Hunter, J. G. Carter and L. G. Christophorou. "Electron motion in the gases CF4, C2F6, C3F8 and n-C4F10". In: *PHYSICAL REVIEW A* 38 (1988).

[29] L.M.S. Margato, A. Morozov, M.M.F.R. Fraga, L. Pereira and F.A.F. Fraga. "Effective decay time of CF4 secondary scintillation". In: *JINST 8 P07008* (2013).

[30] F. Sauli. "The gas electron multiplier (GEM): Operating principles and applications". In: *Nuclear Instruments and Methods A* 805 (2016), pp. 2–24.

[31] P. Geltenbort and A. Oed. "Proceedings of the Workshop on Progress in Gaseous Microstrip Proportional Chambers 21–23 June 1993". In: (1993).

[32] A. Morozov, M.M.F.R. Fraga, L. Pereira, L.M.S. Margato, S.T.G. Fetal, B. Guerard, G. Manzin and F.A.F. Fraga. "Photon yield for ultraviolet and visible emission from CF4 excited with alpha-particles". In: *Nuclear Instruments and Methods in Physics Research Section B* 268.9 (2010), pp. 1456–1459.

[33] Claus Grupen and Irène Buvat. Springer-Verlag, Berlin, Heidelberg, 2012.

[34] Y. Kawai, H. Nakayama, A. Kusaka, H. Kakuno, T. Abe, M. Iwasaki, H. Aihara, M. Tanaka, M. Shiozawa, H. Kyushima and M. Suyama. "Large aperture hybrid photodetector". In: *Nuclear Instruments and Methods in Physics Research Section A: Accelerators, Spectrometers, Detectors and Associated Equipment* 579 (2007), pp. 42–45.

[35] Z. Sadygov. In: *Russian Patent 2102820* (1996).

[36] J. Abraham. "The Fluorescence Detector of the Pierre Auger Observatory". In: *Nucl.Instrum.Meth. A* 620 (2010).

[37] Glenn Roberts Jr. "Construction of World's Most Sensitive Dark Matter Detector Moves Forward". In: (2016). URL: http://newscenter.lbl.gov/2016/09/26/lz-dark-matter-detector-moves-forward/.

[38] Reyco Henning. "Current status of neutrinoless double-beta decay searches". In: *Reviews in Physics* 1 (2016), pp. 29–35.

[39] S. Andringa. "Current Status and Future Prospects of the SNO+ Experiment". In: *arXiv:1508.05759v3 [physics.ins-det]* (2016).

[40] S. Fukuda et al. "The Super-Kamiokande detector". In: *Nuclear Instruments and Methods in Physics Research A* 501.042039 (2003), 418–462.

[41] "Hubble Space Telescope Servicing Mission 3A. Fine guidance sensor." In: (2017). URL: https://www.spacetelescope.org/about/general/instruments/fgs/.

[42] A.G. Wright. "Metal ceramic photomultipliers for oil well logging". In: *Technical reprint RP/079 from E.T. Enterprises* (2016). URL: http://www.et-enterprises.com/files/file/technical-information/rp079_Metal%20Ceramic%20Pmt.pdf.

[43] *Photomultiplier Tubes: Basics and Applications*. 3rd ed. 2007.

[44] K. K. Hamamatsu-Photonics. "Hamamatsu Super Bialkali Photocathodes". In: (2006). URL: http://www.hamamatsu.com/jp/en/technology/innovation/photocathode/index.html.

[45] ET Enterprises. "Photomultiplier brochure from ET-Enterprises". In: (), p. 6. URL: http://www.et-enterprises.com/photomultipliers.

[46] J. R. Prescott. "A Statistical Model for Photomultiplier Single-Electron Statistics". In: *Nucl. Instr. Methods* 39 (1966), pp. 173–179.

[47] F. Neves. "Aplicação de xénon líquido na detecção de matéria escura". PhD thesis. Universidade de Coimbra, Portugal, 2006.

[48] Janardan Misra and Indranil Saha. "Artificial neural networks in hardware: A survey of two decades of progress". In: *Neurocomputing* 74 (2010), 239–255.

[49] Wasserman. *Neural Networks Fundamentals for Scientists and Engineers*. 1989.

[50] Kyoung-Su Oh and Keechul Jung. "GPU implementation of neural networks". In: *Pattern Recognition* 37.6 (2004), pp. 1311–1314.

[51] Amos R. Omondi and Jagath C. Rajapakse, eds. *FPGA Implementations of Neural Networks*. Springer-Verlag New York, Inc. Secaucus, NJ, USA, 2006.

[52] Alex Ryer. *Light Measurement Handbook*. 2000. URL: `www.intl-light.com/customer/handbook/handbook`.

[53] Eugene Hecht. *Optics*. Addison-Wesley, 2012.

[54] H.J. Van Stavaren et al. "Construction, quality assurance and calibration of spherical isotropic fibre optic light diffusers". In: *Laser Med. Sci.* 10 (1995), pp. 137–147.

[55] Flyckt S.O. and C. Marmonier. *Photomultiplier Tubes: Principles and Applications*. Ed. by France Philips Photonics Brive. 2002.

[56] Wright A. G. "Determination of the multiplier gain of a photomultiplier". In: *J. Phys. E: Sci. Instrum.* 14 (1981), pp. 851–5.

[57] E.H. Bellamy et al. "Absolute calibration and monitoring of a spectrometric channel using a photomultiplier". In: *Nucl. Instr. and Meth. A* 339 (1994), pp. 468–476.

[58] A. Morozov, I. Defendi, R. Engels, F.A.F. Fraga, M.M.F.R. Fraga, B. Guerard, M. Jurkovic, G. Kemmerlingv, G. Manzin, L.M.S. Margato, H. Niko, L. Pereira, C. Petrillo, A. Peyaud, F. Piscitelli, D. Raspino, N.J. Rhodesv F. Sacchetti, E.M. Schooneveld, P. Van Eschd and K. Zeitelhack. "ANTS — a simulation package for secondary scintillation Anger-camera type detector in thermal neutron imaging". In: *JINST* 7.P08010 (2012).

[59] V. Solovov et al. "B-spline parameterization of spatial response in a monolithic scintillation camera". In: *JINST* 11.P09014 (2016).

[60] D.S. Akerib et al. "The Large Underground Xenon (LUX) experiment". In: *Nucl. Instrum. Meth. A* 704 (2013), p. 111.

[61] Peter Seitz. "Single-Photon Imaging". In: *Springer Series in Optical Sciences* 160 (2011).

[62] F. Neves et al. “Measurement of the absolute reflectance of polytetrafluoroethylene (PTFE) immersed in liquid xenon”. In: *JINST* 12.P01017 (2017).

[63] Martin Janecek. “Optical Reflectance Measurements for Commonly Used Reflectors”. In: *IEEE TRANSACTIONS ON NUCLEAR SCIENCE* 55.4 (2008).

[64] Min K. Yang and Roger H. French. “Optical properties of Teflon AF amorphous fluoropolymers”. In: *J. Micro/Nanolith. MEMS MOEMS* 7.033010 (2008).

[65] Victor R. Weidner and Jack J. Hsia. “Reflection properties of pressed polytetrafluoroethylene powder”. In: *J. Opt. Soc. Am.* 71.7 (1981), pp. 275–288.

[66] Morozov et al. “Iterative reconstruction of SiPM light response functions in a square-shaped compact gamma camera”. In: *Phys Med Biol.* 62.9 (2017).